



**HAL**  
open science

## RF switches based on 2D materials

Simon Skrzypczak

► **To cite this version:**

Simon Skrzypczak. RF switches based on 2D materials. Micro and nanotechnologies/Microelectronics. Université de Lille, 2023. English. NNT : 2023ULILN006 . tel-04320864

**HAL Id: tel-04320864**

**<https://theses.hal.science/tel-04320864v1>**

Submitted on 4 Dec 2023

**HAL** is a multi-disciplinary open access archive for the deposit and dissemination of scientific research documents, whether they are published or not. The documents may come from teaching and research institutions in France or abroad, or from public or private research centers.

L'archive ouverte pluridisciplinaire **HAL**, est destinée au dépôt et à la diffusion de documents scientifiques de niveau recherche, publiés ou non, émanant des établissements d'enseignement et de recherche français ou étrangers, des laboratoires publics ou privés.



## THESE

Présentée à l'Université de Lille

Ecole Doctorale Sciences de l'Ingénierie et des Systèmes

Pour obtenir le grade de :

Docteur de l'Université

**Spécialité : Micro et Nano Technologies, Acoustique et Télécommunications**

Par

SKRZYPCZAK Simon

Unité de recherche: IEMN

RF switches based on 2D materials

Commutateurs RF fabriqués à partir de matériaux 2D

Soutenue le 29 Mars 2023 devant la Commission d'examen

Membres du jury :

Mr. Henri HAPPY (Professeur)

Mme. Christelle AUPETIT-BERTHELEMOT (Professeur)  
Limoges – Limoges)

Mme. Florence PODEVIN (Professeur)

Mr. Renato NEGRA (Professeur)

Mr. Emiliano PALLECCHI (Maître de conférences)

Mr. Deji AKINWANDE (Professeur)  
– Austin)

Mr. Mario LANZA (Professeur associé)

Mr. Guillaume DUCOURNAU (Professeur)

Directeur de thèse (IEMN – Lille)

Présidente du Jury (Université de

Rapporteur (INP – Grenoble)

Rapporteur (RWTH – Aachen)

Examineur (IEMN – Lille)

Examineur (University of Texas

Examineur (KAUST – Thuwal)

Invité (IEMN – Lille)

# Table of Content

General Introduction:.....	5
CHAPTER I State of the art of RF Switches .....	10
1. Introduction.....	12
2. RF switch characteristics .....	12
2.1. Main topology of RF switch .....	16
3. Technologies used nowadays.....	16
3.1. PIN diode - short description .....	16
3.2. <i>FET - Short description</i> .....	18
3.3. MEMS switching devices.....	21
4. Emerging switching technologies.....	24
4.1. Description of metal insulator transition (MIT) switch.....	25
4.2. Phase change material (PCM) switches .....	26
4.3. Conductive bridge switches .....	27
4.4. Resistive switching observed with 2D material .....	28
4.5. Application for emerging technology RF switches .....	30
5. Comparison between different RF switches .....	30
6. Conclusion .....	32
7. References.....	33
CHAPTER II Optimization of the 2D RF switch layout and RF measurement setup .....	37
1. Introduction.....	39
2. RF study.....	39
2.1 Coplanar waveguide (CPW) .....	39
2.2 CPW study.....	40

2.3	Structure of 2D switch .....	42
3.	Description of DC and RF measurement procedure .....	48
3.1	RF measurement procedure .....	48
3.2	De-embedding procedure.....	49
4.	Conclusion .....	52
5.	References.....	53
CHAPTER III Fabrication and RF characterization of 2D based switches .....		55
1.	Introduction.....	58
2.	Fabrication process .....	59
2.1	Overview of microfabrication .....	59
2.2	Description of the layout .....	60
2.3	Fabrication of alignment marks .....	62
2.4	Fabrication of the bottom electrode (BE).....	63
2.5	2D material transfer and patterning.....	65
2.6	Fabrication of the top electrode (TE).....	68
2.7	CPW pads deposition .....	70
3.	I-V characterization and S-parameters study.....	71
3.1	Switching phenomenon description .....	71
3.2	Measurement protocol.....	73
3.3	I-V characteristics measurement and S-parameters of switches with 6 monolayers of MoS <sub>2</sub> (SS03).....	76
3.4	I-V characteristics and S-parameters measurement of Ni/MoS <sub>2</sub> /Pt interface .....	80
3.5	SS07 I-V characteristic and S-parameters measurement .....	84
4	De embedding of devices and FOM parameters extraction of 3MLs and 6 MLs of MoS <sub>2</sub>	88
5.	Conclusion .....	91

6. References.....	92
CHAPTER IV Linearity and data communication .....	94
1. Introduction.....	96
2. Linearity.....	97
2.1. IP3 measurement principle .....	98
2.2. Polynomial fit and extraction for ADS simulation.....	100
2.3. Result of the IP3 measurement .....	102
2.4. IP3 conclusion .....	104
3. Real life scenario: data communication .....	104
3.1. Structures of switches used for data communications .....	104
3.2. RF characteristics of switches used for data communications.....	105
3.3. Setup for data communication at 100 GHz .....	107
3.4. RF result on data communication at 100 GHz .....	109
3.5. Data communication at 320 GHz .....	111
3.6. Setup for data communication at 320GHz and advanced vectorial modulation	112
3.7. RF result on data communication at 320 GHz .....	113
4. Conclusion .....	116
5. References.....	117
Conclusion and perspectives.....	119
Perspectives:.....	122
ANNEX .....	123
Annex of chapter 2 .....	123
Annex of chapter 3 .....	125
Annex of chapter 4 .....	142
Summary .....	145

# Acknowledgement

First, I would like to express my appreciation to my supervisor Dr E. Pallecchi and my director Professor Henri Happy for their patience, their expertise and their continuous support during my thesis. Their kindness and guidance were what make me able to finish this doctoral study. Without their help, this work would not have been possible.

I would like to thank the reviewers of this work: Professor F. Podevin and Professor R. Negra for their comments on this dissertation and Professor C. Aupetit-berthelemot; Professor D Akinwande and Associated Professor M. Lanza for participating in the defense committee.

I give my appreciation to Dr D. Vignaud, thanks to him I learned a lot on 2D materials this last three years. I also thank Professor G. Ducournau for its precious help for the RF part of this work and its precious advices.

I thank our partner from CEA Leti and IMEP that work with me in this project. They are Dr R. Gassilloud, Dr A. Cresti and Dr J. David-Vifflantzeff. I also thank the partner from University of Texas in Austin for their exchange who are Professor D. Akinwande, Dr K. Myungsoo and S. Jin Yang.

I would like to express my gratitude to all the cleanroom engineers who helped me in many ways for the fabrication, the optical characterization. They are Dr F. Vaurette; Mr Y. Deblock; Mr P. Tilmant; Mr M. Dewitte; Dr I. Roch-jeune; Mr C. Boyaval; Mrs S. Ouendi Dr D. Yarekha and Mr T. Bertrand. I would like to express my gratitude to the engineers of the characterization center who are Ms V. Avramovic; Mr E. Okada; Dr S. Eliet and Ms S. Lepilliet. I also thank Dr D. Guerin for its help.

I also thank all my friends from IEMN that support me during this thesis. They are Thomas, Yevheniia, Houda, Nemanja, Louis, Quentin, Jeyan, Martin, Yasmine, Fawzi, Rupali and Leslie. Thanks for all the memories of these 3 years. I thank aswell all the people which I work to this past 3 year that I did not named before.

Finally, I would like to thank my family: my parents and sister, and finally Lucile my fiancee. I also thank my cat Yuumi which help me relieve some stress. Thank for giving me your support and love which give me courage to move forward.

# General Introduction:

With the growth of the market of telecommunication with 4G and 5G and the place that the internet of things is taking in our everyday life, more and more wireless telecommunication systems are needed and have to work at very high frequency. The future 6G is currently a discussion topic and its working frequency band will be above 100GHz.

Radio frequency (RF) switches play an important role in these wireless systems, where they are used for multiple applications such as: routing high frequency signals through systems, routing the signal in the front-end module of telecommunication systems for transceivers, ...

The main technologies used for RF switches nowadays are complementary metal oxide semiconductor (CMOS) technology, field effect transistors (FET), positive intrinsic negative (PIN) diodes and micromechanical system (MEMS). However, the first and the second show their limits in terms of frequency range, and the latter one has constraint in terms of switching time. De facto, a novel approach is necessary to reach the requirement of the future systems.

With the highlight of 2D material thanks to various funding programs such as the GRAPHENE flagship, and the scientific breakthroughs in the fabrication and characterization of these materials, various applications start to emerge. In 2018, one application using transition metal dichalcogenides (TMD) 2D material shows promising results for high performance RF switches.

It is in this context that my thesis on “RF switches based on 2D materials” takes place. The objectives of my thesis are the development, the fabrication and the characterization of 2D RF switches. This thesis was made in the framework of ANR project SWIT n° ANR-19-CE24-0004-01 under the coordination of Dr. Emiliano PALLECCHI, with the following partners: CEA LETI, IMEP-LaHC.

Given the large scope of the 2D material existing, this thesis will focus on the development of MoS<sub>2</sub> based switches, which have a great interest for the consortium of SWIT project. The first chapter focuses on providing the state of the art about the existing technology for RF switches. After a description of the characteristics of an RF switch, a brief presentation of switches based on semiconductor materials as well as MEMS-based structures are presented. We then discuss emerging technologies based on switches made of transition or phase change

materials, as well as resistive switches. These technologies are derived from memory technologies and have undeniable advantages in terms of system integration. Our attention is then focused on RF switches based on 2D materials, which have the advantage of combining an easy integration in RF systems (no complex switch activation circuit), and of allowing an operation at frequencies close to THz. The active part of the switch is directly inserted in the structure of the transmission line (coplanar transmission lines are used) and the switch is controlled by a DC voltage applied to the transmission line. These devices will be the main work of this thesis.

One of the major objectives of this thesis is to demonstrate that switches based on 2D materials can achieve very high performance in terms of working frequency. Chapter 2 presents the work done to analyze and optimize the proposed structures. This is done through: (i) the optimization of the propagation structures (coplanar waveguide transmission lines) to reach frequencies of the order of 500 GHz, (ii) the calibration and de-embedding techniques to extract the characteristics of the passive switch, (iii) as well as the characterization methodology implemented. The characterization set-ups of the Lab allow to make measurement with RF probes up to the THz regime.

The third chapter focuses on the fabrication and characterization of resistive switches based on molybdenum disulfide ( $\text{MoS}_2$ ). This subject being new in the laboratory, all the steps of the manufacturing process were designed and optimized in the framework of the thesis. Moreover, it was necessary to ensure the compatibility of the manufacturing processes with the 2D material transfer technique, a technological step carried out by the LETI in Grenoble.

The first part of the chapter describes the technological steps used to manufacture the switches. To improve the understanding of the switching mechanisms, several combinations of metals are used as contacts (Bottom and top electrodes) for the 2D material. The size of the active part of the switch is also explored. Three manufacturing batches are fabricated with success: 2 substrates with six monolayers of  $\text{MoS}_2$  named SS03 and SS04 and one substrate with three monolayers of  $\text{MoS}_2$  named SS07.

In the second part dc and RF analysis of switches from the 3 substrates were explored. For this analysis, it is necessary to switch the device ON (SET) and OFF (RESET) according to the



measurement made. For the ON state (positive bias), a current limitation is necessary to avoid device destruction. This is not necessary when the switch is turned to the OFF state (negative bias). The DC analysis shows the reliability of the fabrication process. The impact of ON state current on the resistance of the switch is also pointed out. The highest ON state current is correlated with lower insertion loss. Another important result is the impact of the size of the switch: The best reproducibility is achieved with the  $0,5 \times 0,5 \mu\text{m}^2$  switches. Considering RF performances, measurement on these fabricated multilayer MoS<sub>2</sub> devices were limited to 67 GHz in this chapter. The measurements made show that the initial objective of 15 dB difference between ON state and OFF state is achieved both on transmission without any optimization (substrate 1) and with optimization (substrate 2 and 3). Considering the variation of the devices after already a few switching cycles it was not obvious to extract and to compare efficiently the figure of merit of different batches. But the results are good enough to explore the properties of these devices in a real system. This exploration is made in the next chapter.

Chapter 4 focuses on the practical application of these switches in a real data communication system. This part was developed in collaboration with the university of Texas Austin (research group of Deji Akinwande) and the Photonic-THz group (G. Ducournau) at IEMN. The university of Texas provided us a first batch of device with a monolayer of hexagonal boron nitride (hBN) material as 2D material in a coplanar waveguide (CPW) without any optimization, and a second batch with a monolayer of MoS<sub>2</sub> embedded in optimized CPW design in chapter 2. These devices are fabricated on diamond substrate, and could be considered as the thinnest switches that exist. The electrodes (Top and Bottom electrodes) are made of gold.

In the first part of this chapter, an analysis of the nonlinear behaviour of the 2D multilayer resistive switches is carried out. The main reason is that in the ON state, RF input power can cause self-heating of the device and cause the characteristics of the switch to vary due to thermal effects. The measurements made on switches with multiple layers of MoS<sub>2</sub> show good stability (IP<sub>3</sub> above 26 dBm) and are compatible with the polynomial model extracted from simulation in the ADS software.

The first batch of device received from the University of Austin was characterized at IEMN up to 220 GHz, and an on off keying (OOK) modulation was applied with a carrier signal at 100 GHz. The measurement system composed of terahertz photonic devices is described and

permits to investigate the viability of hBN switches for high-speed data communication. This study concludes by showing the quality of the devices using eye diagramme and bit error rate measurements for an  $8.5 \text{ Gbit.s}^{-1}$  data stream.

Finally, the second batch with a monolayer of MoS<sub>2</sub> was measured up to 480 GHz. The insertion loss was around 0.8 dB in the ON state and the isolation was around -20 dB at 480 GHz. The objectives of these device were to match the new IEEE standard for future 6G which involves advanced modulation uses for spectral efficiency, high data rates of at least  $100 \text{ Gbit.s}^{-1}$  to support the future application modulation at high carrier frequencies (around 300 GHz). Those requirements were achieved with success using a carrier frequency at 320 GHz. Optimized devices could attain a  $100 \text{ Gbit.s}^{-1}$  data rate using 16 quadrature amplitude modulation. This result represents the state-of-the-art, and shows that these devices are suited for 6G communication systems.

A final conclusion on this work will then be given, and the perspective will be described.

# CHAPTER I State of the art of RF Switches

# Table of Contents

CHAPTER I State of the art of RF Switches .....	10
1. Introduction.....	12
2. RF switch characteristics .....	12
2.1. Main topology of RF switch .....	16
3. Technologies used nowadays.....	16
3.1. PIN diode - short description .....	16
3.2. <i>FET - Short description</i> .....	18
3.3. MEMS switching devices.....	21
4. Emerging switching technologies.....	24
4.1. Description of metal insulator transition (MIT) switch.....	25
4.2. Phase change material (PCM) switches .....	26
4.3. Conductive bridge switches .....	27
4.4. Resistive switching observed with 2D material .....	28
4.5. Application for emerging technology RF switches .....	30
5. Comparison between different RF switches .....	30
6. Conclusion .....	32
7. References.....	33

## 1. Introduction

Radio Frequency (RF) switches are critical components used in telecommunication systems. They are used to route high frequency signals through systems. They can be found in the front-end module just before the antenna to switch the system from transmitting to receiving data, in cellular phones or in systems where redundancy and reconfigurability are needed. One of the most widely used technologies for RF switch is complementary metal oxide semiconductor (CMOS) technology. Infineon report sales of over 1 billion unit for 2018 and over 5 billion units over the next 5 years. RF switches are therefore a key part of wireless technology.

In this chapter, I will introduce RF switches and describe successively:

- The characteristics of RF switches. Based on a simplified small-signal equivalent circuit of an RF switch, I will present the main figure-of-merits (FOMs). I will discuss some examples of RF applications with their specific requirements.
- Some technological families of RF switches based on active components (diodes and transistors) or passive components (Micro Electro Mechanical Systems - MEMS) are described with illustrative examples from the literature. The main characteristics of each family of components are given.
- The emerging field of switches based on materials whose properties change according to stimuli such as temperature, electric field, etc. This field is very active and many materials are investigated nowadays. I will describe here some of these components based on metal insulator transition (MIT), phase change material (PCM), and conductive bridge (CB). I will then discuss RF switches based on 2D materials, which will be the subject of our study. The potential of these devices up to the THz regime will be explained.

Finally, a synthesis table of the state of the art of this field is displayed.

## 2. RF switch characteristics

An RF switch is a device that possesses two distinct states, as shown in Fig. 1a. When the switch is in its low resistance state (LRS) – also called the ON state – a high-frequency signal

can be transmitted through the device. A simple electrical equivalent circuit model of an RF switch in the ON state consists of a low resistance,  $R_{ON}$ , in parallel to a capacitance,  $C_{ON}$ , as shown in the red square of Fig. 1b. When the switch is in its high resistance state (HRS) – also called the OFF state – an RF signal is blocked by the device. Its equivalent circuit is then a small capacitance,  $C_{OFF}$ , in parallel to a large resistance,  $R_{OFF}$ , (green square Fig. 1.b). An ideal switch in the ON state can be viewed as a short circuit and an OFF switch as an open circuit. The value of  $R_{ON}$  has an impact on the losses of the system whereas  $C_{OFF}$  affects its operation at high frequencies.

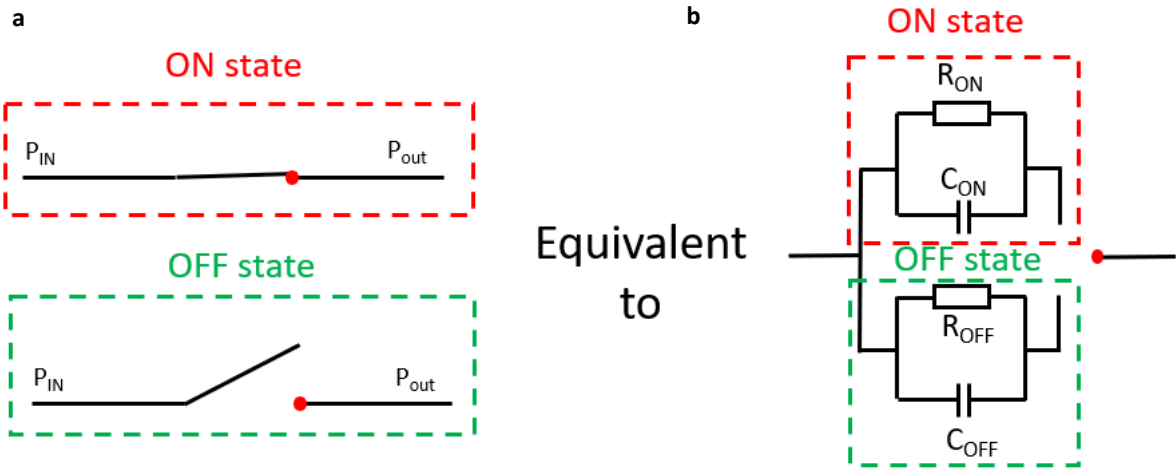


Figure 1: (a) Classical representation of an RF switch. In the ON state (red rectangle) a signal can flow through the device while in the OFF state (green rectangle) the signal is blocked by the device. (b) Equivalent electrical diagram of an RF switch in the ON state (red square) composed of a resistance,  $R_{ON}$ , in parallel with a capacitance,  $C_{ON}$ , and in the OFF state (green square) with a resistance,  $R_{OFF}$ , in parallel with a capacitance  $C_{OFF}$

We now discuss the figure-of-merits (FOMs) for RF switches, starting with one of the most important for telecommunications applications, the so-called  $R_{ON} * C_{OFF}$  product. The  $R_{ON} * C_{OFF}$  product is used to evaluate the high-frequency performances of the device and to calculate the **cut-off frequency,  $f_c$** , which is defined in the literature [1] as:

$$f_c = \frac{1}{2\pi * R_{ON} * C_{OFF}}$$

RF switches have several other figure-of-merits:

- **Insertion loss** represents the attenuation of the signal that flow through the switch in the ON state. The lower the insertion loss the better is the performance of the RF switch in the ON state.
- **Isolation** represents the attenuation of the signal in the OFF state of the device. The higher the isolation the better the RF switch block the RF signal in its OFF state.
- **Power handling** represents the maximal power capability measured in dBm [1] that the switch can handle without permanent electrical performance deterioration or self-switching.
- **Endurance** is the durability of a RF switch represented by the number of switching cycles before failure.
- **Non-volatility** is the capacity for a device to keep its state without external stimuli.
- **Linearity** is the capacity of the device to exhibit a linear I-V characteristics. It is evaluated by the Third order intercept point (IP3)

The above figure-of-merits describe the basic electrical properties of an RF switch and are essential means of comparison of different switch technologies.

RF switches have various applications depending of their performances and are used either as fundamental element or as a Front-end subsystem. In table 1 in the next page, we list some of the main applications and their requirements.

Table 1 Some applications of RF switches from [2]

Fundamental elements	
Elements	Requirement
Tunable inductor	<ul style="list-style-type: none"> <li>• Low <math>R_{ON}</math>, low <math>C_{OFF}</math></li> <li>• Endurance <math>&gt;10^6</math></li> </ul>
Tunable capacitor	
Multiplexers	
Tunable antenna	
RF Front-End Subsystems	
Subsystem	Requirement
Switching networks	<ul style="list-style-type: none"> <li>• Low <math>R_{ON}</math>, low <math>C_{OFF}</math></li> <li>• Small footprint</li> <li>• Endurance <math>10^6 - 10^9</math></li> <li>• Low biasing circuit overhead</li> </ul>
Tunable attenuators	
Tunable filters	
Switched antenna	
Phase shifters	
Switched matching networks	
Switched oscillators amplifiers	
RF Front-end Systems	
System	Requirement
Reconfigurable radio	<ul style="list-style-type: none"> <li>• High performance RF switch</li> <li>• Small foot print</li> <li>• Multiple switching networks</li> </ul>
Phased array	<ul style="list-style-type: none"> <li>• Low-loss phase shifters</li> <li>• Small footprint switches</li> </ul>
Constrained power/energy radio	<ul style="list-style-type: none"> <li>• Low power switching</li> <li>• Low static energy</li> </ul>



## 2.1. Main topology of RF switch

RF switches are categorized by the number of inputs and outputs, *i.e.*, number of poles and throws respectively. The number of poles and throws vary accordingly to the use of the RF switch.

A Single Pole Single Throw (SPST) switch consist of one input and one output. This type of switch is the only one fabricated in this thesis. The SPST switch serves as on-off switch in a circuit allowing the signal to pass through in the ON state and stopping it in the OFF state. An example of the most used SPST switch technology is reported by M. Uzunkol et G. M. Rebeiz [1]. (Fig. 1a)

## 3. Technologies used nowadays

This part focuses on the presentation of mature and commercially available technologies of RF switches. First, we will talk about solid-state technology. Solid-state switches are made by using a semiconductor. Semiconductors are materials with electrical conductivity laying in a range between conductors (usually metals) and insulators. A highly tunable conductivity in semiconductors is usually achieved by means of doping, *i.e.*, the introduction of impurities to a material in a controllable way. N-type doping can be realized with chemical elements, which behave as donors and give free electrons to a semiconductor, while P-type doping with chemical elements which accept electrons. Semiconductor materials mainly utilized for RF devices are from the III-V group such as gallium arsenide (GaAs)[4] or indium phosphide (InP) [5]. A semiconductor RF switch can also be based on PIN diodes and Field Effect Transistors (FETs), such as high electron mobility transistors (HEMTs) and CMOS devices. MEMS switches are another type of commercially available of RF switches.

### 3.1. PIN diode - short description

A PIN diode is a semiconductor device. It is composed of an intrinsic zone with high resistivity sandwiched between two other zones with p-and n-type doping. This diode possesses two states. The direct polarization or ON state happen when a positive voltage is applied to the diode directly, thus RF signal is allowed to pass through and the insertion loss is low. The

reverse polarization or OFF state happens when the diode is under reversed bias. In this case, the PIN diode does not let the signal go through and possess a high isolation. PIN diodes are used as power limiter [6], [7], phase shifters [8], [9] or as a SPDT RF switches [10], [11]. Fig. 2 shows the structure of a PIN diode used in a shunt configuration of a SPST RF switch, under direct bias and (Fig. 2a) and reverse bias (Fig. 2b) [10].

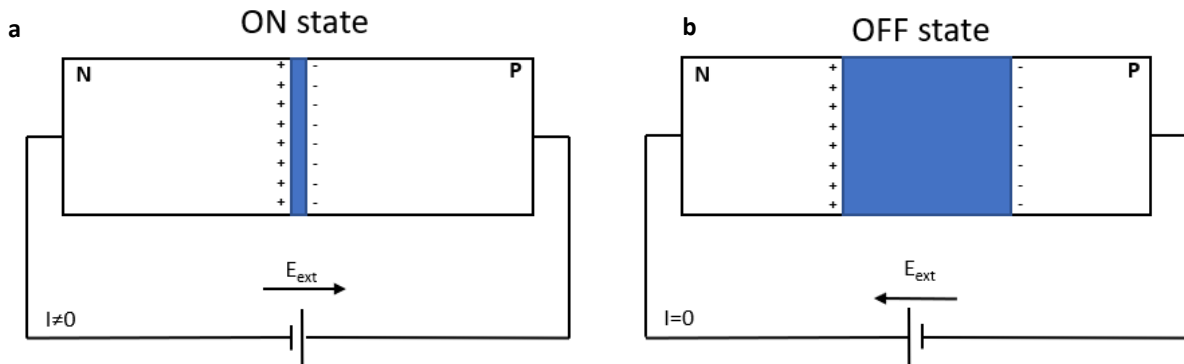


Figure 2 Representation of a PIN diode in (a) direct polarization (ON state) and (b) in reverse polarization (OFF state)

The advantage of PIN diode lies in its high-speed switching with value on the order of 100 ns. However, a bias current is required to maintain the ON state. As a consequence, there is a continuous power consumption for this state.

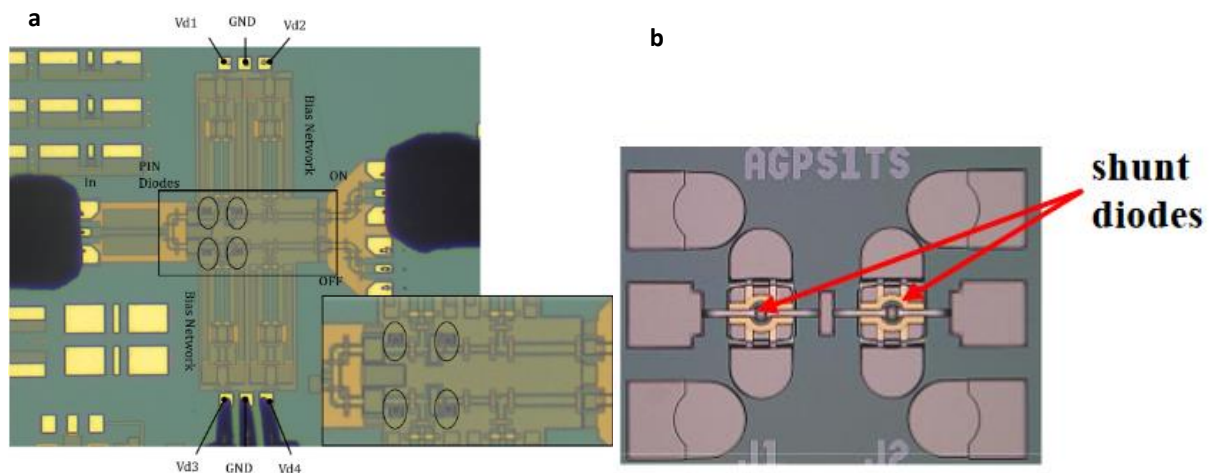


Figure 3 SPDT RF switches with PIN diode from [11] SPST RF switch with 2 shunt diodes from [10]

Regarding the FOM of a typical commercially available PIN diodes: the frequency range of a PIN diode a switch spans from 0.3 to 18 GHz, it possesses an insertion loss of -3.7 dB and an isolation of -55 dB with a switching time of 100ns. The power consumption is around 200 mW

for the commercially available model presented.<sup>1</sup> For higher frequency devices, a single pole double throw (SPDT) device can achieve an insertion loss of 2.8 dB at 85 GHz and an isolation of 30 dB at 85 GHz from [11]. (Fig. 3)

### 3.2. *FET - Short description*

This part focuses on a brief description of an FET transistor, the HEMT, as some RF switches available commercially are made with this technology. It follows the CMOS technology that is most used as RF switches nowadays.

An FET is an electronic semiconductor device, which uses the electric field effect to control the current flow. An FET has three terminals: source, drain and gate. As mentioned above, the FET controls the current flow through the voltage applied to its gate. Thus, altering the conductivity of the channel between the drain and the source electrodes.

#### 3.2.1. *HEMT devices as RF switches*

High-electron mobility transistors (HEMT) are field-effect transistors that works by incorporating a junction between two materials with different bandgaps as the channel. Conventional HEMTs are generally made out of a combination of GaAs with AlGaAs (Fig. 4) and it is used here for illustration. It is worth to mention that today, many other efficient HEMT device families exist.

---

<sup>1</sup> <https://www.pulsarmicrowave.com/product/switch/SW1AD-33>

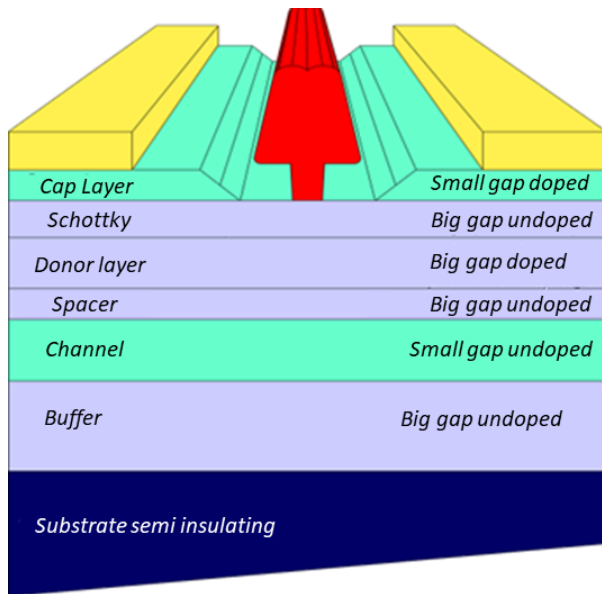


Figure 4 Schematic cross section of a conventional HEMT

The HEMT works by applying a tension to the gate that controls the density of the charge carriers in the channel (2D electron gas). The density of the charge carriers in the 2D electron gas then controls the drain current. Depending on the value on the gate bias, the device switches from its ON state to its OFF state or from its OFF state to its ON state. Fig. 5 displays a HEMT RF switch working in the 59-77GHz frequency range and its implementation [12].

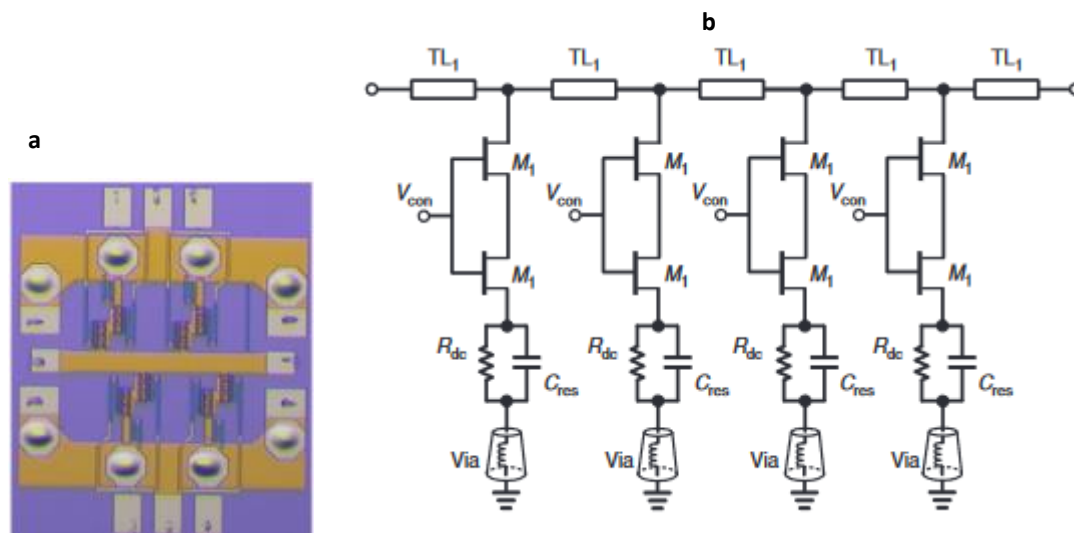


Figure 5 Photography of the chip of a HEMT-based RF switch and its implementation from [12]

This type of device is used for high speed, high frequencies and microwave circuits and it can be used as an RF switch.[13] It possesses a low insertion loss <1,1 dB and an high isolation > 25dB over a frequency range of 59-77 GHz. It has a switching speed in the order of nanosecond.

### 3.2.2. CMOS - the most available RF switches

Complementary Metal Oxide Semiconductor (CMOS) is the main technology used for RF switches nowadays because of its low insertion loss and high isolation.

#### 3.2.2.1. CMOS operational principles

CMOS is a type of MOSFET composed of complementary pairs of nMOS and pMOS. When the nMOS is ON, the pMOS is OFF and vice versa. The power in this case is only consumed during the switching transitions between these two states.

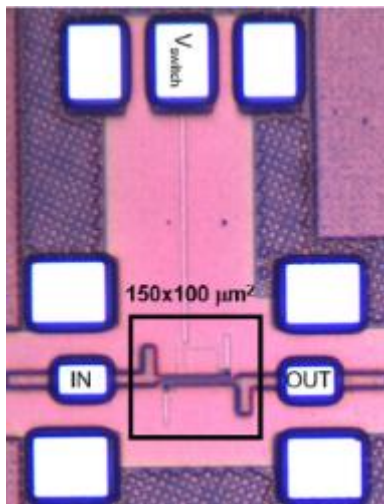


Figure 6 Top view of a CMOS with parasitic devices from [14]

Fig. 6 shows an SPST RF CMOS switch from [14] using a coupled-line topology with MOSFET employed as variable impedance components. Most of the high frequency CMOS RF switches are based on coupled lines. In literature CMOS RF switches are reported to work with coupled lines at high frequencies, *i.e.*, in a frequency range of 250-320 GHz. They possess a high insertion loss of 4 dB at 303 GHz and an isolation of 40.3 dB at 303 GHz [14].

#### 3.2.2.2. CMOS Benefits for RF switch

CMOS possess some benefit that makes it the best RF switch for the actual use thanks to a method of fabrication that was matured for decade and a close to zero static power dissipation. The main benefits are:

- Low fabrication cost

- Large-scale integration
- Compact device size with a gate size down to tens of nanometres
- Low static power consumption on the order of 0.1 mW
- Low switching time in the order of nanoseconds
- Low insertion loss around 0.4 dB at 1 GHz and high isolation around 40 dB at 1 GHz for commercial switch in the frequency range from 0 to 3.5 GHz.<sup>2</sup>

Regardless of the listed advantages, CMOS technology suffers from limitations like their low power handling (maximum 15 dBm) caused by their low voltage operation and their narrow band operation for coupled-line-based designs at high frequency (over 100 GHz). [15] Thus, other RF switching technologies need to be improved or need to be developed to overcome existing challenges.

### 3.3. MEMS switching devices

MEMS switches are surface micromachined devices, they consist of anchor points and a moving part that moves according to external stimuli provided by an actuator. They are classified depending on the source of the physical phenomenon that produce the stimuli to generate the mechanical movement which can be electrostatic, thermal, piezoelectric and magnetostatic.

Considering RF MEMS, two types of MEMSs - with ohmic contacts and with capacitive contacts - will be presented.

#### *3.3.1. RF MEMS with ohmic contact -serial contact*

MEMSs with ohmic contacts possess a contact zone, where the cantilever and the electrode are put in contact with each other when the device switch into its ON state. In the OFF state, the cantilever is suspended on top of the contact zone. The air gap between the cantilever and the contact has a capacitance,  $C_{OFF}$ . Switching from OFF to ON occurs when the actuation

---

<sup>2</sup> <https://www.mouser.fr/new/infineon/Infineon-bgsx44ma12-rf-cmos-switch/>

electrode is biased. Thus, an electrostatic force is formed and attracts the cantilever forming the contact with the electrode. The metal-metal contact is characterized by the resistance,  $R_{ON}$ .

Fig.7 shows an example of a MEMS with ohmic contact, where the contact between the cantilever and the contact electrode is realized by means of a microspring. [16]

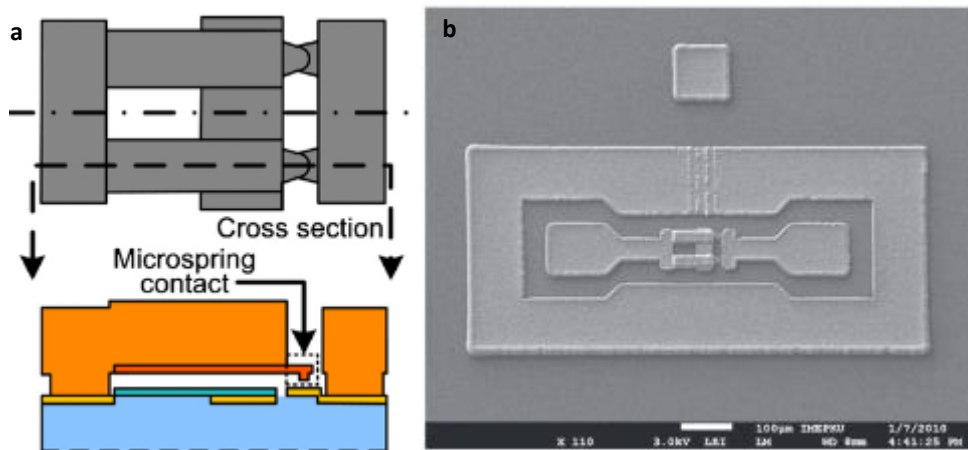


Figure 7 (a) Schematic of a microspring contact in a metal-to-metal contact MEMS switch configuration (b) SEM image of the fabricated switch from [16]. The microspring is put in contact with the metallic part to switch the device to its ON state. In the OFF, the microspring lays on top of the metallic contact without touching it.

This switch provides: from 0 to 20 GHz, an insertion loss of 0.2 dB and an isolation of 22 dB at 20 GHz. The actuation voltage for this device is around 50 V.

### 3.3.2. RF MEMS with capacitive contact- parallel circuit

MEMSs with capacitive contacts are similar to the one with ohmic contacts. The difference is the presence of a dielectric deposited on top of the signal electrode, as shown on Fig. 8a changing its capacitance. The circuit model of this type of switch is different compared to the one presented at the beginning of this chapter. This type of switch is characterized by a  $C_r$ -ratio where  $C_r = C_{OFF}/C_{ON}$ . A high  $C_r$  ratio is required for capacitive MEMSs to be used as RF switches.

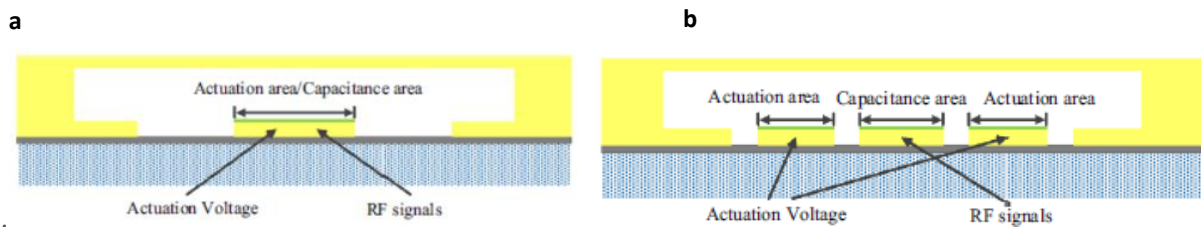


Figure 8 (a) Classic capacitive MEMS device (b) Capacitive MEMS switch with specific design from [17]

In the OFF state, the cantilever and the capacitance area are separated by air and the dielectric, the  $C_{OFF}$  capacitance is high. By applying a voltage to the actuation pad, the cantilever is attracted by the electrostatic force and makes a contact with the dielectric on top of the actuation pad. The device attains its  $C_{ON}$  capacitance and switches from its OFF state to the ON state. An improved capacitive MEMS device is shown on Fig. 8b and 9. This device is embedded in a coplanar waveguide for RF application, where the actuation zone surrounds the capacitive area [17].

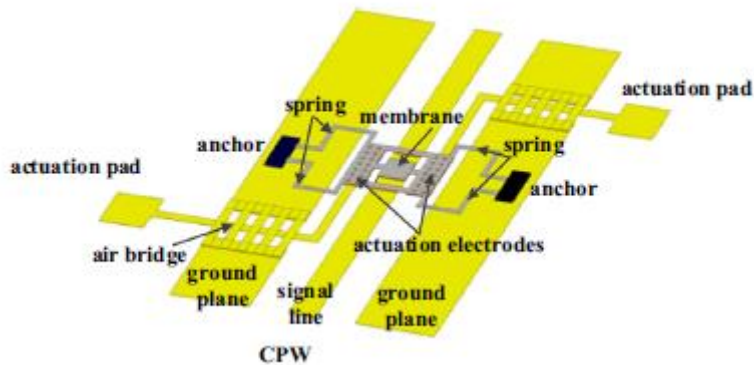


Figure 9 Structure of the MEMS switch from [17]. The coplanar waveguide (yellow) embeds the switching area

### 3.3.3. MEMS for high frequency

Recently made state-of-the-art MEMS RF switches are designed to work at high frequency. For example, the switch, displayed in Fig. 10, operates with a signal at 240-325 GHz and possess some advantage: MEMS RF switches can achieve an extremely low IL (<0.5 dB at 235 GHz) and high isolation (25 dB at 235 GHz). Overall this kind of devices shows high linearity [16]–[22]. MEMS RF switches have low power consumption due to voltage actuation.



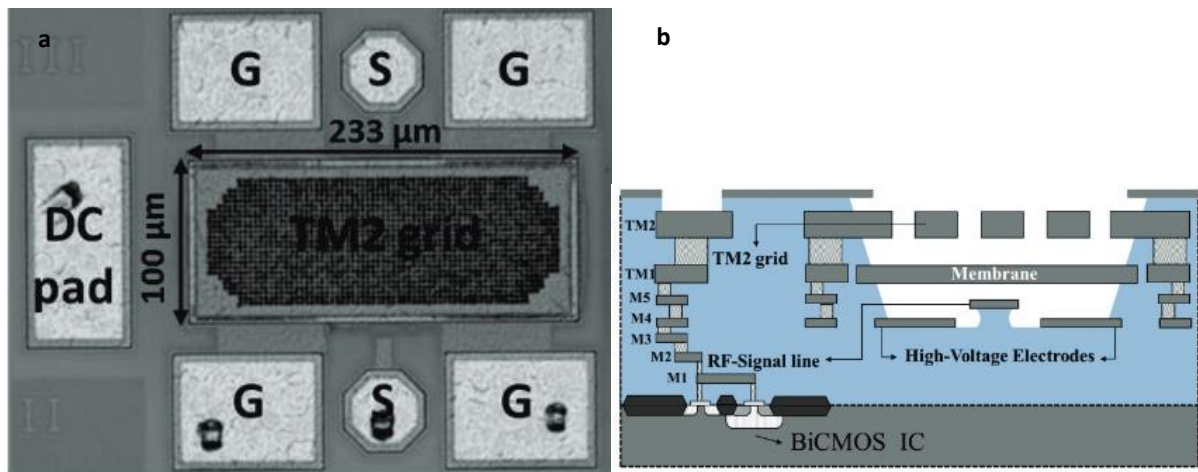


Figure 10 (a) Optical image of a 240GHz RF MEMS switch and (b) schematic and cross section of the RF MEMS from [18]

However, MEMS RF switches have the following drawback: regardless recent achievements in commercially available MEMS switches operating at voltage of 3 V (ADGM1003)<sup>3</sup>, most of MEMS devices require a high actuation voltage (> 30 V). Low switching speed (around 120 μs) and relatively to solid-state switches low power handling (around 30 dBm) are also considered as limitation. Finally, they are really sensitive to exterior contamination and need to be protected by encapsulation. Nevertheless, this switch technology is widely and successfully used in reconfigurable antennas [23], [24].

#### 4. Emerging switching technologies

The development of emerging technologies based on different resistive states to store information has shown promising results [2]. This part reviews four different emerging switching technologies starting with metal insulator transition (MIT) switches that is a volatile technology. It is then followed by three other nonvolatile emerging technologies that can be used for RF switches such as phase change material (PCM) switches, conductive bridge (CB) switch technology and finally 2D-based switches. The nonvolatility of a device implies that it does not consume energy to maintain its current state. This term is borrowed from memory

<sup>3</sup> Web address: <https://www.analog.com/en/products/adgm1003>

device where this technology comes from. The description of 2D-based RF switches that has been recently developed is finalizing the section.

#### 4.1. Description of metal insulator transition (MIT) switch

Vanadium dioxide ( $\text{VO}_2$ ) is a favourable material for RF switches devices due to its metal to insulator and insulator to metal transition. This phenomenon occurs when the  $\text{VO}_2$  reaches a critical temperature of  $68^\circ\text{C}$  and becomes conductive. This temperature needs to be maintained to keep the device in the ON state. An RF switch is fabricated by separation of two metal electrodes by a  $\text{VO}_2$  zone (Fig. 11). MIT RF switches possess low insertion loss, a high isolation and a high switching speed. However, the power consumption of the device is high due to the need to maintain the temperature at  $68^\circ\text{C}$  in the ON state.

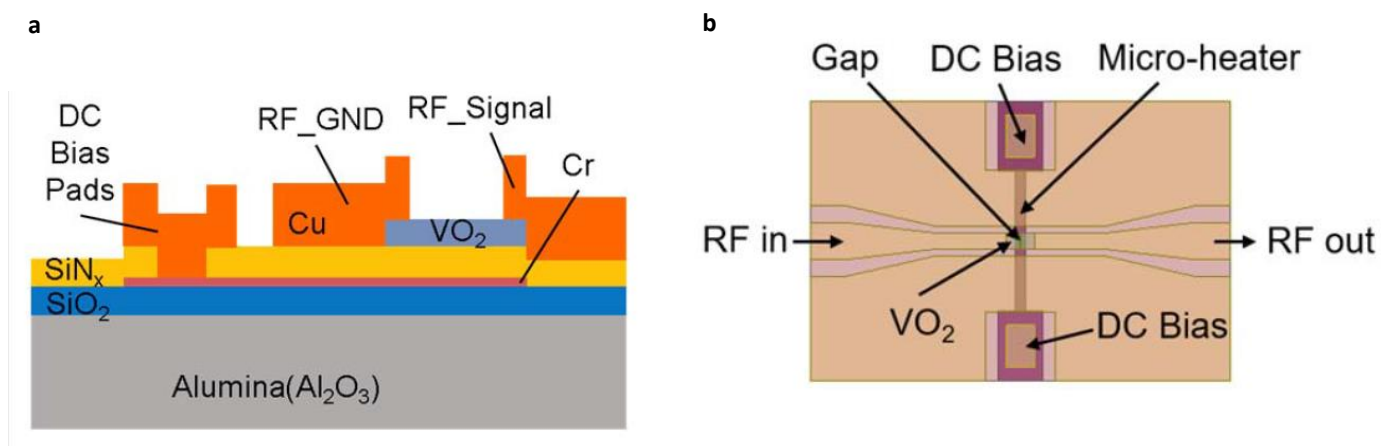


Figure 11 MIT RF switch (a) cross view and (b) top view after fabrication embedded in a coplanar waveguide from [25]

For the  $\text{VO}_2$  switch from [25], the insertion loss and isolation are 0.5 dB and 25 dB respectively at 20 GHz and simulations suggest that it could operate up to 75 GHz. The state-of-the-art for  $\text{VO}_2$  switch exhibit a frequency range from 210 GHz to 290 GHz with a insertion loss and an isolation of 1.5 dB and 12 dB respectively at 290 GHz.[26]

## 4.2. Phase change material (PCM) switches

A PCM switch uses phase change materials such as GeTe. A phase change material is a material that has two – or more – distinct state. For the GeTe, the two states are its amorphous phase that is a High Resistive State (HRS), and its crystalline phase that is a Low Resistive State (LRS). The phase transition is controllable by changing the temperature of the active material (Fig. 12). In short, when the GeTe is in its crystalline phase, the switch is in its ON state. To switch it, the device is heated for a short time above the melting temperature,  $T_f$ , and suddenly freezed, then GeTe becomes amorphous and the switch is in its OFF state. The device is nonvolatile meaning that its state will not change if it is not submitted to an exterior stimulus, here a temperature change. To turn the device back ON, it is heat up to the temperature of crystallization,  $T_c$ , so that the GeTe crystallize back and the device goes in its LRS. A high resistance in the amorphous state of the material and a low resistance in the crystalline phase makes PCM a viable candidate for RF switches.

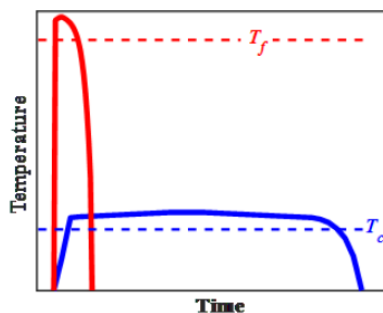


Figure 12 Cycle of PCM switch from [27]. In dashed red is represented the melting temperature,  $T_f$ , of GeTe. Above this temperature the GeTe changes phase from its crystalline state to its amorphous state. In blue is represented the crystallization temperature of GeTe. By heating the device, a slightly above this temperature, the phase of the GeTe changes from amorphous to crystalline.

PCMs are nonvolatile device and possess a retaining time of a few years. A different  $R_{ON}/R_{OFF}$  ratio and endurance can be achieved by stoichiometric evolution. Fig. 13 shows an example of one of the PCM material switches made with GeTe, it is basically a coplanar waveguide that guide the RF signal with a DC part for the heating of the GeTe.

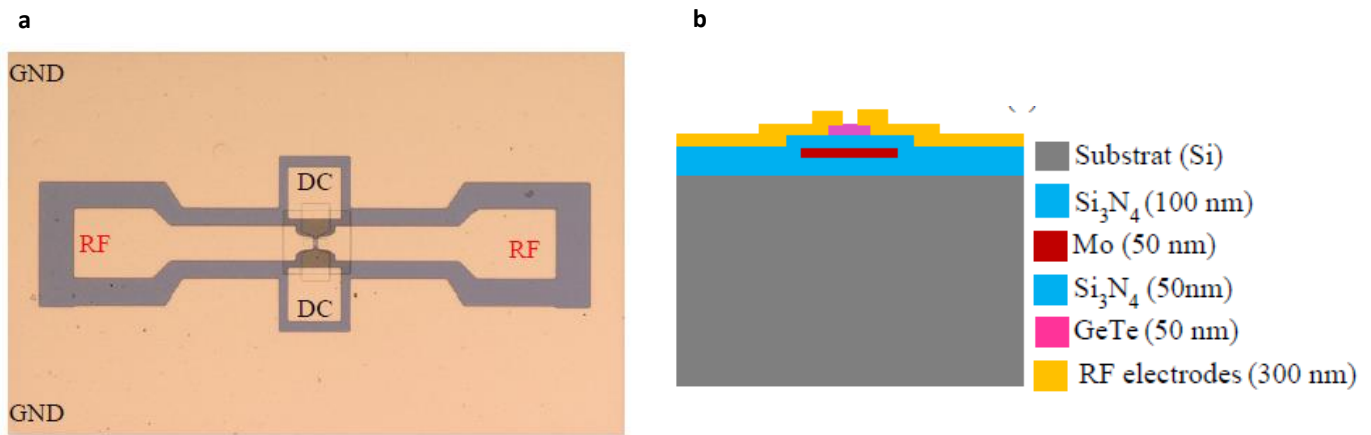


Figure 13 (a) Top view and (b) cross view of PCM switch from [27]

The figure-of-merit of PCM switches presented in [27] are: from 0 to 20 GHz with an insertion loss of 2 dB at 20 GHz, an isolation of 18 dB at 20 GHz, that is a typical performance.

### 4.3. Conductive bridge switches

Conductive-Bridge devices (CB) are also known as electrochemical metallization memory. They are composed of two asymmetric metal electrodes, one active and one inert, and separated from each other by a small gap [28] (Fig. 14) or by an insulating layer [29]. Fig. 14 shows a gap type CB [28].

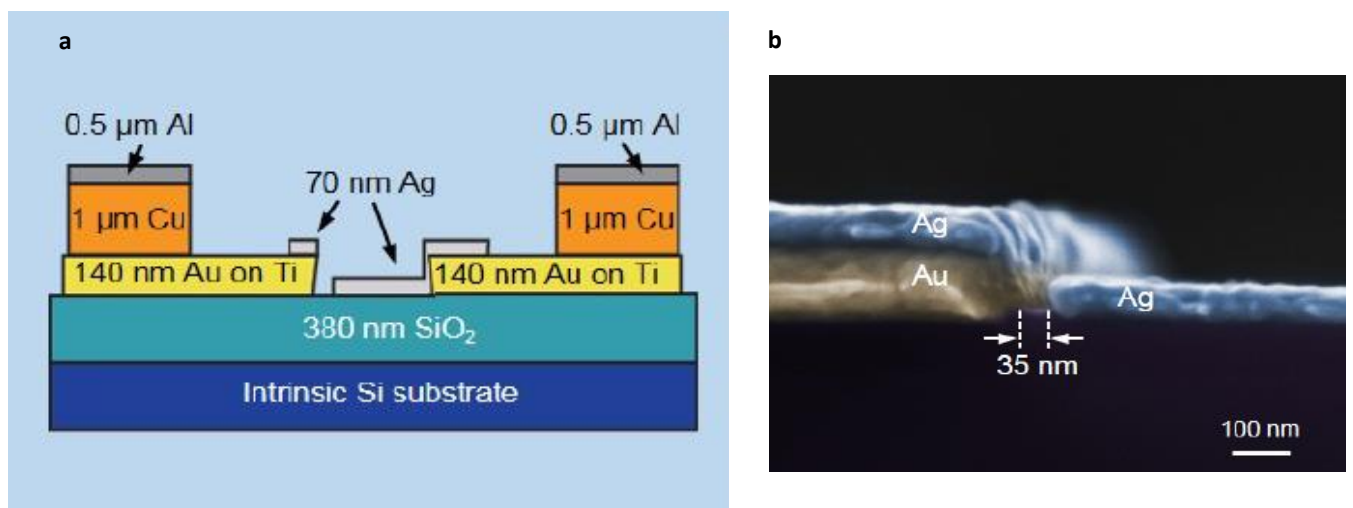


Figure 14 (a) cross view of a gap CBRAM switch. (b) Colored view of a SEM image of a CB switch from [28]

The switching mechanism is based on a redox process. A metallic filament is formed by ion migration from the active electrode to the inert electrode when an external electric field is applied to them. This process is named SET. Under reversed electric field, the metallic filament is ruptured and dissolves itself as the ions migrate back to the active electrode. This process is named as RESET. This switch is also embedded into a CPW for RF operation (Fig. 15).

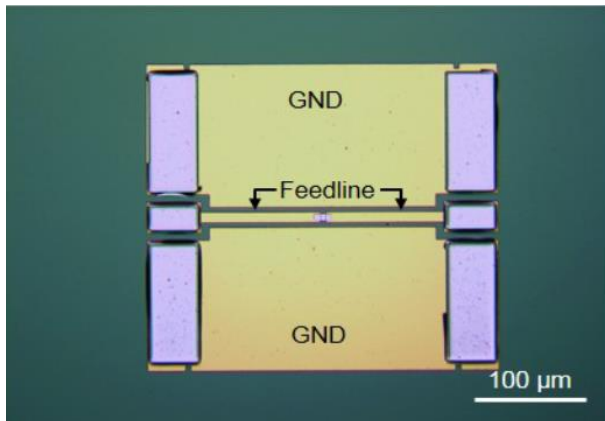


Figure 15 Optical image of an RF CB switch in a CPW configuration

A SEM image of the filament between both electrodes is shown in Fig. 16. [28]

The state-of-the-art possesses the following figures of merit: a frequency range measured till 110 GHz, an insertion loss of 0.33 dB and an isolation of 29.8 dB measured at 40 GHz. For the intrinsic parameters, an  $R_{ON}$  of 3.6  $\Omega$  and a  $C_{OFF}$  of 1.37 fF were determined.

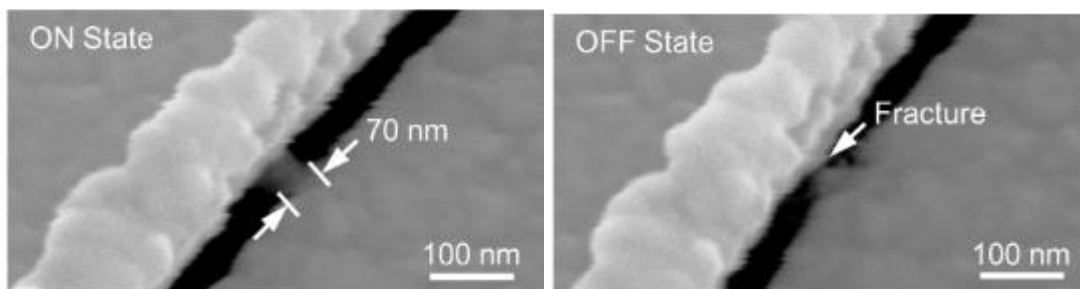
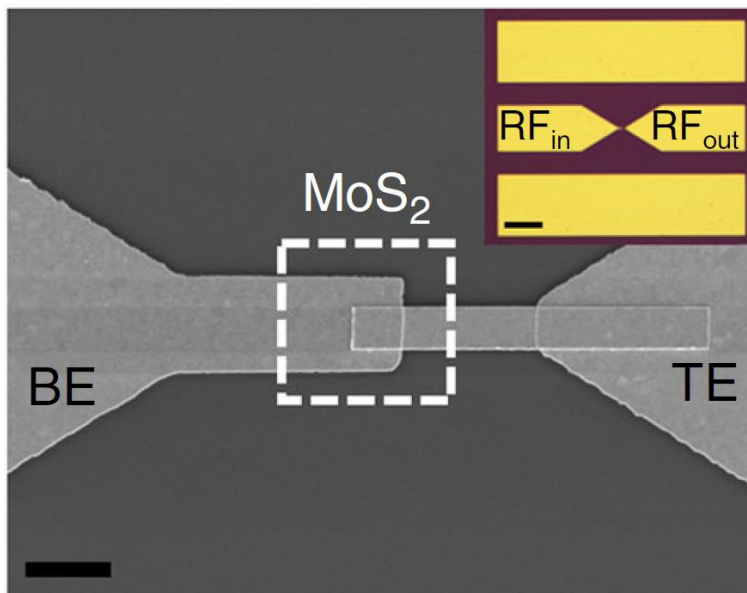


Figure 16 SEM image of the gap switch in its (a) ON state and (b) OFF state from [28]. In (a), a filament is observed that link both electrodes.

#### 4.4. Resistive switching observed with 2D material

This is the last type of RF switches that is presented and the main focus of this thesis.

Resistive switching in 2D materials as monolayer hexagonal boron nitride (hBN) or Tungsten disulphide ( $WS_2$ ) or molybdenum disulphide ( $MoS_2$ ) has been demonstrated recently [30]. Following this seminal work, RF switches based on the 2D material are currently researched for high frequency and memory application. Such 2D switches consist of 2D material sandwiched by two metal electrodes (Fig. 17). For RF application, they are embedded into coplanar wave guides. Devices are usually fabricated utilizing CVD grown 2D materials, which are then transferred on the top of the electrodes from the growth substrate. Switches based on 2D materials exhibit remarkable high frequencies performances due to the ultimate thickness of the 2D materials, thus they become promising for RF application as well as for memory application.



*Figure 17 SEM image of 2D switch and inset: microscopy image of 2D switch CPW from [31]. A 2D material (dashed square), is sandwiched between a bottom electrode (BE) and a top electrode (TE).*

The switch is nonvolatile meaning that the switch retains its ON state or OFF state without consuming any power. The RF switch in [29] possesses a correct insertion loss (1.2 dB) and isolation (12 dB) at 50 GHz. The endurance of these devices requires an improvement as it is still low [32]. The mechanism behind the 2D RF switches were not investigated at the beginning of my thesis and will be explained in chapter 3.

## 4.5. Application for emerging technology RF switches

New emerging RF switches using the technology presented above are under wide investigation nowadays because of their:

- High state-of-the-art FOM
- Low switching energy
- Nonvolatility
- Small footprint
- Low energy necessary for activation

Possible applications for the resistive RF switch are summarized in Table 1 in the beginning of the chapter [2]. Applications are various, from fundamental elements such as tunable inductors or capacitors as part of subsystems like switching networks or phase shifters in RF front-end modules because of their low  $R_{ON}$  and low  $C_{OFF}$ .

## 5. Comparison between different RF switches

Table 2 resumes different figure-of-merits of the devices from the state-of-the-art literature for the technologies discussed above.

Table 2 Comparison table of RF performance of different RF switch technologies

Ref	Technology	IL (dB)	IS (dB)	Bandwidth (GHz)	R <sub>ON</sub> (Ω)	C <sub>OFF</sub> (fF)	F <sub>c</sub> (THz)	Control voltage (V)
[12]	70nm GaAs m-HEMT SPST	-1.1	-25	59-77	5.4	36	0.81	/
[14]	65nm CMOS SPST	-4	-40	250-320	/	/	/	/
[33]	CMOS SOI SPST	<-3	-50	0-43	/	/	/	< 3
[16]	MEMS Ohmic contact	-0.2	-22	0-20	/	/	/	50
[17]	MEMS capacitive contact	-0.3	-20.5	0-40	/	/	/	18.3
[18]	MEMS BiCMOS	-0.44	-24.6	220-325	/	/	/	70
[10]	SPST PIN diode	-0.3	-50	0-50	/	/	/	/
[11]	SPDT PIN diode	-2.8	-30	55-105	10	23	0.69	1.8
[25]	SPST VO <sub>2</sub> switch	-0.4	-28	0-20	/	/	/	15
[26]	SPST VO <sub>2</sub> switch	-1	-12	210-290	/	/	/	1
[27]	SPST GeTe switch	-2	-15.5	0-20	25	10	0.63	/
[34]	GeTe switch	-0.6	>20	0-67	/	/	/	/
[37]	GeTe switch	-0.15	>25	0-40	1.1	6.8	11	7.5
[35]	CB switch	-1.1	-25	0-3	2	1681	0.04	16
[28]	CB switch	-0.3	-30	0-40	2.6	1.45	42.2	3
[32]	MoS <sub>2</sub> Atomristor	-0.25	-29	0-50	11	7.7	1.87	1



At high frequency (around 300 GHz), some devices possess issues with for example high insertion loss for CMOS or high voltage needed for MEMS technology. On the other hand, we can observe that emerging technologies like CB switch, PCMs and finally 2D switch feature high FOMs around 40-60 GHz frequency. Further study is then needed to improve them and see their functionality in the 300 GHz frequency range.

## 6. Conclusion

In this chapter, the figure-of-merits and the topology of RF switches are introduced. Furthermore, for 6G and very high frequency applications, commercially available switches have limitations such as the high voltage needed for MEMS devices or the narrow operation band and low power handling of CMOS devices.

Therefore, emerging technologies are an active research field, starting with MIT VO<sub>2</sub> switches that are promising thanks to their excellent insertion loss, isolation and their capability to work at high frequency. Nevertheless, VO<sub>2</sub> requires to be heated up to 68°C to maintain its ON state, causing a high energy consumption and limiting the scalability. PCM devices are nonvolatile and feature a good insertion loss and isolation over a relative broad frequency range but a reduction of the parasitic capacitance is necessary to reach higher frequency. That is also the case for CB that shows great expectation from its insertion loss and isolation as well. However, both these technologies need to reach higher frequency to be able to match the requirement for future 6G applications [36]. Finally, the latest and most recent switch presented in this thesis, the 2D material based switch possess an enormous potential because of the absolute thickness of the 2D material and great scaling with frequency and its simple switching control, despite a first operation report limited at 50GHz [32].

The goal of this thesis is to develop and optimize nonvolatile 2D-based RF switches to assess their potential for high frequency application (above 100 GHz) for 5G and beyond. To match the requirement for 6G, the study of metallic electrode, thickness of the 2D material, scaling need to be carried out. The objective is to improve our understanding of the device to match requirement for real application and to comply with constraints imposed by future integration in a semiconductor production line.

## 7. References

- [1] D. M. Pozar, *Microwave Engineering, 4th Edition*. Wiley, 2011.
- [2] N. Wainstein, G. Adam, E. Yalon, et S. Kvatinsky, « Radiofrequency Switches Based on Emerging Resistive Memory Technologies - A Survey », *Proc. IEEE*, vol. 109, n° 1, p. 77-95, jan. 2021, doi: 10.1109/JPROC.2020.3011953.
- [3] M. Uzunkol et G. M. Rebeiz, « 140–220 GHz SPST and SPDT Switches in 45 nm CMOS SOI », *IEEE Microw. Wirel. Compon. Lett.*, vol. 22, n° 8, p. 412-414, agu. 2012, doi: 10.1109/LMWC.2012.2206017.
- [4] A. Gopinath et J. B. Rankin, « GaAs FET RF switches », *IEEE Trans. Electron Devices*, vol. 32, n° 7, p. 1272-1278, 1985, doi: 10.1109/T-ED.1985.22111.
- [5] J. S.-C. Chien et J. F. Buckwalter, « Compact, High-Isolation 110-140-GHz SPST and SPDT Switches Using a 250-nm InP HBT Process », in *2022 IEEE/MTT-S International Microwave Symposium - IMS 2022*, 2022, p. 152-155. doi: 10.1109/IMS37962.2022.9865636.
- [6] E. Gatard, R. Sommet, P. Bouysse, R. Quere, M. Stanislawiak, et J.-M. Bureau, « High power S band limiter simulation with a physics-based accurate nonlinear PIN diode model », in *2007 European Microwave Integrated Circuit Conference*, 2007, p. 72-75. doi: 10.1109/EMICC.2007.4412650.
- [7] A. V. Bezruk, A. Y. Yushchenko, G. I. Ayzenshtat, V. G. Bozhkov, et V. I. Perfiliev, « The microwave power limiter based on pin-diodes for the frequency range of 100–110 GHz in form of waveguide MIC », in *2013 23rd International Crimean Conference « Microwave & Telecommunication Technology »*, sept. 2013, p. 74-75.
- [8] J. Zhang, S. W. Cheung, et T. I. Yuk, « A compact 6-bit phase shifter with high-power capacity based on composite right/left-handed transmission line », in *The 40th European Microwave Conference*, sept. 2010, p. 437-440. doi: 10.23919/EUMC.2010.5616000.
- [9] M. U. Nazir, M. Kashif, N. Ahsan, et Z. Y. Malik, « PIN diode modelling for simulation and development of high power limiter, digitally controlled phase shifter and high isolation SPDT switch », in *Proceedings of 2013 10th International Bhurban Conference on Applied Sciences Technology (IBCAST)*, 2013, p. 439-445. doi: 10.1109/IBCAST.2013.6512197.
- [10] T. Boles, J. Brogle, D. Hoag, et D. Curcio, « AlGaAs PIN diode multi-octave, mmW switches », in *2011 IEEE International Conference on Microwaves, Communications*,

- Antennas and Electronic Systems (COMCAS 2011)*, nov. 2011, p. 1-5. doi: 10.1109/COMCAS.2011.6105783.
- [11] V. Vassilev, A. Vilenskiy, H. -T. Chou, M. Ivashina, et H. Zirath, « A 55-105 GHz PIN Diode SPDT Switch », in *2021 International Symposium on Antennas and Propagation (ISAP)*, oct. 2021, p. 1-2. doi: 10.23919/ISAP47258.2021.9614359.
- [12] Y. Kim et S. Jeon, « Mm-wave single-pole single-throw m-HEMT switch with low loss and high linearity », *Electron. Lett.*, vol. 56, n° 14, p. 719-721, 2020, doi: <https://doi.org/10.1049/el.2020.0969>.
- [13] G. Shen, H. Zhu, Q. Xue, et W. Che, « An 11–40-GHz High-Power Switch With Miniaturized High-Order Topology Using 100-nm GaN-on-Si HEMTs », *IEEE Trans. Electron Devices*, p. 1-8, 2022, doi: 10.1109/TED.2022.3204511.
- [14] J. Kim, S. Kim, K. Song, et J.-S. Rieh, « A 300-GHz SPST Switch With a New Coupled-Line Topology in 65-nm CMOS Technology », *IEEE Trans. Terahertz Sci. Technol.*, vol. 9, n° 2, p. 215-218, 2019, doi: 10.1109/TTHZ.2019.2898815.
- [15] J. Sobolewski et Y. Yashchyshyn, « State of the Art Sub-Terahertz Switching Solutions », *IEEE Access*, vol. 10, p. 12983-12999, 2022, doi: 10.1109/ACCESS.2022.3147019.
- [16] B. Liu, Z. Lv, X. He, M. Liu, Y. Hao, et Z. Li, « Improving performance of the metal-to-metal contact RF MEMS switch with a Pt–Au microspring contact design », *J. Micromechanics Microengineering Struct. Devices Syst.*, vol. 21, n° 6, p. 9, june 2011, [En ligne]. Disponible sur: [http://inis.iaea.org/search/search.aspx?orig\\_q=RN:47010002](http://inis.iaea.org/search/search.aspx?orig_q=RN:47010002)
- [17] M. Li, J. Zhao, Z. You, et G. Zhao, « Design and fabrication of a low insertion loss capacitive RF MEMS switch with novel micro-structures for actuation », *Solid-State Electron.*, vol. 127, p. 32-37, jan. 2017, doi: 10.1016/j.sse.2016.10.004.
- [18] S. T. Wipf *et al.*, « 240 GHz RF-MEMS switch in a 0.13  $\mu\text{m}$  SiGe BiCMOS Technology », in *2017 IEEE Bipolar/BiCMOS Circuits and Technology Meeting (BCTM)*, 2017, p. 54-57. doi: 10.1109/BCTM.2017.8112910.
- [19] C.-Y. Lin, C.-C. Hsu, et C.-L. Dai, « Fabrication of a Micromachined Capacitive Switch Using the CMOS-MEMS Technology », *Micromachines*, vol. 6, n° 11, 2015, doi: 10.3390/mi6111447.
- [20] A. Persano, A. Tazzoli, P. Farinelli, G. Meneghesso, P. Siciliano, et F. Quaranta, « K-band capacitive MEMS switches on GaAs substrate: Design, fabrication, and reliability », *Spec. ISSUE 23rd Eur. Symp. Reliab. ELECTRON DEVICES Fail. Phys. Anal.*, vol. 52, n° 9, p. 2245-2249, sept. 2012, doi: 10.1016/j.microrel.2012.06.008.

- [21] Y. Zhu, L. Han, M. Qin, et Q. Huang, « Novel DC-40GHz MEMS series-shunt switch for high isolation and high power applications », *Sens. Actuators Phys.*, vol. 214, p. 101-110, agu 2014, doi: 10.1016/j.sna.2014.04.024.
- [22] M. Fernandez-Bolanos Badia, E. Buitrago, et A. M. Ionescu, « RF MEMS Shunt Capacitive Switches Using AlN Compared to  $\text{Si}_3\text{N}_4$  Dielectric », *J. Microelectromechanical Syst.*, vol. 21, n° 5, p. 1229-1240, oct. 2012, doi: 10.1109/JMEMS.2012.2203101.
- [23] B. A. Cetiner, G. Roqueta Crusats, L. Jofre, et N. Biyikli, « RF MEMS Integrated Frequency Reconfigurable Annular Slot Antenna », *IEEE Trans. Antennas Propag.*, vol. 58, n° 3, p. 626-632, march 2010, doi: 10.1109/TAP.2009.2039300.
- [24] D. E. Anagnostou *et al.*, « Design, fabrication, and measurements of an RF-MEMS-based self-similar reconfigurable antenna », *IEEE Trans. Antennas Propag.*, vol. 54, n° 2, p. 422-432, feb. 2006, doi: 10.1109/TAP.2005.863399.
- [25] J. Jiang, G. Chugunov, et R. R. Mansour, « Fabrication and characterization of VO<sub>2</sub>-based series and parallel RF switches », in *2017 IEEE MTT-S International Microwave Symposium (IMS)*, june 2017, p. 278-280. doi: 10.1109/MWSYM.2017.8059096.
- [26] C. Hillman, P. Stupar, et Z. Griffith, « Scaleable vanadium dioxide switches with submillimeterwave bandwidth: VO<sub>2</sub> switches with improved RF bandwidth and power handling », in *2017 IEEE Compound Semiconductor Integrated Circuit Symposium (CSICS)*, 2017, p. 1-4. doi: 10.1109/CSICS.2017.8240450.
- [27] A. Hariri, A. Crunteanu, C. Guines, C. Hallepee, D. Passerieux, et P. Blondy, « Double-Port Double-Throw (DPDT) Switch Matrix Based on Phase Change Material (PCM) », in *2018 48th European Microwave Conference (EuMC)*, sept. 2018, p. 479-482. doi: 10.23919/EuMC.2018.8541405.
- [28] S. Pi, M. Ghadiri-Sadrabadi, J. C. Bardin, et Q. Xia, « Memristors as radiofrequency switches », in *2016 IEEE International Symposium on Circuits and Systems (ISCAS)*, may 2016, p. 377-380. doi: 10.1109/ISCAS.2016.7527249.
- [29] U. Celano *et al.*, « Conductive-AFM tomography for 3D filament observation in resistive switching devices », in *2013 IEEE International Electron Devices Meeting*, dec. 2013, p. 21.6.1-21.6.4. doi: 10.1109/IEDM.2013.6724679.
- [30] R. Ge *et al.*, « A Library of Atomically Thin 2D Materials Featuring the Conductive-Point Resistive Switching Phenomenon », *Adv. Mater.*, vol. 33, n° 7, p. 2007792, feb. 2021, doi: 10.1002/adma.202007792.

- [31] M. Kim *et al.*, « Zero-static power radio-frequency switches based on MoS<sub>2</sub> atomrystals », *Nat. Commun.*, vol. 9, n° 1, p. 2524, june 2018, doi: 10.1038/s41467-018-04934-x.
- [32] R. Ge *et al.*, « Atomrystal: Nonvolatile Resistance Switching in Atomic Sheets of Transition Metal Dichalcogenides », *Nano Lett.*, vol. 18, n° 1, p. 434-441, jan. 2018, doi: 10.1021/acs.nanolett.7b04342.
- [33] A. Eltaliawy et J. R. Long, « A Broadband, mm-Wave SPST Switch With Minimum 50-dB Isolation in 45-nm SOI-CMOS », *IEEE Trans. Microw. Theory Tech.*, vol. 69, n° 6, p. 2899-2906, 2021, doi: 10.1109/TMTT.2021.3066977.
- [34] T. Singh et R. R. Mansour, « Monolithic PCM Based Miniaturized T-type RF Switch for Millimeter Wave Redundancy Switch Matrix Applications », in *2019 IEEE MTT-S International Microwave Symposium (IMS)*, 2019, p. 658-660. doi: 10.1109/MWSYM.2019.8700946.
- [35] S. López-Soriano, J. Methapettyparambu Purushothama, A. Vena, et E. Perret, « CBRAM technology: transition from a memory cell to a programmable and non-volatile impedance for new radiofrequency applications », *Sci. Rep.*, vol. 12, n° 1, p. 4105, march 2022, doi: 10.1038/s41598-022-08127-x.
- [36] V. Petrov, T. Kurner, et I. Hosako, « IEEE 802.15.3d: First Standardization Efforts for Sub-Terahertz Band Communications toward 6G », *IEEE Commun. Mag.*, vol. 58, n° 11, p. 28-33, 2020, doi: 10.1109/MCOM.001.2000273.
- [37] A. Léon *et al.*, "RF Power-Handling Performance for Direct Actuation of Germanium Telluride Switches," in *IEEE Transactions on Microwave Theory and Techniques*, vol. 68, no. 1, pp. 60-73, Jan. 2020, doi: 10.1109/TMTT.2019.2946145.

# CHAPTER II Optimization of the 2D RF switch layout and RF measurement setup

# Table of Contents

CHAPTER II Optimization of the 2D RF switch layout and RF measurement setup .....	37
1. Introduction.....	39
2. RF study .....	39
2.1 Coplanar waveguide (CPW) .....	39
2.2 CPW study.....	40
2.2.1 CPW Dimension calculation and simulation .....	41
2.3 Structure of 2D switch.....	42
2.3.1 OPEN/SHORT structures simulation.....	43
2.3.2 Comparison between measurement and simulation for SHORT/OPEN structures	45
2.3.3 Optimisation up to 480 GHz.....	46
3. Description of DC and RF measurement procedure .....	48
3.1 RF measurement procedure .....	48
3.2 De-embedding procedure.....	49
3.2.1 Removing of the parasitic elements.....	51
3.2.2 Determination of the intrinsic parameters:.....	52
4. Conclusion .....	52
5. References.....	53

## 1. Introduction

This chapter focuses on the structure of the 2D-based RF switch. Our 2D RF switch is a device embedded in a coplanar waveguide (CPW). First, we design a CPW operating from 0-67 GHz. Then, based on the CPW design, two more structures are developed. The first one is an OPEN representing the OFF state of an ideal 2D switch and the second one is a SHORT representing the ON state of an ideal 2D switch. Both of these structures are simulated up to 67 GHz, fabricated, and simulation results are compared with measurements. These structures are used for de-embedding purpose to extract the intrinsic figure of merits (FOMs) of our devices. Finally, an optimization of the design of the CPW is realized to reach a working frequency of 480 GHz. This new design is then simulated from 0 to 480 GHz. To conclude this chapter, RF and DC measurement setup and procedures are presented, followed by an explanation of the de-embedding technique used to extract the FOMs of our devices.

## 2. RF study

### 2.1 Coplanar waveguide (CPW)

A coplanar waveguide is a transmission line mainly used in the design of microwave circuit. A CPW consists of a conductor strip called signal, which is located in the middle of two grounds. It is used for our device because they work at high frequencies without entailing any parasitic discontinuities [1]. Fig. 1 shows the cross section of a CPW where the yellow rectangles correspond to the metallic conductors and the blue one represents the dielectric substrate.



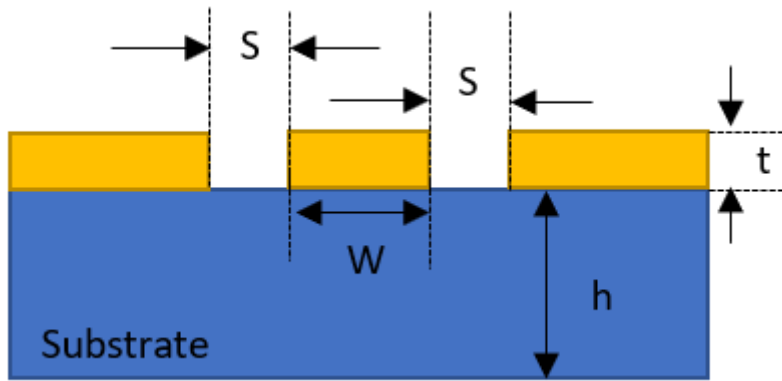


Figure 1 Cross section of a CPW, the metallic contacts are represented by the yellow rectangles and the substrate is represented by the blue rectangle. In this figure,  $W$  is the width of the signal,  $S$  the distance between the signal and the ground,  $h$  the thickness of the substrate and  $t$  the thickness of the contacts

The characteristic impedance of a CPW depends on the width of the conductor line ( $W$ ), the space ( $S$ ) between the conductor line and the ground, and on the dielectric permittivity of the substrate ( $\epsilon_r$ ). The metal thickness ( $t$ ) affects the ohmic losses. Main advantages of CPW are their low dispersion up to very high frequencies. [2] and the simple realization.

## 2.2 CPW study

The goal here is to determine the dimensions,  $W$  and  $S$ , required for an impedance of the line close to  $50 \Omega$ . These values are then used for the CPW embedding our 2D RF switch. The design is constrained by three factors: (i) ( $S$ ) has to be small to avoid parasitic modes at high frequency, (ii) the width of the signal line cannot be smaller than  $20 \mu\text{m}$  because of the size of the measurement probes, and (iii) ( $2S+W$ ) need to be smaller than twice the pitch of the probes, the pitch is  $100 \mu\text{m}$  in our station at this frequency range.

To design the CPW, we have used the software Pathwave Advanced Design System (ADS) from Keysight which allow to design and simulate high frequency devices and circuits. First, a tool from ADS called Controlled Impedance Line Designer is used to calculate the dimension of our CPW with our constraints. Afterwards, a simulation of the S-parameters of the CPW is carried out up to 67 GHz. Then, as mentioned above, two structures based on the dimension of the CPW are studied. The first one is the OPEN structure (corresponding to an open circuit) which represents the lower limit of the isolation obtainable for the RF switch OFF state. The second

is the SHORT structure (corresponding to a short circuit) which represents the lower limit of the insertion loss obtainable for the RF switch in the ON state. Both of these structures are then simulated up to 67 GHz and then compared to the fabricated one.

### 2.2.1 CPW Dimension calculation and simulation

To determine the width of the signal line ( $W$ ) and the gap between ground and source ( $S$ ), we first create a file that corresponds to our substrate and specify the conductive metal and the dielectric. This substrate file is used in the Controlled Impedance Line Designer tool to calculate the coplanar waveguides dimension. The substrate chosen is Si/SiO<sub>2</sub> that is a standard substrate for microelectronics, its dielectric constant is 11,68 (Fig. 2a). A width of the signal line  $W$  of 40  $\mu\text{m}$  and a gap  $S$  of 22  $\mu\text{m}$  are determined for a frequency up to 67GHz, giving an impedance of 49.7  $\Omega$ .

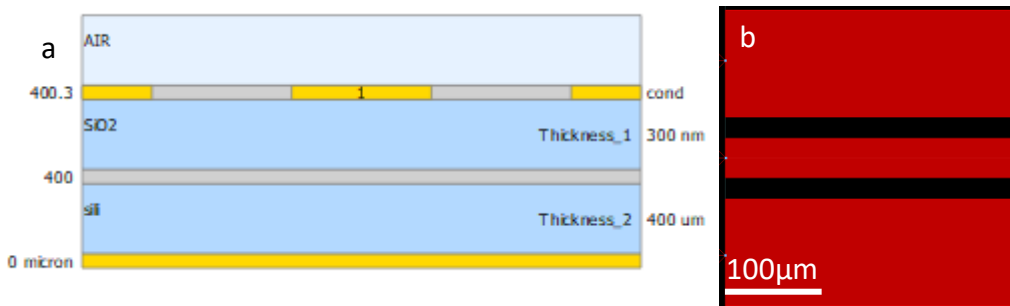


Figure 2 (a) Si/SiO<sub>2</sub> substrate parameters and (b) structure of the CPW simulated with  $W= 40\mu\text{m}$ ,  $S=22\mu\text{m}$  and the length of the coplanar  $L = 300\mu\text{m}$

An S-parameters simulation of the CPW shown in Fig. 3b is realized using a finite element method (FEM) simulation. Fig. 3a shows the reflection parameters  $S_{11}$  and  $S_{22}$  and Fig. 3b shows the transmission parameters  $S_{12}$  and  $S_{21}$ .

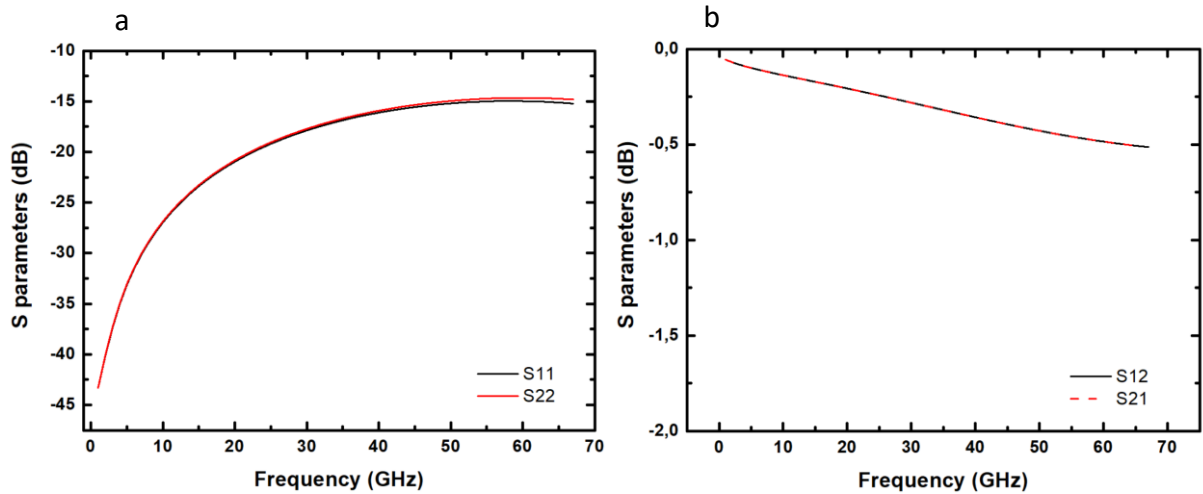


Figure 3 (a) Reflection parameters  $S_{11}$  and  $S_{22}$  (b) transmission parameters  $S_{12}$  and  $S_{21}$  of the CPW. The  $S_{21}$  is -0.5 dB at 67 GHz (89.1% of the power transmitted). For the reflexion it reaches -15 dB at 67 GHz (3.16% of the power is reflected)

The reflexion coefficient at 67 GHz of this CPW is -15 dB meaning that only 3.16% of the power is reflected under matched conditions, which is sufficient for our application.

### 2.3 Structure of 2D switch

Our devices consist of a vertical metal insulator metal (MIM) structure made with a metallic electrode for the bottom electrode (BE) and the top electrode (TE) and with a 2D film sandwiched in between (Fig. 4a). To measure the switch at RF frequencies, the device needs

to be embedded in a CPW. Consequently, the signal line needs to be gradually reduced from 40  $\mu\text{m}$  to the dimension of the 2D switch (Fig. 4b).

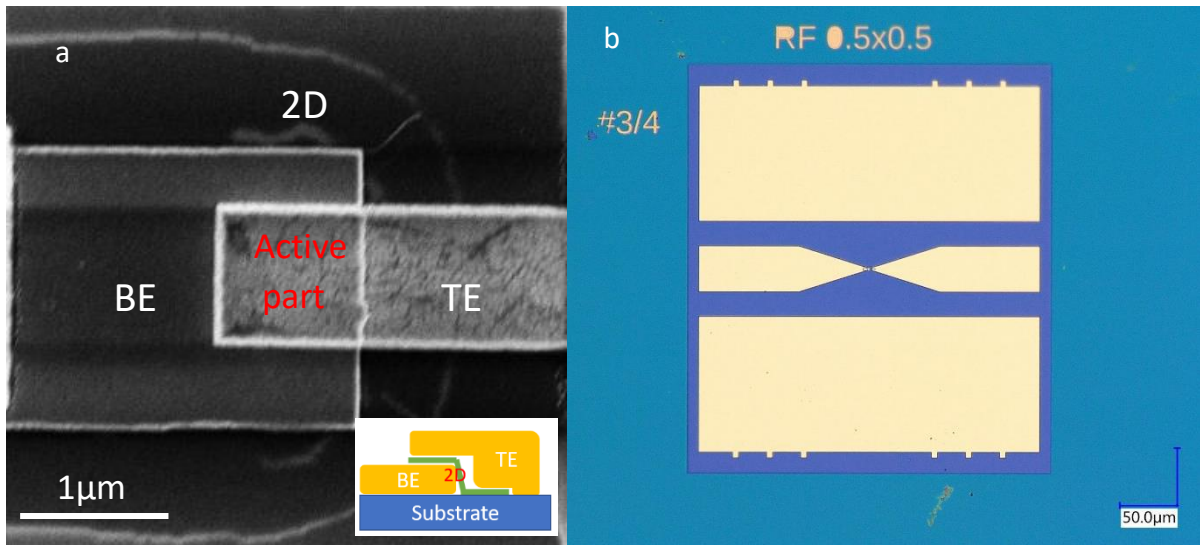


Figure 4 (a) SEM photograph of the switch based (top view). The inset show the cross-section composition of the switch (b) Optical photograph of the switch embedded in the CPW test structure.

### 2.3.1 OPEN/SHORT structures simulation

The layout of the SHORT and OPEN are displayed in Fig. 5a and 6a. They represent an ideal 2D RF switch in ON state and OFF state, respectively. The SHORT layout is based on the CPW structure studied but with a signal line of reduced width (1  $\mu\text{m}$ ) at the place of the future 2D switch (Fig. 5b). The OPEN structure is realized by creating a gap of 3  $\mu\text{m}$  in the middle of the signal line (Fig. 6b). As one represents the limit of the ON state performances of the switch and the other represent the limit for the OFF state, it is mandatory that the difference of the  $S_{21}$  parameters between the ideal ON and the ideal OFF state is as large as possible.

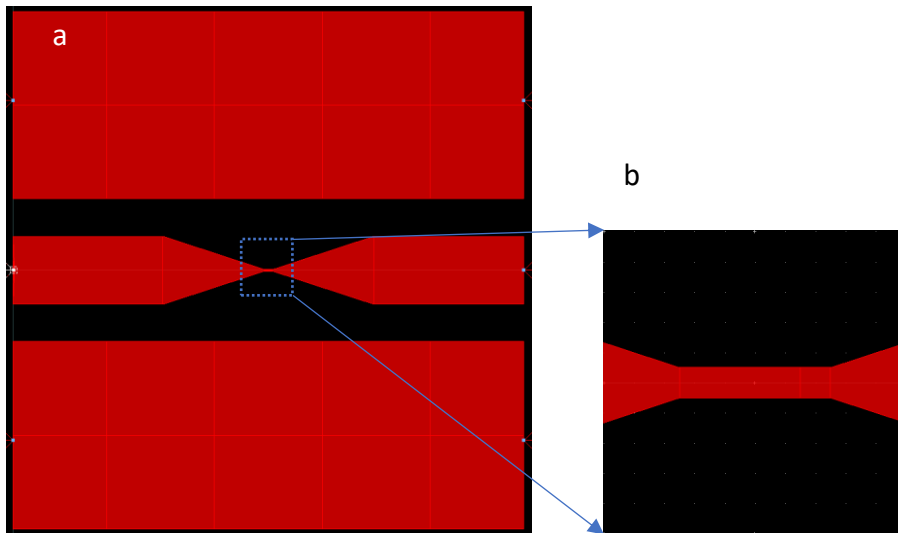


Figure 5 (a) SHORT structure (b) Zoom in of the junction

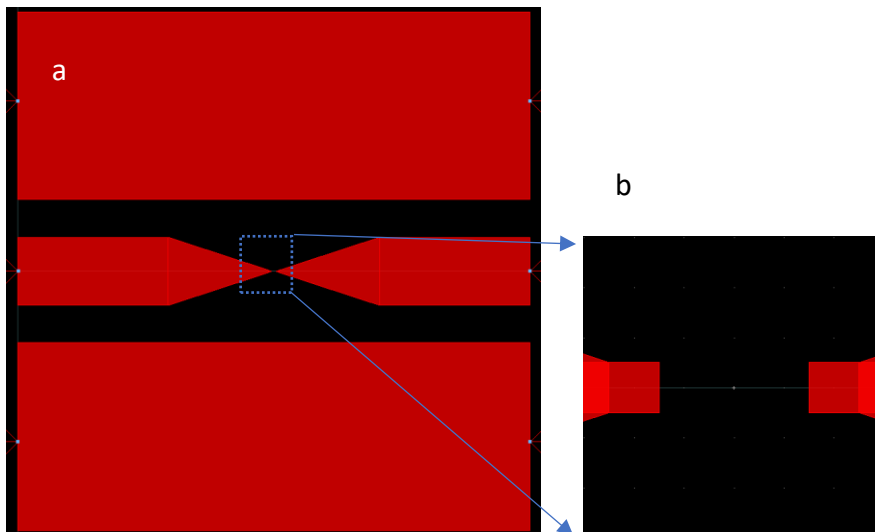


Figure 6 (a) OPEN structure (b) Zoom in of the junction with a 3  $\mu\text{m}$  gap

To validate our design, both structures are simulated up to 67 GHz. The layout of the global device is first created in the layout system of ADS. Once the design is created, we define the ports that simulate the measurements probes and assign them to left (input) and right (output) side of the CPW. Then, the substrate previously defined with its thickness, its dielectric constant and the thickness of the metal electrode is selected. Finally, the finite element method (FEM) and the frequency range for the simulation are chosen in the software. The simulation of S-parameters for both OPEN and SHORT is then obtained.

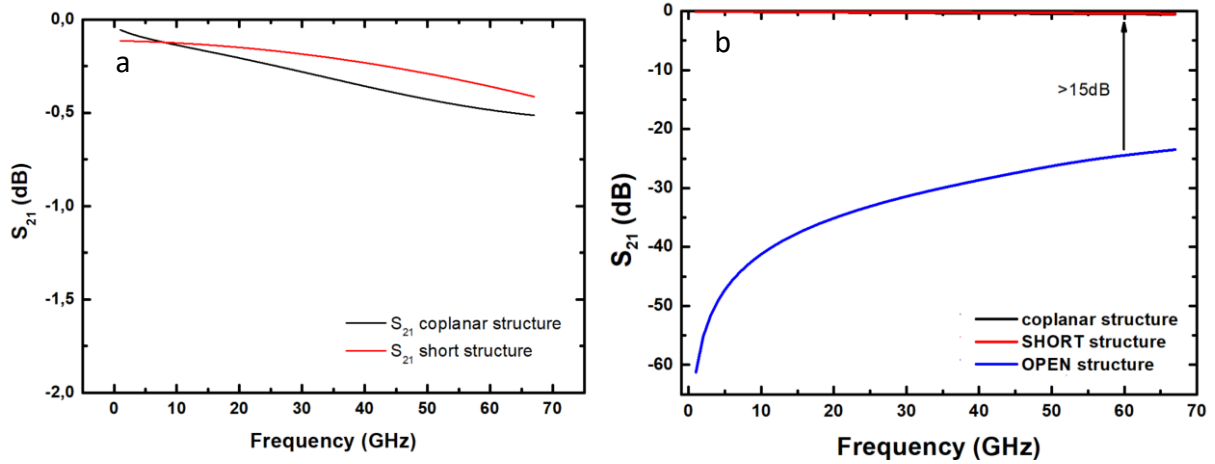


Figure 7 (a) Comparison of  $S_{21}$  parameters between the classical CPW and the modified SHORT structure. The classical CPW reaches a value of -0.5 dB at 67 GHz and the SHORT structure is around -0.4 dB at 67 GHz. (b)  $S_{21}$  parameters for SHORT/OPEN and the classical CPW, a difference >15dB is observed between the  $S_{21}$  parameter of the OPEN and the SHORT best structure. The insertion loss of the SHORT is -0.4dB at 67 GHz and the isolation of the OPEN is -22 dB at 67 GHz

Fig. 7 shows a comparison of the  $S_{21}$  parameters between the first coplanar waves guide and the SHORT structure. We can observe that the reduction of the signal line in the SHORT does not affect significantly the transmission, compared to the CPW. For a CPW with a gap of 3  $\mu\text{m}$  as OPEN structure, the transmission is less than -20 dB at 67 GHz. Therefore, a difference of more than 15 dB between the SHORT and the OPEN is achieved up to 67 GHz.

### 2.3.2 Comparison between measurement and simulation for SHORT/OPEN structures

The OPEN and SHORT test structures are then fabricated on a silicon/silicon oxide ( $\text{Si}/\text{SiO}_2$ ) substrate. The measurements of the fabricated OPEN/SHORT structures are compared to the results obtained in simulations. Fig. 8 shows  $S_{21}$  as a function of frequency up to 67 GHz for the  $\text{Si}/\text{SiO}_2$  substrate. We observe that for both the OPEN and the SHORT structure the simulation results and measurements data are close to each other. The difference between  $S_{21}$  of the SHORT and the OPEN is around 23 dB at 67 GHz.

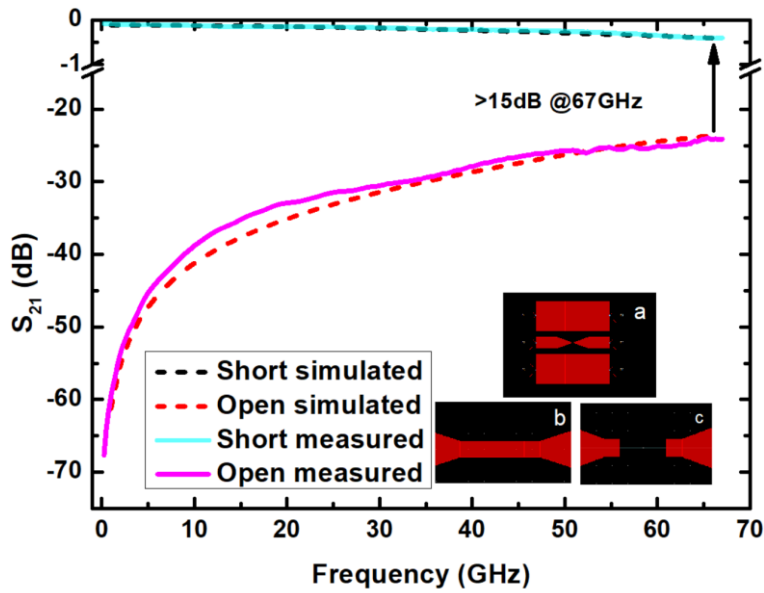


Figure 8  $S_{21}$  parameters comparison between simulated inset (a) general structure of (b) SHORT and (c) OPEN. The SHORT structure reaches a value of -0.4 dB for both the measurement and the simulation at 67 GHz. The OPEN structure reaches a value of -25 dB for both the measurement and simulation

The difference between  $S_{21}$  in the ON state and in the OFF state should be as high as possible. For practical data communication, a difference of at least 10 dB between the ON and the OFF state allows to differentiate each state. For the demonstration of the practical use of our device, we aim to have a difference in  $S_{21}$  of at least 15 dB between ON and OFF state to allow a better distinction between both states.

### 2.3.3 Optimization up to 480 GHz

After the design for devices on silicon substrate working up to 67 GHz, another design was realized for frequency up to 480 GHz. The structure of the CPW used as a base is changed with the width,  $W$ , reduced to the minimum dimension of 20  $\mu\text{m}$  and a ground-signal distance,  $S$ , of 5  $\mu\text{m}$ . A diamond substrate is also preferred to Si/SiO<sub>2</sub> due to its lower dielectric constant ( $\epsilon_r = 5.7$ ) and its better thermal dissipation. (Fig. 9a)

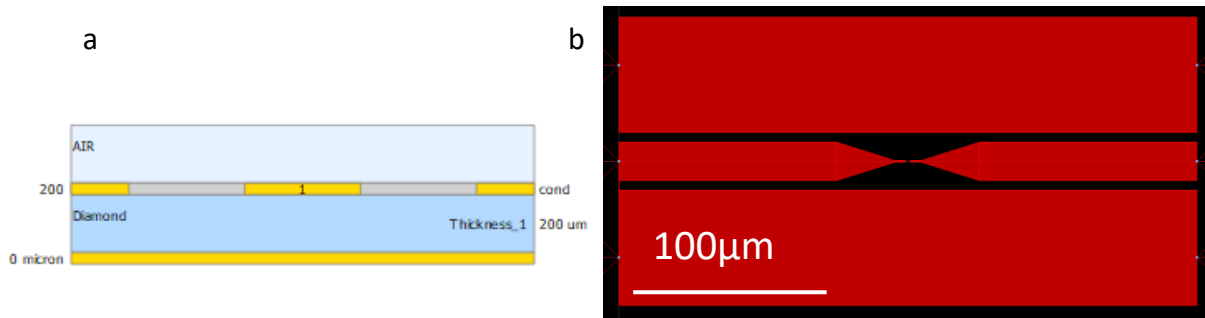


Figure 9 (a) Cross section of the diamond substrate parameters and (b) design of the optimised high frequency OPEN structure

Fig.9b shows the new structure used for both OPEN/SHORT structure. The simulated S-parameters of both of these structures are presented in Fig.10. The aim to get a gap between SHORT and OPEN around 15 dB is fulfilled over the whole 0.1-480 GHz.

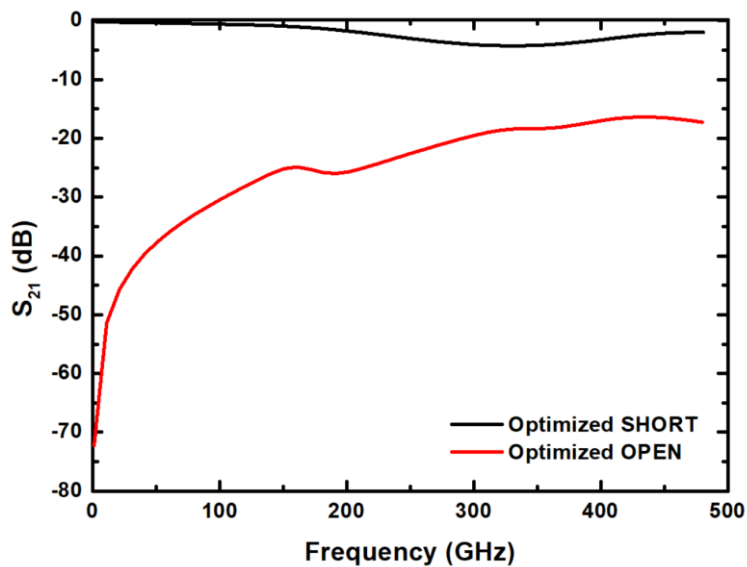


Figure 10 Simulation of  $S_{21}$  for the OPEN and the SHORT structure optimized for operation up to 480 GHz.

Fig.10 shows that at 480 GHz the transmission is reduced to -2 dB for the SHORT and -17 dB for the OPEN. We should stress that simulations at these frequencies are very tricky and experimental validation through measurements is mandatory (see next chapter).



### 3. Description of DC and RF measurement procedure

This section describes the procedures used to extract DC and RF properties of 2D switches. More precisely, we describe the RF and DC measurement setups and the de-embedding procedure.

The RF switches discussed in the next two chapters are directly embedded in the CPW transmission line as mentioned previously. Also, as their structures are very simple, *i.e.*, we can switch them OFF and ON by applying a DC bias pulse or step directly on the RF signal line. Therefore, an RF probe station with a DC source (SMU E5270) connected to the VNA (Agilent E8661A) is used for DC characterization and RF characterization. The DC sources is used for DC characterization prior to any RF measurements and to switch the device ON and OFF.

Considering the progress achieved during my thesis, several RF setups similar to the one mentioned above were used for RF characterization:

- A VNA (Agilent E8661A) from 0.25-67 GHz
- A VNA and a millimetre-wave converter ZC110 for the frequency range 0.25-110GHz
- A VNA and a millimetre-wave converter ZC220 for the frequency range 140-220GHz
- A VNA and a millimetre-wave converter ZC330 for the frequency range 220-325GHz
- A VNA and a millimetre-wave converter ZC500 for the frequency range 325-480GHz

The results of the measurements are detailed in chapter 3.

#### 3.1 RF measurement procedure

Prior to the RF measurements, a Line-Reflect-Reflect-Match calibration (LRRM) is performed to remove the impact of cables and connectors of the measurements. A de-embedding procedure is then applied to extract the RF properties of the switches from the transmission line access.

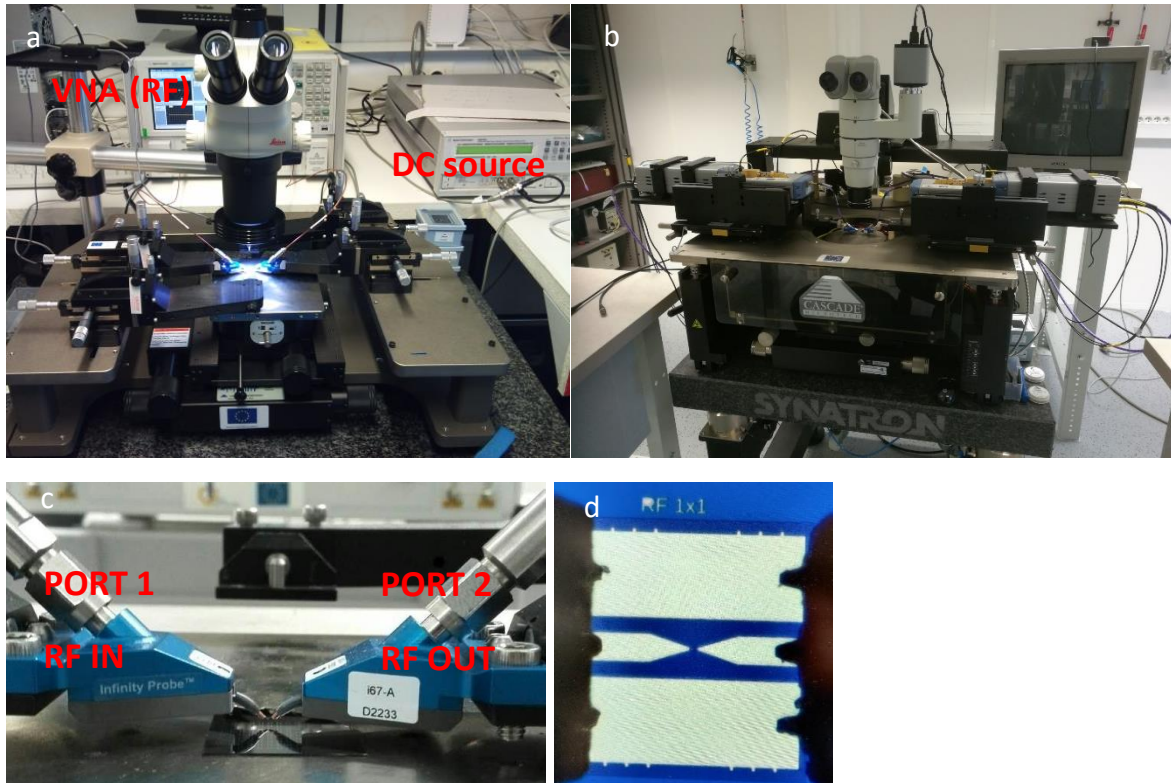


Figure 11 (a) Typical setup for S-parameters/IV measurements for the frequency range 0.25-67 GHz (b) setup for S-parameters/IV measurements for the frequency range 0.25-110 GHz (c) photo of the CPW probe tips with 100  $\mu\text{m}$  pitch (d) photo of a device under test (DUT) with 100  $\mu\text{m}$  pitch CPW pads

### 3.2 De-embedding procedure

The de-embedding removes the parasitic contribution of the CPW structure from the measured S-parameters to extract the intrinsic FOM of the device. A de-embedding is necessary as the contribution from the coplanar wave guide can be high, especially at high frequencies [1] [2]. The schematic in Fig. 12 depicts the equivalent lumped element model of our 2D-based RF switch for both of its state. It represents the intrinsic parameters the 2D switch: in the ON state the resistance,  $R_{\text{ON}}$ , is in parallel to the capacitance,  $C_{\text{ON}}$ , and in the OFF state the resistance,  $R_{\text{OFF}}$ , is in parallel to the capacitance,  $C_{\text{OFF}}$ .

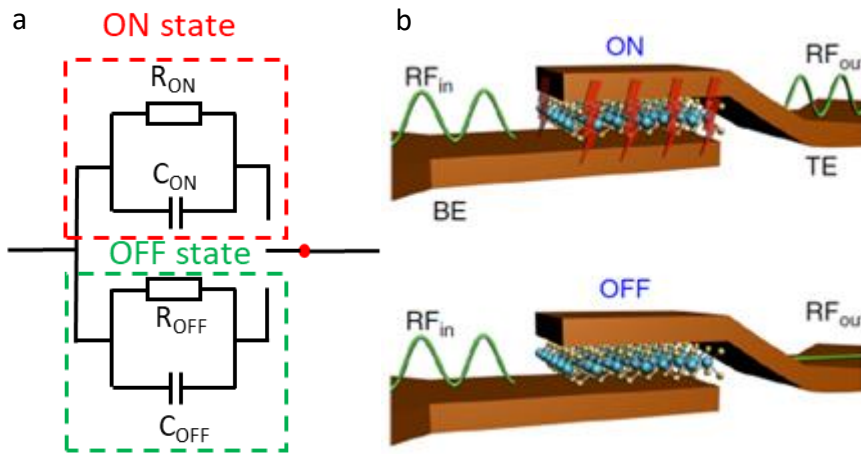


Figure 12 (a) The equivalent lumped element model for our RF switch (b) representation of the 2D switch in both states from [5]

The RF characterization system of the switch and its coplanar structure can be represented as show in Fig. 13.

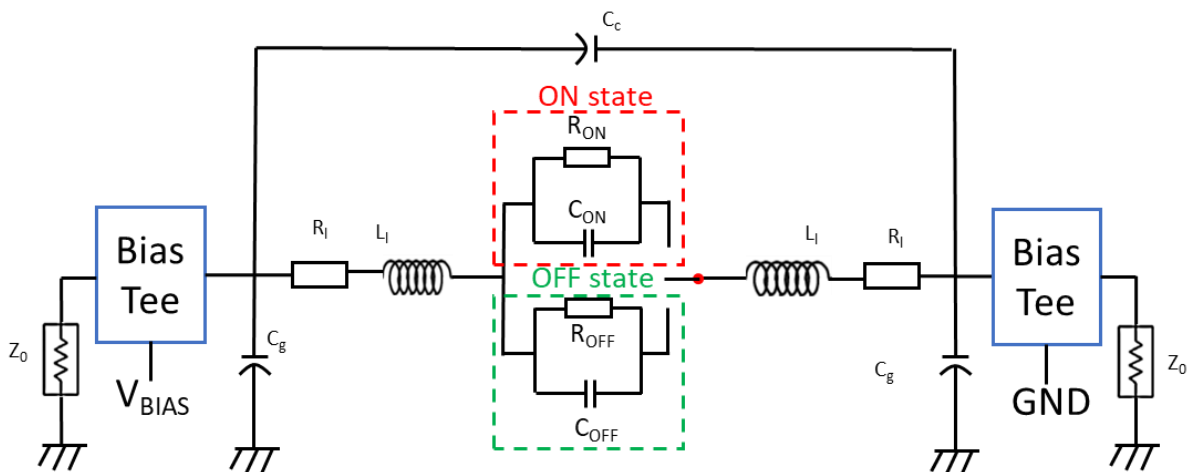


Figure 13 Equivalent lumped element model of the RF switch embedded in a CPW. This model includes the characteristics impedance,  $Z_0$ , the line resistor,  $R_l$ , the line inductor,  $L_l$  the parasitic capacitance coupling to ground,  $C_g$ , the cross-talk capacitance,  $C_c$ ,  $R_{ON}$  and  $C_{ON}$  represent the ON state of the 2D switch and  $R_{OFF}$  and  $C_{OFF}$  represent the OFF state of the 2D switch

The coplanar wave guide is described by the lumped RLC models, where  $R_l$  is the resistance,  $L_l$  the inductance,  $C_g$  the coupled capacitance and  $C_c$  the cross-talk capacitance. These parameters need to be determined to de-embedded the characteristics of the device. To realize this, the on-chip SHORT and OPEN structures are measured.

### 3.2.1 Removing of the parasitic elements

The equivalent lumped element circuit for the OPEN and SHORT structure are represented in Fig. 14. They are passive and symmetric. The capacitance between the input and output signal lines which are separated by 3 microns (see layout open Fig. 6) is negligible.

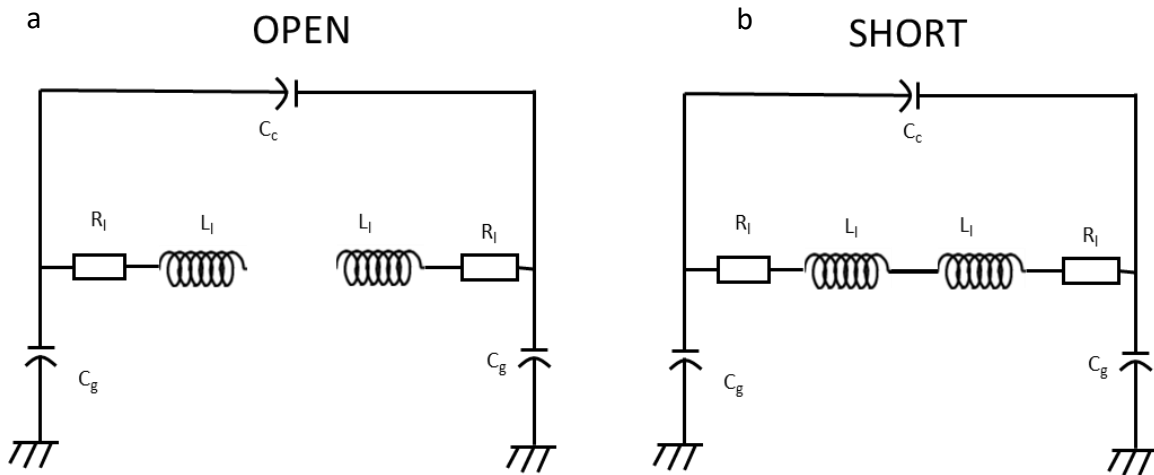


Figure 14 (a) Equivalent lumped element circuit for the OPEN structure (b) equivalent lumped element circuit for the SHORT structure

#### Removing of capacitive parasitic Cg and Cc:

To perform the de-embedding [6], first we transform the measured S-parameters of the device, the SHORT and OPEN structures into Y parameters. The transformation equations are detailed in the annex.

From the Y parameters of the device under test (DUT) and SHORT we remove the parallel capacitive contributions of the coplanar wave guide structure by subtracting the Y parameters of the OPEN structure:

$$Y_{T1} = Y_{dut} - Y_{open}$$

$$Y_{T2} = Y_{short} - Y_{open}$$

#### Removing of line resistance and line inductance:

To remove the series contribution of the resistance of the line  $R_l$  and the inductance of the line,  $L_l$ , from the DUT measurements, we transform the admittance parameters  $Y_{T1}$  and  $Y_{T2}$  into impedance parameters  $Z_{T1}$  and  $Z_{T2}$ . The intrinsic Z parameters are easily obtained by subtraction.

$$Z_{intrinsic} = Z_{T1} - Z_{T2}$$

### 3.2.2 Determination of the intrinsic parameters:

Finally, we transform  $Z_{intrinsic}$  into Y parameters and from them we determine  $R_{ON}$  and  $C_{ON}$  for the ON state of the RF switch and the  $R_{OFF}$  and  $C_{OFF}$  for the OFF state of the RF switch by looking at the real and imaginary parts using the following equations (calculations are in the annex):

$$R = \frac{1}{Re(-Y_{21})}$$

$$C = \frac{Imag(-Y_{21})}{2 * \pi * Frequency}$$

#### Validation of the De-embedding

To validate the de-embedding, we compare the  $R_{ON}$  extracted from S-parameters with the DC value  $R_{DCON}$  measured during the I-V characterization. We observed that the two values are in agreement as they differ by less than 1  $\Omega$  once we subtract  $R_{DCSHORT}$  (DC resistance of the short structure) from  $R_{DCON}$  of the RF switch.

## 4. Conclusion

This chapter introduces two layouts for our switch embedded on a CPW.

The first one is for a silicon substrate. Its CPW is designed with the help of simulations and has a signal width of 40  $\mu\text{m}$  and a gap signal to ground of 22  $\mu\text{m}$ . Then, OPEN and SHORT are designed by modifying the CPW and gradually reducing the signal line to match the small size of our 2D switches. A simulation of the SHORT and OPEN structure is performed up to 67GHz, achieving an insertion loss of 0.44 dB at 67 GHz and 23 dB isolation, respectively. Both of these

layouts are design for de-embedding and will be used for extracting the intrinsic parameters of our 2D switch. The simulation is compared with the measurements on fabricated structures to validate the design.

Furthermore, in order to characterize the 2D RF switches at higher frequency (up to 480 GHz), a second optimized structure for OPEN and SHORT was simulated up to 480 GHz. It possesses a smaller gap between signal and ground of 5  $\mu\text{m}$  and a smaller signal line width of 20  $\mu\text{m}$ . The simulated substrate was changed from Si/SiO<sub>2</sub> to diamond for its higher thermal conductivity, insulation and lower dielectric constant ( $\epsilon_r = 5.7$ ). The simulation of the SHORT and OPEN structure performed at 480 GHz show an insertion loss of 1.9 dB and an isolation of 20 dB.

In the second part of this chapter, the setups used for the DC and RF measurements are presented. As the frequency range of measurement was quite important, five different setups with the respective frequency ranges of 0.25-67 GHz, 0.25-110 GHz, 140-225 GHz, 225- 325 GHz and 325-480 GHz were required. The measurement results will be discussed in the chapter 3. Finally, the de-embedding procedure used to extract the intrinsic FOM and the switch equivalent circuit parameters  $C_{\text{OFF}}$  and  $R_{\text{ON}}$  is described. The results of the de-embedding are discussed in chapter 3.

## 5. References

- [1] D. M. Pozar, *Microwave Engineering, 4th Edition*. Wiley, 2011.
- [2] « Introduction », in *Coplanar Waveguide Circuits, Components, and Systems*, John Wiley & Sons, Ltd, 2001, p. 1-10. doi: <https://doi.org/10.1002/0471224758.ch1>.
- [3] M. Kim *et al.*, « Analogue switches made from boron nitride monolayers for application in 5G and terahertz communication systems », *Nat. Electron.*, vol. 3, n° 8, p. 479-485, agu. 2020, doi: 10.1038/s41928-020-0416-x.
- [4] M. Kim *et al.*, « Non-volatile RF and mm-wave Switches Based on Monolayer hBN », in *2019 IEEE International Electron Devices Meeting (IEDM)*, dec. 2019, p. 9.5.1-9.5.4. doi: 10.1109/IEDM19573.2019.8993470.
- [5] M. Kim *et al.*, « Zero-static power radio-frequency switches based on MoS<sub>2</sub> atomrystals », *Nat. Commun.*, vol. 9, n° 1, p. 2524, june 2018, doi: 10.1038/s41467-018-04934-x.

- [6] G. Dambrine, A. Cappy, F. Heliodore, et E. Playez, « A new method for determining the FET small-signal equivalent circuit », *IEEE Trans. Microw. Theory Tech.*, vol. 36, n° 7, p. 1151-1159, 1988, doi: 10.1109/22.3650.

# CHAPTER III Fabrication and RF characterization of 2D based switches



# Table of Contents

CHAPTER III Fabrication and RF characterization of 2D based switches .....	55
1. Introduction.....	58
2. Fabrication process .....	59
2.1 Overview of microfabrication .....	59
2.2 Description of the layout .....	60
2.3 Fabrication of alignment marks .....	62
2.4 Fabrication of the bottom electrode (BE).....	63
2.5 2D material transfer and patterning.....	65
2.6 Fabrication of the top electrode (TE).....	68
2.7 CPW pads deposition .....	70
3. I-V characterisation and S-parameters study.....	71
3.1 Switching phenomenon description .....	71
3.2 Measurement protocol.....	73
3.3 I-V characteristics measurement and S-parameters of switches with 6 monolayers of MoS <sub>2</sub> (SS03).....	76
3.3.1 Switch structure with an active area of 1x1 $\mu\text{m}^2$ .....	76
3.3.2 Switch structure with an active area of 0,5x0,5 $\mu\text{m}^2$ .....	77
3.3.3 Conclusion of IV characteristics and S-parameters measurement for SS03.....	80
3.4 I-V characteristics and S-parameters measurement of Ni/MoS <sub>2</sub> /Pt interface ..	80
3.4.1 Switch structures with an active area of 1x1 $\mu\text{m}^2$ .....	81
3.4.2 Switch structures with an active area of 0,5x0,5 $\mu\text{m}^2$ .....	82
3.4.3 Conclusion of IV characteristics and S-parameters measurement for SS04.....	84
3.5 SS07 I-V characteristic and S-parameters measurement.....	84
3.5.1 Switch structures with an active area of 1x1 $\mu\text{m}^2$ .....	85

3.5.2	Switch structures with an active area of $0,5 \times 0,5 \mu\text{m}^2$ .....	86
3.5.3	Conclusion of IV characteristics and S-parameters measurement for SS07.....	88
4	De embedding of devices and FOM parameters extraction of 3MLs and 6 MLs of MoS <sub>2</sub> 88	
5.	Conclusion .....	91
6.	References.....	92

## 1. Introduction

The first part of this chapter presents the fabrication processes used at IEMN for RF 2D switches fabricated with MoS<sub>2</sub>. The chapter will describe the fabrication step by step starting with the substrate choice. Three sample batches are studied (SS03, SS04 and SS07): two (SS03 and SS04) have 6 monolayers (MLs) of MoS<sub>2</sub> while batch SS07 has 3MLs of MoS<sub>2</sub>. For each batch, different combinations of metal will be used for bottom and top electrode. The metals for the bottom electrode are either Au, Ni, Ag or Pt. For the Top electrode, the metal studied are CrAu, Ni and Pt. Each combination of metals is now defined in function of the metal in contact with the 2D and is called interface. An interface is labelled starting with the metal of the bottom electrode in contact with the 2D material, the 2D layers and the metal in contact with the 2D from the top electrode. For example, one of the interfaces fabricated is Ni/MoS<sub>2</sub>/Ni meaning that the MoS<sub>2</sub> is here sandwiched between two electrodes of Ni directly in contact with the 2D material.

In the second part, a study of the electrical properties of the switches is presented. The I-V characteristics of the devices are analyzed to verify the switching nature of the device. Then the S-parameters are measured to validate and characterize the RF performances of the RF switch in both the ON and OFF states. The study was carried out on devices with an active part (2D metal stack) of two sizes: 1x1 μm<sup>2</sup> and 0.5x0.5 μm<sup>2</sup>. Devices with a 0.25x0.25 μm<sup>2</sup> active part were also fabricated but their I-V characteristics and S-parameters will not be discussed. The interfaces that are presented in this chapter are Au/MoS<sub>2</sub>/CrAu with 6MLs of MoS<sub>2</sub> and Ni/MoS<sub>2</sub>/Pt with 6 MLs of MoS<sub>2</sub> and 3 MLs of MoS<sub>2</sub>. Two other combinations are presented in the annex: Ni/MoS<sub>2</sub>/Ni and Au/MoS<sub>2</sub>/Pt both with 6MLs of MoS<sub>2</sub>. Devices with Pt as bottom electrode were also realized but the results are not presented in this thesis as their analysis is still on-going. The interfaces with Ag as bottom electrode, due to fabrication issues, were not characterized and will not be shown as well in this manuscript. Finally, the de-embedding technique presented in the previous chapter is used to extract the FOMs of the switches and compare the 3MLs MoS<sub>2</sub> and the 6MLs MoS<sub>2</sub> with the interface Ni/MoS<sub>2</sub>/Pt.

## 2. Fabrication process

### 2.1 Overview of microfabrication

This section describes the fabrication process for the first batches of samples, labelled SS03 and SS04, respectively. The detailed design of each component of the layout is given in the annex. The chosen substrate is a two-inch silicon substrate with a thickness of 400  $\mu\text{m}$  and 300 nm of dry thermal  $\text{SiO}_2$  on top.

The entire manufacturing process is based on eBeam lithography. This choice was motivated by the small size of the active area of the switch which requires alignments with accuracy below 100 nm and feature sizes of 250 nm. Moreover, from our experience, eBeam resist is generally easier to remove from 2D materials than optical resist.

The manufacturing of the components is carried out in 5 main steps which will be detailed in the next section:

- (i) The fabrication of the alignment marks based on etching technique.
- (ii) The fabrication of bottom electrodes based on lift-off process. In this work, 4 different metals (Au, Ni, Pt, Ag) are evaporated to explore the potential impact of the metal on the RF switches (in yellow in Fig. 1).
- (iii) The transfer of the 2D material ( $\text{MoS}_2$ ) onto the bottom electrode. This is made at CEA Leti by a scientific partner, followed by the etching at IEMN (in red in Fig. 1).
- (iv) The fabrication of the top electrode, also based on lift-off process (in green in Fig. 1). Two metals were explored for the first substrate: CrAu and Ni.
- (v) Finally, the fabrication of the coplanar waveguide is performed which required thick metallisation (orange in Fig. 1).

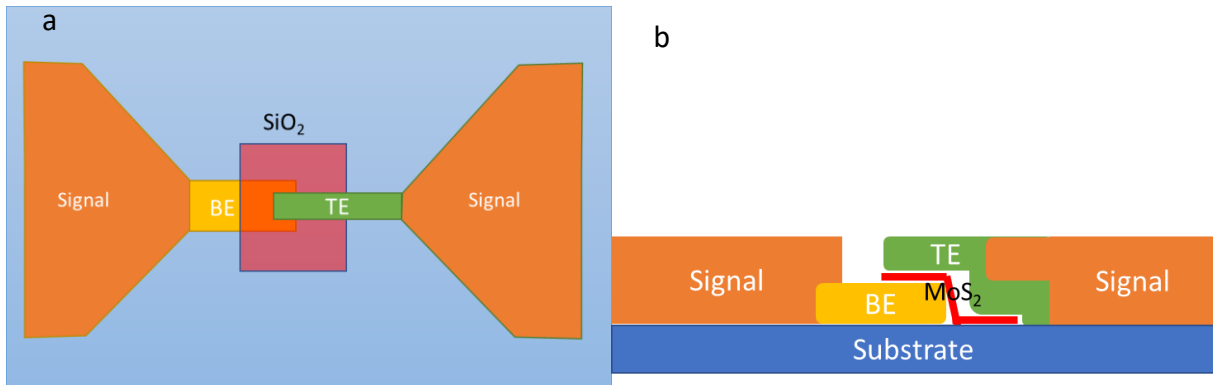


Figure 1 (a) Top view schematic (b) cross section of the device. Each colour corresponds to one fabrication step.

## 2.2 Description of the layout

The layout represents the design of the component that will be fabricated on the substrate. For the elaboration of the layout for the devices, some constraints were taken into account. The first one is that the MoS<sub>2</sub> layer that will be transferred has a maximum dimension of 3x3 cm<sup>2</sup>, the second one is that we want to test different interfaces bottom electrode/MoS<sub>2</sub>/top electrode with the same 2D film. The first constrain is given by the growth process, the second one allows us to compare the impact of the metal interfaces directly. Therefore, we designed the layout by dividing a 2-inches substrate in nine-unit cells with 0.9x0.9 cm<sup>2</sup> area separated by 2 mm pitch in x and y directions. By choosing a unit cell of reasonable size and separated by a little space, one single lithography step can be used to deposit multiple different metals for the bottom or top electrode by mechanically hiding the other unit cells during the evaporation. This size of 0.9x0.9 cm<sup>2</sup> is big enough to regroup a sufficient number of RF devices and de-embedding structures and to manipulate efficiently the substrate for the evaporation step described later in this chapter.

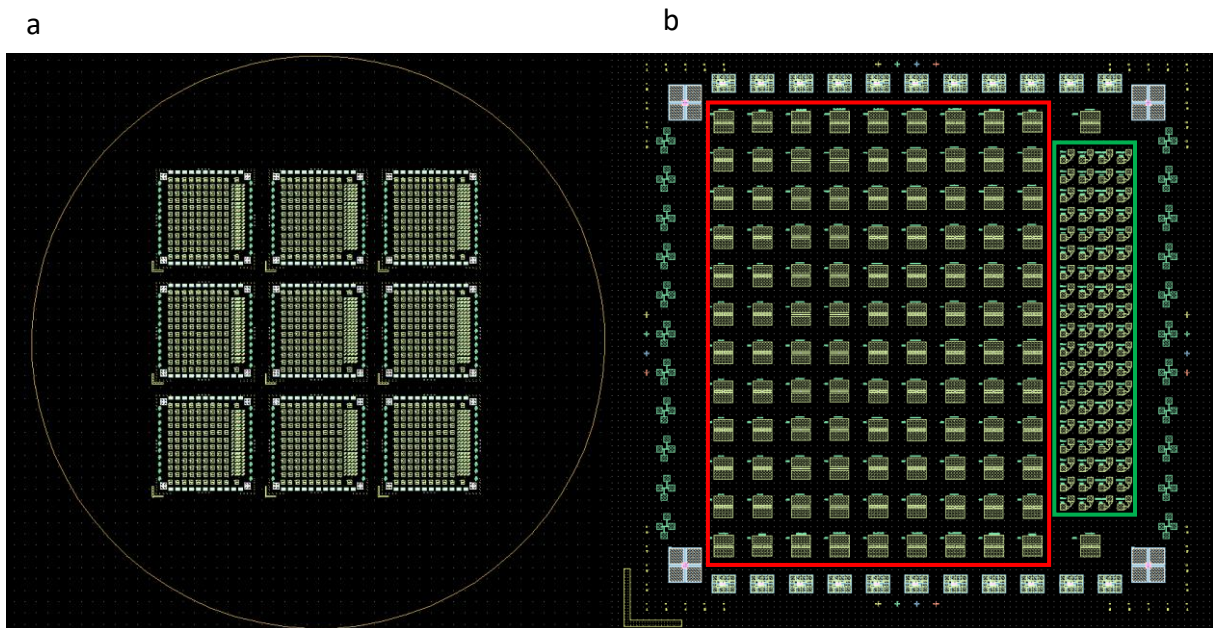


Figure 2 (a) Layout of 2-inch substrate and (b) Layout of a unit cell of  $0.9 \times 0.9 \text{ cm}^2$

Fig. 2 represents the layout of the unit cell that was used for every substrate. Its composition is detailed in table 1 in the annex with a picture of the design for each component. Overall, one unit is composed of the RF part (red square in Fig. 2) and a DC part (green rectangle). Each part is composed of switches with an active part size of  $1 \times 1 \mu\text{m}^2$ ,  $0.5 \times 0.5 \mu\text{m}^2$  and  $0.25 \times 0.25 \mu\text{m}^2$ . Some TLM structure, Hall square structure and resistivity pattern are also present on the layout. Furthermore, OPEN and SHORT structures are fabricated on chip around the RF part for de-embedding purpose. As an example, Fig. 3 shows the design of a  $1 \times 1 \mu\text{m}^2$  RF switch. The CPW access (Fig. 3a) is based on the previous simulated structures. The active part of the switch (Fig. 3b) corresponds to the overlapping of the top and bottom electrodes, with the 2D material sandwiched between them.

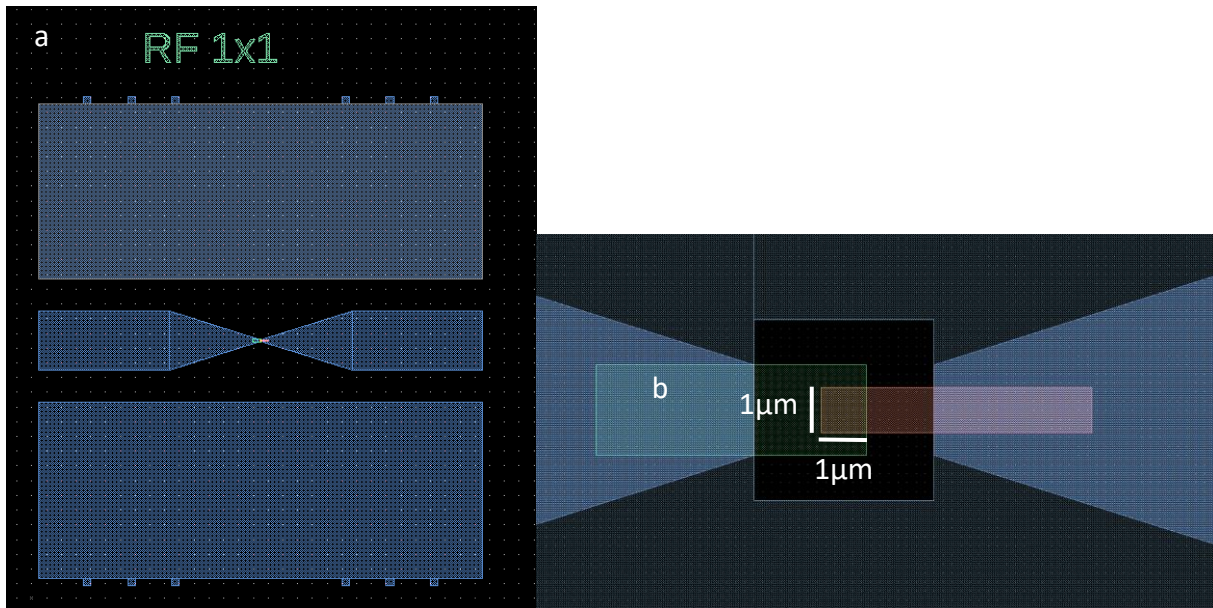


Figure 3 Layout of an RF switch with an  $1 \times 1 \mu\text{m}^2$  active part. (a) the CPW access are based on the simulations discussed in the previous chapter. (b) zoom in the active part the bottom and top electrodes overlap is  $1 \times 1 \mu\text{m}^2$

### 2.3 Fabrication of alignment marks

The alignment marks are used to align patterns defined lithographically in different fabrication step, *e.g.*, bottom electrode, top electrode, etching mask of the 2D material and PAD structure. The alignment marks are etched squares on the silicon substrate of  $20 \times 20 \mu\text{m}^2$  with a depth of  $0.8 \mu\text{m}$ . They are made by etching the substrate with reactive ion etching. The fabrication steps for this part are resumed in table 2 in the annex. First, the substrate is cleaned with acetone and isopropanol, then the substrate is dehydrated at  $180^\circ\text{C}$  on a hot plate for 10 minutes, finally, UV210 41% resist is spin coated on top of the substrate. The thickness required for the resist is  $2 \mu\text{m}$ . The following parameters are used to obtain the wanted resist thickness: speed 2500 rpm, 1000 rpm/s acceleration for 15 s with lid OPEN. Then the substrate is soft baked at  $140^\circ\text{C}$  for 1 min 30 s on the hot plate. Electron beam lithography (eBeam) is then performed to define the alignment mark. The writing is performed by an IEMN engineer using an electron beam pattern generator EBPG 5000plus with a resolution of 25 nm, a surface charge density of  $35 \mu\text{C}/\text{cm}^2$  and a current of 25 nA for a voltage of 10 keV are used. Then, the resist is baked at  $140^\circ\text{C}$  on the hot plate for a post exposition bake and developed with AZ326 MIF developer for 32 s, the development is stopped by



immersing sample into the water for 1 min and drying it with Nitrogen (N<sub>2</sub>) spray gun. Then three etching steps are performed by RIE to etch first SiO<sub>2</sub> with a CF<sub>4</sub> etching then a second one is performed with SF<sub>6</sub> to etch Si and increase the etching rate. The last one is a O<sub>2</sub> etching to remove a part of the polymerized resist made by the previous recipe. This step is required before chemical etching of remaining resist to obtain a clean substrate. The recipes are the following:

**Etching of 300nm of SiO<sub>2</sub>: CF<sub>4</sub> 40 sccm, 50 mTorr, 180 W, 15 min**

After this etching, 300 nm of SiO<sub>2</sub> and 100 nm of Si are etched for a total of 400 nm. The sample was then taken out of the machine for a measurement of the thickness by profilometry. Then another recipe is used to increase the etching rate of silicon substrate.

**Etching of Si: SF<sub>6</sub>, 10 sccm, 20 mTorr, 75 W, 30 s.**

400 nm of Si is etched with this recipe allowing to achieve the 800 nm depth needed for the alignment mark.

The last dry etching consists of an O<sub>2</sub> etching with the following parameters is done to remove a thin polymerized resist on the top of remaining resist, to improve the cleanliness of the substrate after the alignment mark process.

**O<sub>2</sub> etching of resist: O<sub>2</sub>, 20 sccm, 50 mTorr, 50 W, 5 min.**

Finally, the resist left after etching is removed from the substrate by immersing it for at least 2 hours into SVC14 maintained at 70°C. It is then rinsed with acetone for 2 min and IPA for 2 min and dried with N<sub>2</sub> spray gun.

Table 2 in the annex resume all step for the fabrication of the alignment marks.

## 2.4 Fabrication of the bottom electrode (BE)

The bottom electrode (BE) is realized after the alignment marks. It consists of an eBeam writing and a thin-film deposition followed by a lift-off. The size of the BE is 6x2 μm<sup>2</sup> and the thickness of the electrode is the same for all metals tested, 120 nm thick.

First, a baking step at 180°C for 10 min is performed to dehydrate the substrate. Then a double layer of resist is spin coated. The first layer is a 220 nm thick copolymer (EL) 6% resist (1500 rpm speed, 1000 rpm/s acceleration for 15 s with CLOSE lid and 800 rpm speed, 1000 rpm/s acceleration for 8 s with OPEN lid) and the second is an 80 nm thick 4 % PMMA



950 K resist diluted 5/3 (3500 rpm speed, 1000 rpm/s acceleration for 30 s with OPEN lid). The 4% PMMA was diluted in a proportion 5/3 to achieve desirable thickness. The deposition of dual layer of resist (EI 6% and PMMA 4% 950K) facilitates the lift-off process. The soft-baking of resist is performed at 180°C for 10 min after each resist spin-coating. It is then followed by eBeam lithography using a resolution of 10 nm, a surface charge density of 700  $\mu\text{C}/\text{cm}^2$  and a current of 10 nA for a voltage of 10 keV. The development after e-beam writing is done using an MIBK/IPA solution with a dilution ratio 1/2 for 1 min follow by a rinsing of 30 s in IPA. A metal is deposited using an e-beam deposition machine Plassys MEB 550S.

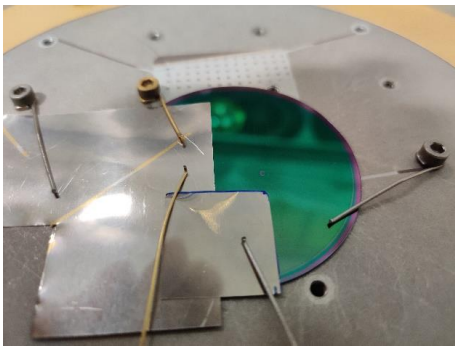


*Figure 4 Mask for the deposition of Au bottom electrodes. The metal will be deposited only on the unprotected part of the wafer. The masks are moved to a different area and a new metal is deposited before lift-off.*

Four different metals are deposited on different parts of the substrate before the lift-off is carried out. This was obtained by masking different areas of the substrate at each deposition (Fig. 4). All depositions use the same process, so we will just detail the first one.

First deposition was Ni/Au, where Ni is used as an adhesion layer, it takes place at a rate of 0.2 nm/s for a thickness of 10 nm for Ni followed by the Au deposition at a rate of 1 nm/s for a thickness of 110 nm. After the first deposition, we moved the mask and deposited the other metal. Then, we repeat this for each different metal. Fig. 5 shows the four different metals on the 2-inch wafer prior to lift-off. Table 3 in the annex resumes all the fabrication steps for this electrode.

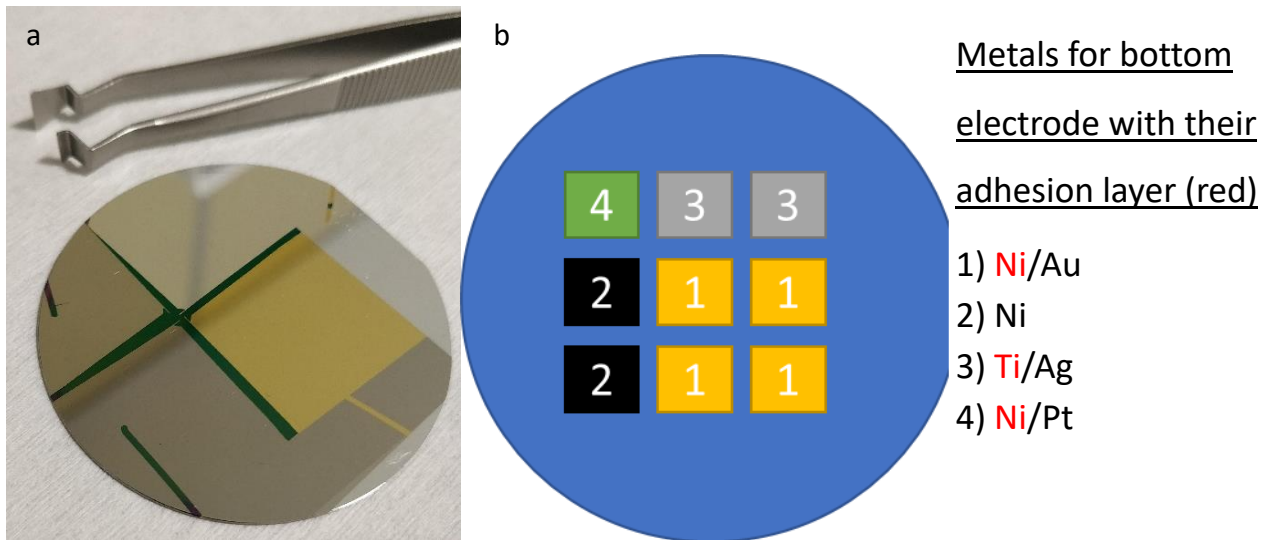


Figure 5 Silicon substrate after four metal depositions for bottom electrode (Ni/Au, Ni, Ti/Ag, Ni/Pt). b Disposition of the metal bottom electrode with respect to the unit cells.

## 2.5 2D material transfer and patterning

The growth and the transfer of the 2D layers are not part of this thesis, as they are carried out by our collaborators at CEA Leti. 6MLs of MoS<sub>2</sub> material were transferred at CEA Leti on two substrates (SS03 and SS04) with bottom electrodes prepatterned at IEMN. The MoS<sub>2</sub> layers were grown on a Si/SiO<sub>2</sub> substrate (from SDEP) and then transferred. The MoS<sub>2</sub> thickness which was measured with an atomic force microscope (AFM) after transfer, is 6 nm, corresponding to 5-6 layers of MoS<sub>2</sub>. (Fig. 6)

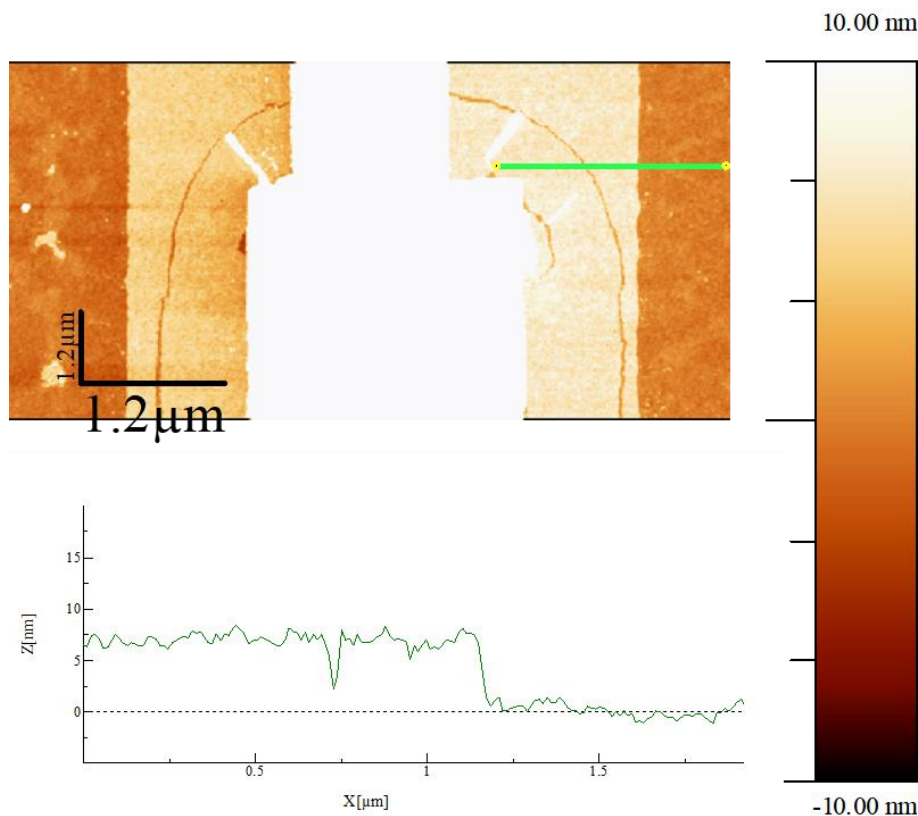


Figure 6 AFM image of  $\text{MoS}_2$  on  $\text{Si}/\text{SiO}_2$  substrate after growth and transfer. Both top and bottom electrode can be distinguished in white. The measurement is done over the green line Inset: the profile of the 2D material shows a thickness of the 2D of 6 nm.

Wet transfer was performed to deposit the  $\text{MoS}_2$  on top of the substrate. The target substrates were first cleaned with acetone and isopropanol (IPA) in an ultrasonic bath. PMMA is spin coated on the  $\text{MoS}_2$  grown on  $\text{Si}/\text{SiO}_2$  and baked at  $150^\circ\text{C}$  for 3 min. PMMA/ $\text{MoS}_2$  layers is then delaminated using deionized water (DI) for the SS03 destined  $\text{MoS}_2$  and NaOH for the destined  $\text{MoS}_2$  of SS04. The PMMA/ $\text{MoS}_2$  layers are then fish up with the targeted substrate SS03 and SS04. A slow drying in ambient air for 20 min on a hot plate at  $80^\circ\text{C}$  is performed, followed by the removal of the PMMA on  $\text{MoS}_2$  in acetone for 10 min.

The  $\text{MoS}_2$  layers with an area around  $7\text{ cm}^2$  were transferred on top of the bottom electrodes. For SS03, four-unit cells were totally covered and two-unit cells were partially covered. For SS04, six units were totally covered. (Fig. 7 –  $\text{MoS}_2$  is illustrated by the red colour)

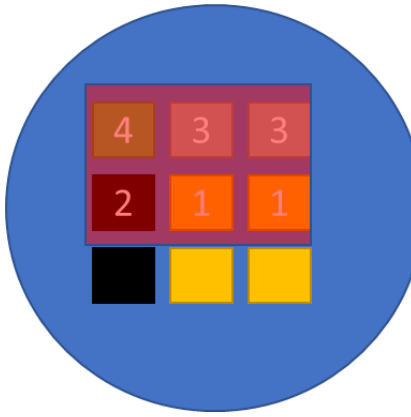


Figure 7 Schematic of the MoS<sub>2</sub> deposition on SS03 substrate.

After transfer, the MoS<sub>2</sub> layer presence and quality was investigated by  $\mu$ Raman measurements. The typical spectra measured on sample SS04 shows two peaks at 382.8 cm<sup>-1</sup> and 407.8 cm<sup>-1</sup>. They are well known MoS<sub>2</sub> peaks and their comparison with spectra taken before transfer suggests that the transfer did not deteriorate the quality of the 2D material. The distance between the peaks (25 cm<sup>-1</sup>) confirms that the thickness of the MoS<sub>2</sub> is around 5-6 layers (Fig. 8). [1]

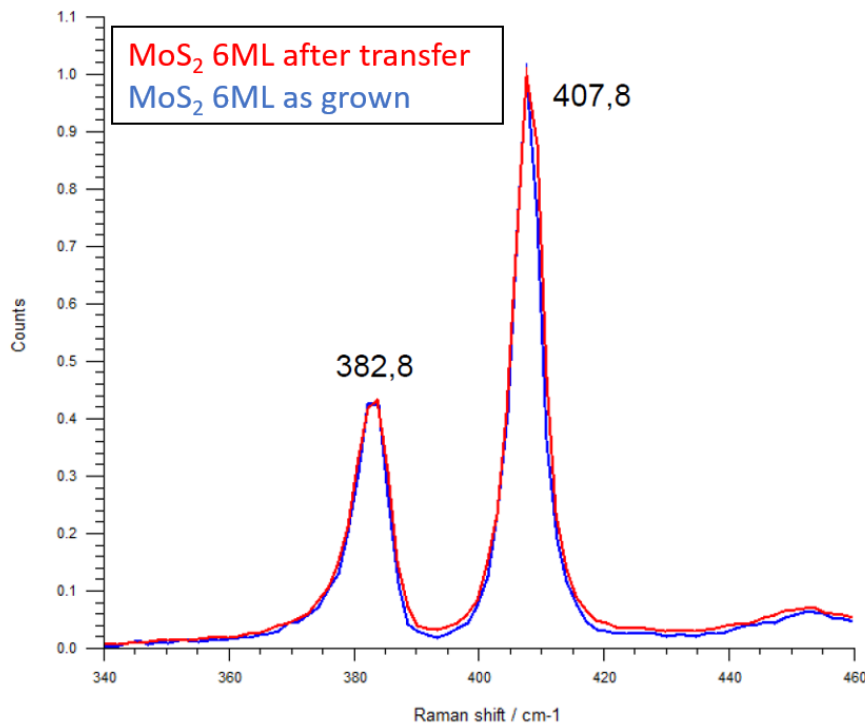


Figure 8 Raman spectroscopy after the transfer of MoS<sub>2</sub> on top of SS04 6 MLs. The distance of 25 cm<sup>-1</sup> between the two peaks corresponds to 6 MLs of MoS<sub>2</sub> and show a good transfer of the 2D materials.

After the transfer of the MoS<sub>2</sub>, a patterning of the MoS<sub>2</sub> is necessary. The main goal of this patterning is to protect a square of 2D material on top of the BE and remove the unprotected 2D layers by dry etching.

Thus, a 350 nm thick layer of 5% PMMA is spin-coated (5% 450 K) (2500 rpm speed, 1000 rpm/s acceleration for 10 s with CLOSE lid and 500 rpm speed, 500 rpm/s acceleration for 8 s with OPEN lid). The etching of MoS<sub>2</sub> material is realized with an RIE system Plasmalab 80+ from Oxford. For the MoS<sub>2</sub>, SF<sub>6</sub> etching is realized with the following parameters:

**SF<sub>6</sub> etching: SF<sub>6</sub> 25 sccm, 80 mTorr, 50 W for 25 s**

The resist is removed by putting the substrate at least 2h in SVC14 at 70°C. It is rinsed with acetone and IPA for 3 min and dried with a nitrogen gun spray.

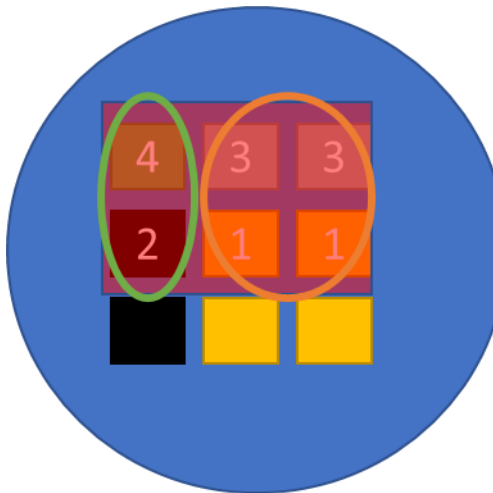
The remaining size of the MoS<sub>2</sub> on top of the BE is 4x4 μm<sup>2</sup> after etching.

Table 4 and 5 in the annex resumes the transfer and patterning of the MoS<sub>2</sub> step by step

## 2.6 Fabrication of the top electrode (TE)

TE is the electrode that will define the size of the active area because of its width and the overlap with the BE. The TE electrode is deposited by using a lift off process, similar to the BE, but the thickness of the metal deposited was increased to 200 nm. This choice increases the resilience of the device (thermal and mechanical properties). Two different metal stacks were deposited (Ni/Au and Cr/Au) depending on the cells using the same masking technique as for the bottom electrode. Fig. 9 shows the disposition of the top electrodes metal as well as the different interfaces fabricated for the first batch (SS03 with 6 MLs). Fig. 10 shows a scanning electron microscope (SEM) image of the switch active area with the bottom electrode and top electrode after fabrication.

Table 6 in annex resume all the step of for the TE fabrication.



TE metals :

Cr/Au : 2/198nm (circled orange)

Ni/Au : 30/170nm (circled green)

Interfaces :

1) Au/MoS<sub>2</sub>/CrAu      3) Ag/MoS<sub>2</sub>/CrAu

2) Ni/MoS<sub>2</sub>/Ni    4) Pt/MoS<sub>2</sub>/Ni

Figure 9 Disposition of top electrode and interface for SS03 substrate

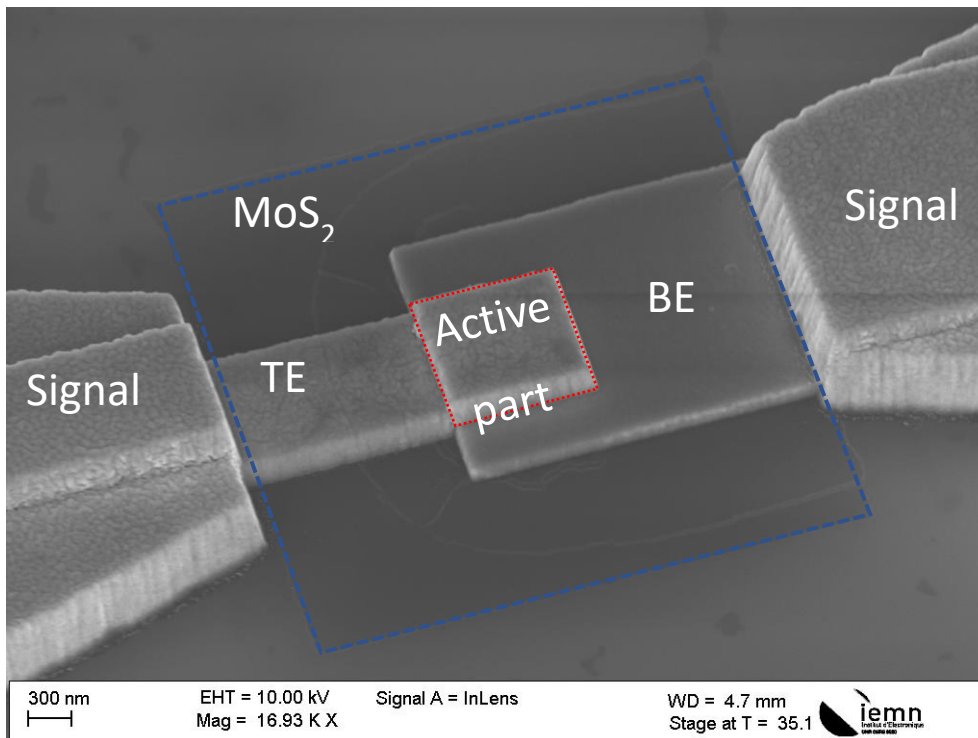


Figure 10 SEM image of an RF switch. The  $1 \times 1 \mu\text{m}^2$  active area is highlighted in the red square. The blue square represents the patterned MoS<sub>2</sub>. The left small electrode is the top electrode (TE) that sandwiches the 2D with the bottom electrode (BE, on the right)

## 2.7 CPW pads deposition

Finally, the last step of the fabrication process is the deposition of the CPW access pads which is composed of the signal line and the two ground planes. The design used for SS03 is the first one presented in the previous chapter with a signal width of  $40\ \mu\text{m}$  and a gap between the signal and the ground of  $22\ \mu\text{m}$ . A lift of process is also used with a deposition of a bilayer resist (EI 13% and PMMA 4% 950 K), followed by the deposition of  $550\ \text{nm}$  of metal ( $50\ \text{nm}$  of Ni and  $500\ \text{nm}$  of Au). Fig. 11 shows the final structure of RF switches embedded in its coplanar waveguides.

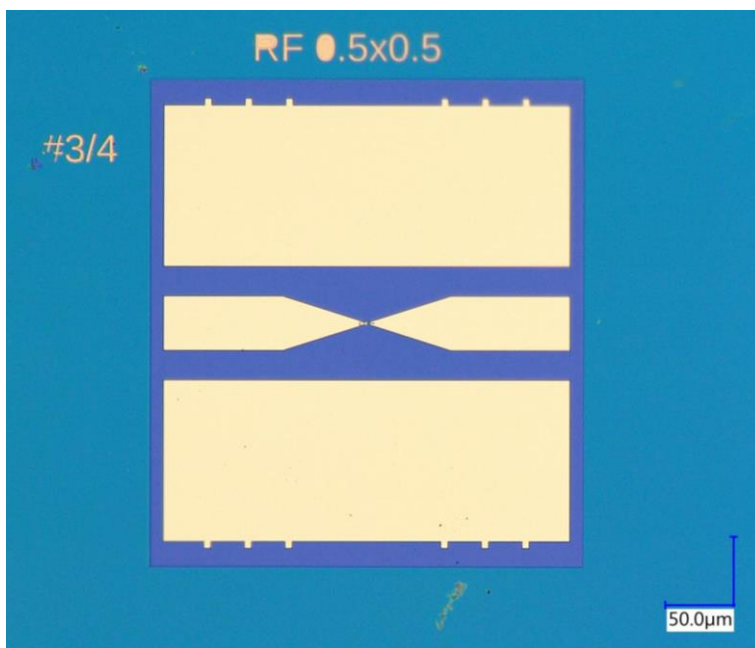


Figure 11 Optical microscopy image of a  $0.5 \times 0.5\ \mu\text{m}^2$  RF switch with coplanar waves guides taken from batch SS03.

All steps for the deposition of CPWs are resumed in table 7 in annex.

Finally, a summary of all interfaces fabricated presents on all the substrates is presented in table 9 in the annex.

Now that the fabrication is finished, DC characteristic (or I-V characteristics) of the devices fabricated can be performed and analyzed alongside with the S-parameters for each interface.

### 3. I-V characterization and S-parameters study

In this section we present first an explanation based on the literature of the phenomenon underlying the 2D switching. Following this explanation of the switching phenomenon, the measurement protocol is explained by giving an example of a typical IV measurement. Then, a typical S-parameter measurement is described. Finally, an observation of the impact of the current limitation on the insertion loss of the devices is shown. Following this protocol measurement explanation, the I-V characteristic measurements of our devices are discussed. We begin with the analysis of the first batch SS03 (6 MLs of MoS<sub>2</sub>) with Au/MoS<sub>2</sub>/CrAu interface for 1x1 μm<sup>2</sup> and 0.5x0.5 μm<sup>2</sup> active part. The interface Ni/MoS<sub>2</sub>/Ni is discussed in the annex. Devices from the batch SS04 with 6 MLs of MoS<sub>2</sub> are measured and analyzed. Two changes are present in SS04. First, the top electrode metal is change to a Pt electrode. Secondly, the device structure is changed to the optimized structure presented in chapter 2 for frequency up to 480 GHz. Furthermore, a new interface Ni/MoS<sub>2</sub>/Pt is studied. The other interface presents on this second batch; Au/MoS<sub>2</sub>Pt is given in the annex. Finally, SS07 possesses only 3 MLs of MoS<sub>2</sub> and is measured with the same interface Ni/MoS<sub>2</sub>/Pt interface and allow us to compared 3 MLs and 6 MLs.

The main goal of this study is to characterize the DC electrical properties of devices from all batches and interfaces. Secondly, the S-parameter measurements are used to determine the switch performances and the equivalent electrical circuits described in previous chapter. From this, the cut-off frequency is calculated. A table is resuming the devices tested at the end of the interface analysis and their main figure of merits, including switching cycles.

#### 3.1 Switching phenomenon description

Recent publications begin to unveil the origin of the switching phenomena in 2D materials [2], [3]. A scanning tunnelling microscope (STM) study provides direct evidence of ion migration at a defect location of a MoS<sub>2</sub> sheet during a SET-RESET cycle [3]. This observation suggests that switching in our devices happens during the SET, *i.e.*, when an electric field is applied and metallic ions migrate through the defects of the 2D materials. The metallic ions form a conductive filament between two electrodes resulting in the switching of the device from its



OFF state to its ON state. During the RESET, Joule heating break the filament and turns the device back from its ON state to the OFF state. The phenomenon is likely the same for both MoS<sub>2</sub> [3] and hBN [2] based switches (see Fig. 13 from Ref [2] for hBN).

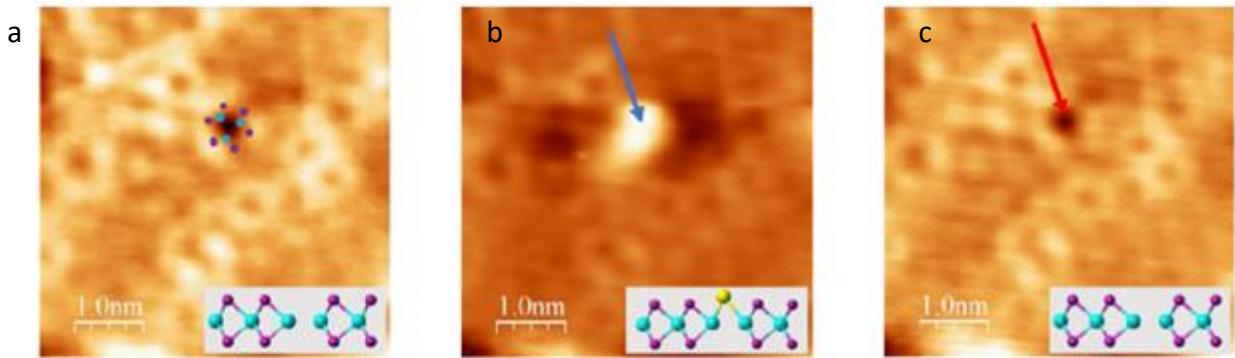


Figure 12 Atomic observation of a SET-RESET sequence with a) presence of a defect in the 2D materials b) after the SET process, the spot is filled by the moving of a conductive ion due to the electric field, that is then remove after the RESET process c) and returns to its original configuration from [3]

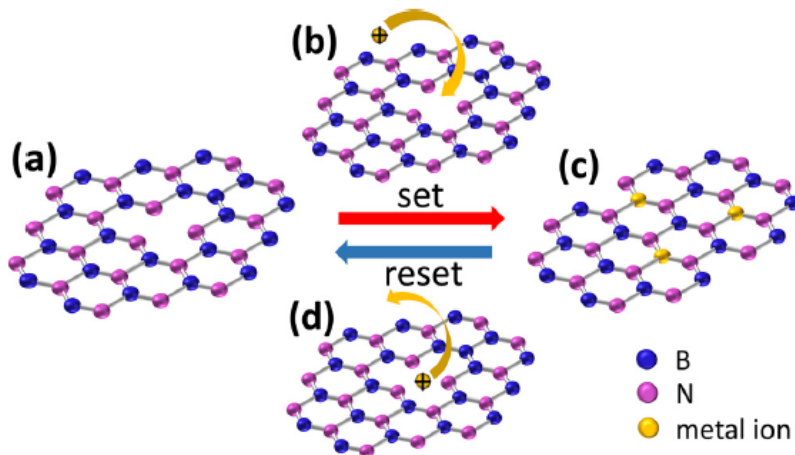


Figure 13 Schematics of resistive switching mechanism in monolayer hBN a) HRS of a monolayer hBN possessing defect or traps b) After the set process, migration of metal ion into the defect is caused by the electric field, c) LRS of monolayer hBN with the metal ion present in the boron vacancies d) reset process, detraping of metal ions with electric field or by Joule heating switching back to HRS from [2]

To summarize, the switching phenomenon is likely caused by the movement of a metallic ions induced by the electrical field generated during a SET. The ions then move into defects of the 2D materials and establish a conductive filament that changes the device from the OFF to the ON state. The reset process then de-trap the metallic ion by joule heating and the ions migrate back to the electrodes.

## 3.2 Measurement protocol

After fabrication, I-V characteristics are measured with the probe station setup described in chapter 2. As reported in literature [4]–[6], after fabrication our switches are in their OFF state as no metallic ion are present at the defect sites of the 2D material. Fig.14 represents one typical I-V measurement of one of our devices. First, a double sweep bias is applied to change its state from a high resistive state (HRS) to a low resistive state (LRS). This first process is called SET process and a limitation of current is applied to avoid breaking the device, in this example the limitation is 30 mA. At the beginning of the first sweep the device is in the OFF state with a low current (1 in Fig. 14). When the switch bias reaches the so-called switching voltage the device current increase abruptly (2 in Fig. 14) up to the current limitation. The second sweep runs from 1.5 V to 0 V. The value of the current remains high during the down-sweep, showing that the device remains in the ON state (3 and 4 in Fig. 14). To switch the device back to its OFF state, a double sweep from 0 V to -1 V and from -1 V to 0 V is applied. This process is called RESET. During the reset, the current limitation is removed or set higher than for the SET. The current remains large (5 in Fig. 14) until the switch reaches the switching voltage of -0.6 V. For this example, the current value reaches 35mA, then its value is abruptly reduced (6 in Fig. 14) and the device switches from ON to OFF. The device remains OFF when the bias is decreased to 0 V (7 in Fig. 14). These two processes, SET and RESET, represent one switching cycle for our device.

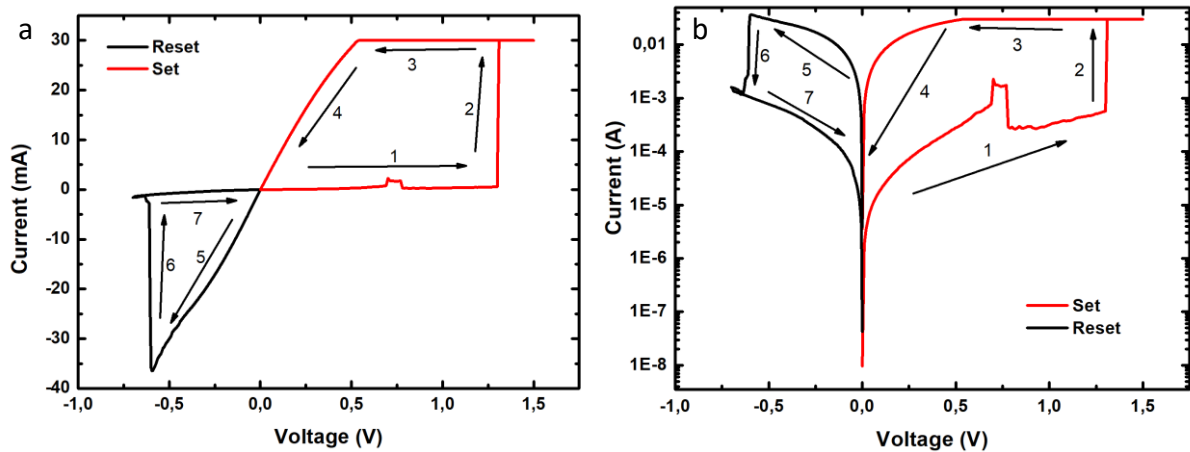


Figure 14 I-V characteristics of a RF switch. The source meter current limit has been set to 30 mA. The trace in red (1,2,3,4) represent the SET process of the switching, the trace in black (5,6,7) represent the RESET process in (a) linear scale and (b) logarithmic scale

As the probe station allows for DC and RF measurements, we can use the same setup to switch the devices and to determine their S-parameters. The S-parameters are measured after each switching cycle. The transmission parameters  $S_{21}$  is the most important to evaluate the performances of the device as a switch as it represents the transmission (ON state) or isolation (OFF) under matched conditions. Fig. 15 shows a typical S-parameter measurement for the same device as the I-V characteristics shown in Fig. 14 ( $0.5 \times 0.5 \mu\text{m}^2$  active part of an Au/MoS<sub>2</sub>/CrAu interface). The x-axis is the frequency in linear scale whereas the y-axis represents the transmission/isolation loss in dB.

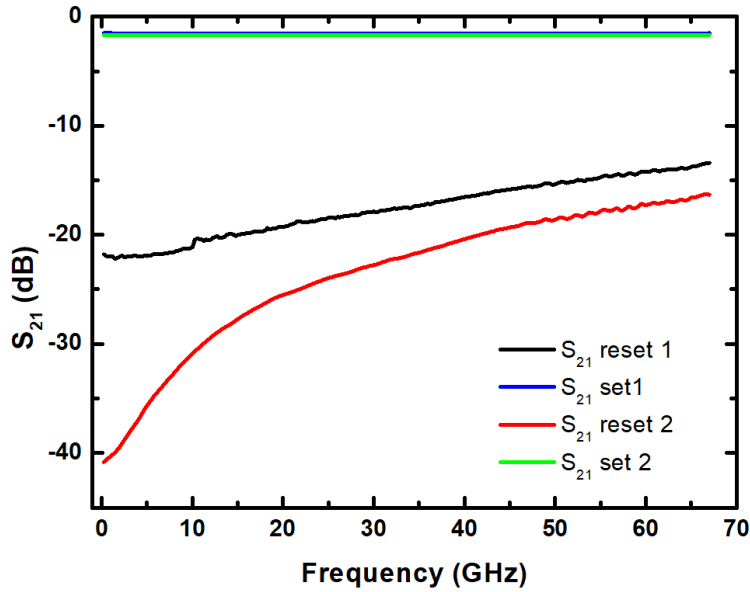


Figure 15 Typical  $S_{21}$  parameters of a  $0.5 \times 0.5 \mu\text{m}^2$  device with multiple cycle with Au/MoS<sub>2</sub>/CrAu interface. For this device we obtain an insertion loss of 1 dB at 67 GHz and an isolation of 16 dB at 67 GHz after the second reset of the device.

The transmission for this device in the ON state at 67 GHz is -1 dB, which means that in the ON state around 80% of the signal power is transmitted through the device. For its equivalent in the OFF state, the second RESET reaches a  $S_{21}$  parameters of -16 dB at 67 GHz. In this case only 2.5% of the signal's power is transmitted through the device in its OFF state. The signal is correctly blocked as wanted. The ON/OFF difference is -15 dB at 67 GHz and exceeds 20 dB at 30 GHz.

We now present the effect of current limitation used during the SET process. We start by increasing the current limitation from 10 mA to 30 mA on the same device and record both DC and S-parameters of each cycle. Fig. 16b shows the evolution of the insertion loss of a switch as a function of the current limitation. The best insertion loss obtain was with a 30 mA current limitation with - 0.9 dB value at 67 GHz. Compared to the SHORT structure that should represent the ON state of an ideal RF switch, a difference of 0.5 dB is present at 67 GHz with a value of -0.4 dB for the SHORT and -0.9 dB for the device with a current limitation of 30mA. Therefore, to obtain the best insertion loss possible, we need to switch the device using a high current limitation. Larger current limitation results in a lower resistance in the ON state (Fig. 16a), which is consistent with the decrease of insertion loss observed at RF. These observations can be explained by the formation of a larger filament or multi-filaments at different locations.

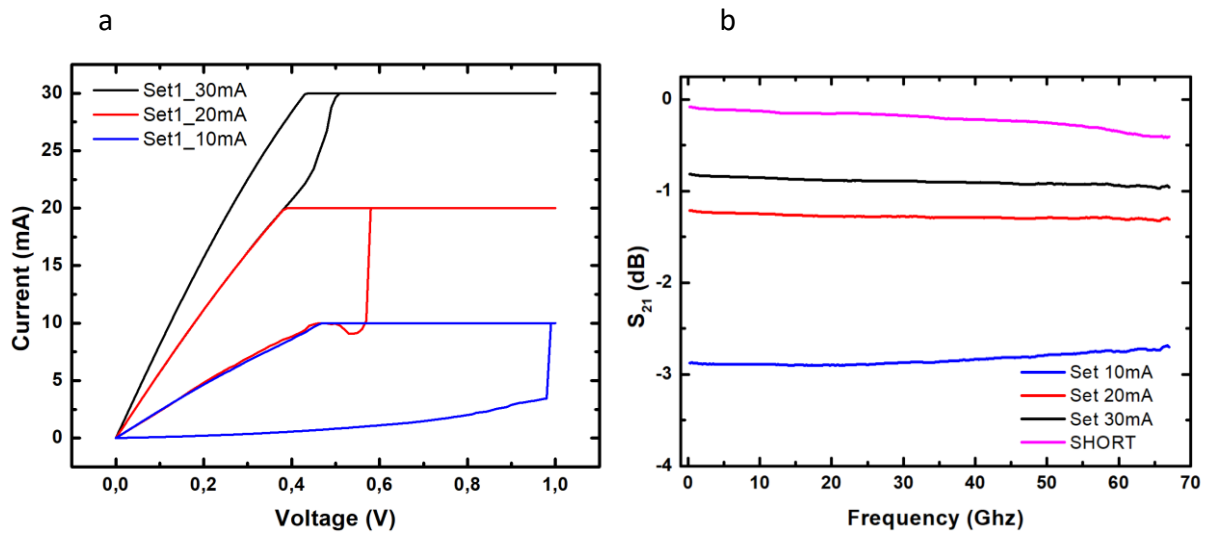


Figure 16 Comparison of (a) I-V characteristics and (b) S-parameters for the ON state with different current limitations for a  $1 \times 1 \mu\text{m}^2$  active part size with Au/MoS<sub>2</sub>/CrAu interfaces and comparison with the SHORT structure fabricated on chip and measured. The insertion loss goes from -3 dB to -1.2 dB and finally reach -1 dB at 67 GHz for 10 mA, 20 mA and 30 mA respectively

### 3.3 I-V characteristics measurement and S-parameters of switches with 6 monolayers of MoS<sub>2</sub> (SS03)

This part will focus on the study of the I-V characteristics from measurement of SS03 devices for different interfaces starting with Au/MoS<sub>2</sub>/CrAu. The Ni/MoS<sub>2</sub>/Ni interface is studied and described in annex. Moreover, the S-parameters for each active part size will be analyzed alongside with the I-V characteristics.

#### 3.3.1 Switch structure with an active area of $1 \times 1 \mu\text{m}^2$

The DC and RF behaviour for the ON state of a  $1 \times 1 \mu\text{m}^2$  device with Au/MoS<sub>2</sub>/CrAu interface was given in Fig. 16. Fig. 17 represents the I-V characteristics of the same device in logarithmic scale and the OFF-state S- parameters. From Fig. 17, the isolation of the device has a value of -8 dB at 67 GHz, far from the value of an OPEN, which is around -25 dB. The difference between the ON and the OFF state is only 7 dB.

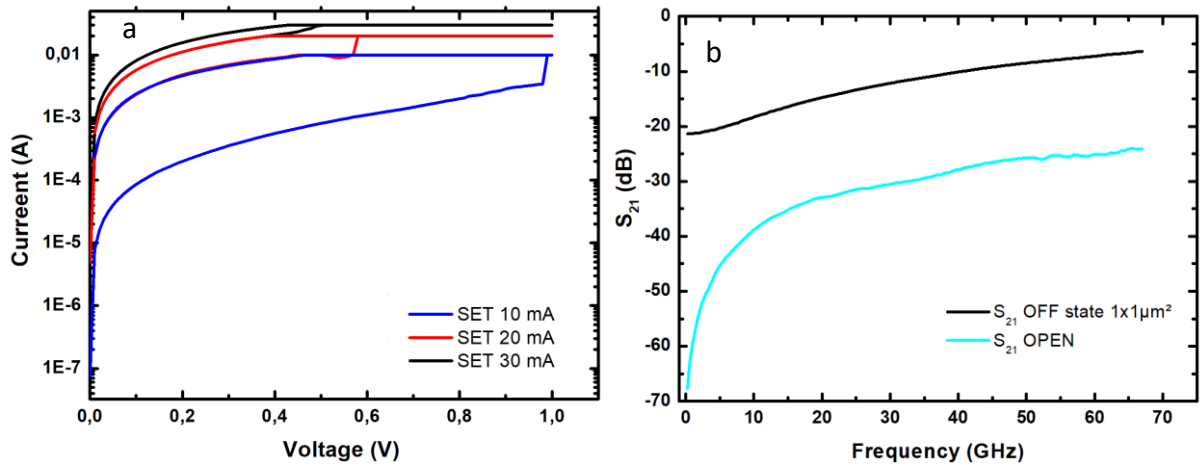


Figure 17 (a) Comparison of I-V characteristics of one  $1 \times 1 \mu\text{m}^2$  RF switch in a logarithmic scale with successive SET process. (b) Comparison of the OFF state to OPEN structure realized on-chip and measured. The device could not achieve multiple switching and only its first state after fabrication is OFF with an isolation of -8 dB at 67 GHz.

Unfortunately, for this component, it was not possible to switch it OFF efficiently; therefore, the obtained attenuation is far from the ideal OFF structure.

### 3.3.2 Switch structure with an active area of $0,5 \times 0,5 \mu\text{m}^2$

Now we will present the case of  $0.5 \times 0.5 \mu\text{m}^2$  device. Fig. 18 represents the ON state of a  $0.5 \times 0.5 \mu\text{m}^2$  size device.

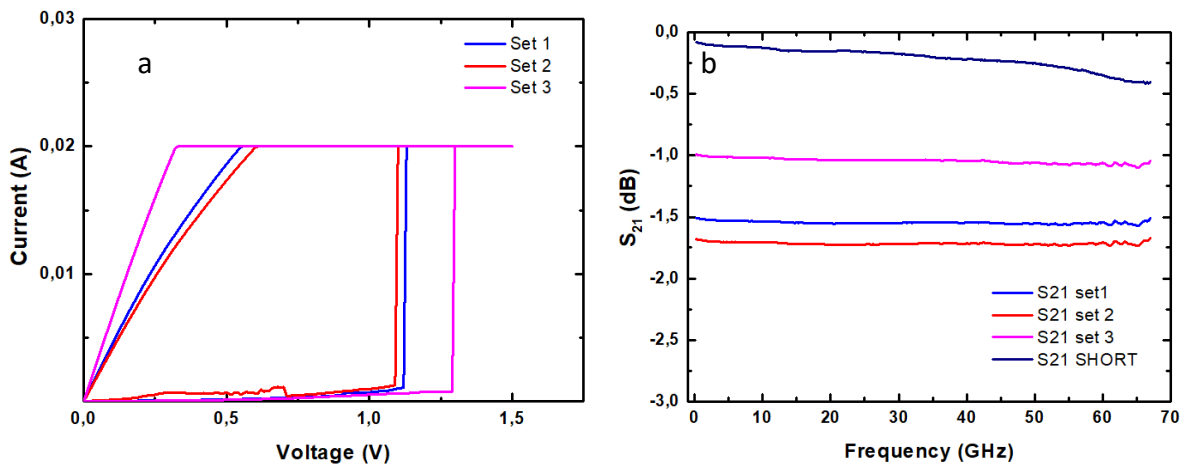


Figure 18 (a) I-V characteristics of multiple SET processes for one  $0.5 \times 0.5 \mu\text{m}^2$  device. (b)  $S_{21}$ -parameters of a single switching device with  $0.5 \times 0.5 \mu\text{m}^2$  active part. Along with the multiple switching the insertion loss improve a bit going from -1.7 dB to -1 dB at 67 GHz for the same current limitation

From Fig. 18b, we can observe that for the same current limitation this switch improves its insertion loss from -1.6 dB to -1 dB. In its OFF state, Fig. 19 shows the difference between the ON and OFF state and compares it to the OPEN. At 67 GHz, after the first RESET the isolation is at -14 dB and for the second reset at -16 dB. The difference between  $S_{21}$  in the ON and OFF state is 15 dB with the second at 67 GHz for the second reset and 13 dB at 67 GHz with the first reset.

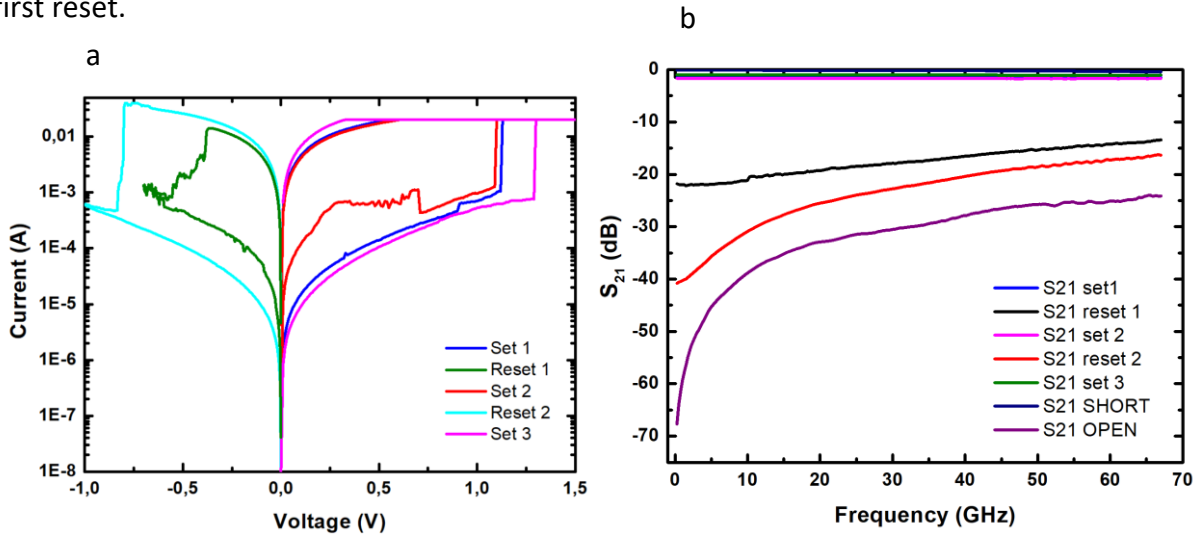


Figure 19 (a) I-V characteristics with multiple cycles for one  $0.5 \times 0.5 \mu\text{m}^2$  device with Au/MoS<sub>2</sub>/CrAu interface, the current limitation is at 20mA for SET process. (b)  $S_{21}$  parameter for ON/OFF state for one  $0.5 \times 0.5 \mu\text{m}^2$  device compared to OPEN/SHORT structure. Multiples switching devices are displayed. The insertion loss value is -1dB at 67GHz and the isolation is -21dB for the 2<sup>nd</sup> reset at 67GHz

From the I-V characteristics, the device switch has a current of  $10^{-8}$  A in the OFF state and  $10^{-4}$  A in the ON state at 0 V. From Fig. 19, the device switches from its OFF to its ON state between 1 V and 1.5 V and reset between -0.4 V and -0.9 V and the maximum current reach 40mA before switching.

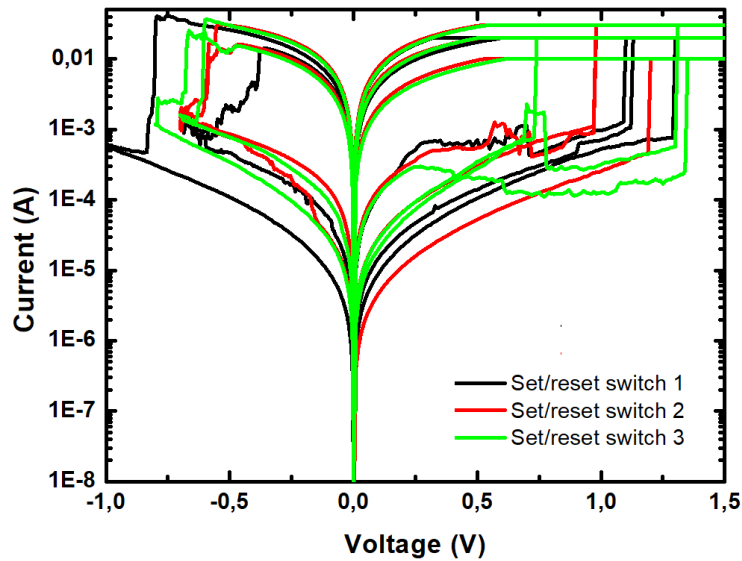


Figure 20 Summary of I-V characteristics of three different  $0.5 \times 0.5 \mu\text{m}^2$  devices with Au/MoS<sub>2</sub>/CrAu interface. Multiple switching cycles of these three devices are displayed. The switching voltage from its OFF to ON state is between 0.5 V and 1.5 V. The switching voltage from its ON state to OFF state is between -1 V and -0.5 V.

From Fig. 20, we can observe that for the  $0.5 \times 0.5 \mu\text{m}^2$  device, the set process happens between 0.5 V and 1.5 V and the reset voltage is around -0.7 V. For the current, the value is in the order of  $10^{-4}$  A in ON state and  $10^{-8}$  A in OFF state.

Twelve devices were tested out of the 20 fabricated for each dimension of the active part and are classified depending if they are working after fabrication, if they exhibit the property to switch one time or to switch multiple time. For this interface, we can observe that with the Au/MoS<sub>2</sub>/CrAu interface out of the 11 devices tested 3 devices exhibit a multiple switching behaviour for the  $0.5 \times 0.5 \mu\text{m}^2$  active part and 3 out of 6 devices exhibit it with  $0.25 \times 0.25 \mu\text{m}^2$  devices. The maximum number of switching for these devices is 2 cycles. All those data concerning the number of devices tested are summarized in table 1.



Table 1 Summary of Au/MoS<sub>2</sub>/CrAu devices tested

Active part dimension (μm <sup>2</sup> )	# Devices tested	Non-working device	# Switching behaviour observed once	# Multiple switching behaviour
1x1	15	7	7	2
0.5x0.5	15	0	15	7
0.25x0.25	16	0	16	4

In conclusion for this interface, the reliability of the devices is low with only 7 devices out of 29 that exhibit a multiple switching behaviour for all size and the maximum number of cycles realized is 3 (one cycle is one set and one reset).

The other interface on this batch is Ni/MoS<sub>2</sub>/Ni and its I-V characteristics and S-parameters are presented in the annex.

### 3.3.3 Conclusion of IV characteristics and S-parameters measurement for SS03

As show by the result exposed previously and considering the coplanar waveguide dimensions, switches with the interface Au/MoS<sub>2</sub>/CrAu reach a difference in S<sub>21</sub> of 15dB that allow a good distinction between the ON state and the OFF state at 67 GHz only for the 0.5x0.5μm<sup>2</sup> dimension. However, the reliability of the Au/MoS<sub>2</sub>/CrAu device is not good with only 3 device that show a multiple switching behaviour.

## 3.4 I-V characteristics and S-parameters measurement of Ni/MoS<sub>2</sub>/Pt interface with 6 MLs

In this sample, a second 2D materials of 6 MLs of MoS<sub>2</sub> is deposit on the SS04 batch. Two changes are present in SS04 compare to SS03. First, the metal in contact with the 2D material for the top electrode is made of Pt. Second, the structure used is the CPW structure optimized in chapter 2 to work up to 500 GHz. However, measurements are only done till 67 GHz in this

part. The dimensions of the CPW are  $W = 20 \mu\text{m}$  and a gap between the signal and the ground  $S = 5 \mu\text{m}$ .

As the second substrates possesses the same bottom electrodes than SS03, the first substrate, the choices were to change the metal top electrode to improve the number of multiple switching cycles. Pt was chosen because of its low diffusivity during fabrication. As a reminder, interfaces present in SS04 are: Au/MoS<sub>2</sub>/Pt and Ni/MoS<sub>2</sub>/Pt. I described here the results made on Ni/MoS<sub>2</sub>/Pt in terms of I-V characteristics and S-parameters for both a  $1 \times 1 \mu\text{m}^2$  device and a  $0.5 \times 0.5 \mu\text{m}^2$  device. The results concerning the interface Au/MoS<sub>2</sub>/Pt are described in annex.

### *3.4.1 Switch structures with an active area of $1 \times 1 \mu\text{m}^2$*

The I-V characteristics and S-parameters of the Ni/MoS<sub>2</sub>/Pt interfaces are represented in Fig. 27. For the switching voltage, from its OFF state to its ON state, the value is between 1.5 V and 2 V except for the last switching that happens at a much lower voltage with a value of 0.5 V. For the reset, the voltage is between -0.5 V and -1.5 V and the maximum current is of 35 mA. (Fig. 21a). For the current value in the OFF state, it is of  $10^{-10}$  A at 0 V and for the ON state, it is of  $10^{-6}$  A at 0 V. For the S-parameters highlighted in Fig. 21b, we can observe that, after fabrication the device is in its OFF state and the OFF state has a higher isolation than after being reset at least once. The value of the isolation for the OFF state after fabrication is -12 dB at 67 GHz and -30 dB after one reset. For the ON set, the value of the insertion loss is around -1.6 dB at 67 GHz. The difference in terms of  $S_{21}$  between the ON and OFF state is 28 dB.

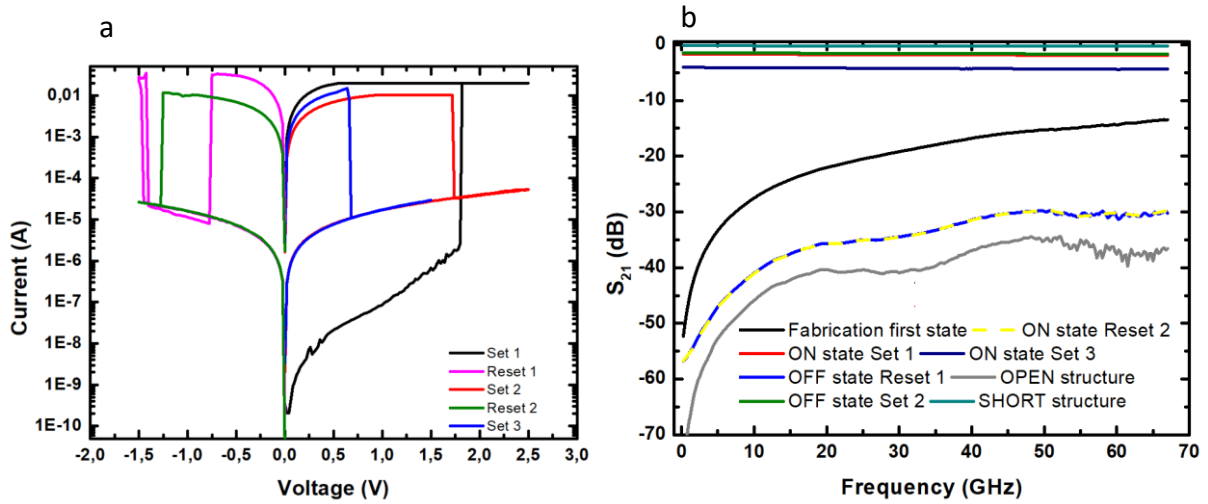


Figure 21 (a) I-V characteristics with multiple switching for one  $1 \times 1 \mu\text{m}^2$  device with Ni/MoS<sub>2</sub>/Pt interface. (b)  $S_{21}$  of Ni/MoS<sub>2</sub>/Pt interfaces for one  $1 \times 1 \mu\text{m}^2$  device and compared to the SHORT/OPEN structure fabricated on chip. Multiple switching cycle of a devices are displayed. The insertion loss value is -1.6 dB at 67 GHz and the isolation is -30 dB at 67 GHz for RESET 1.

### 3.4.2 Switch structures with an active area of $0,5 \times 0,5 \mu\text{m}^2$

Then the measurement of the  $0,5 \times 0,5 \mu\text{m}^2$  device is realized. After fabrication the device is in the OFF state. In the I-V characteristics of Fig. 22a, we observed that the maximum switching voltage from its OFF state to its ON state is 2.5 V. For the current value, in the OFF state, it reaches a value of  $10^{-11}$  A and for its ON state it reaches a value of  $10^{-5}$  A both at 0 V. In the S-parameters of Fig. 22b, the device exhibits an isolation with a value of -21 dB at 67 GHz after fabrication. The isolation value after reset is around -31 dB at 67 GHz. For the ON state of the device, the insertion loss is around -0.9 dB at 67 GHz. The difference between ON and OFF state  $S_{21}$  parameter is around 30 dB.

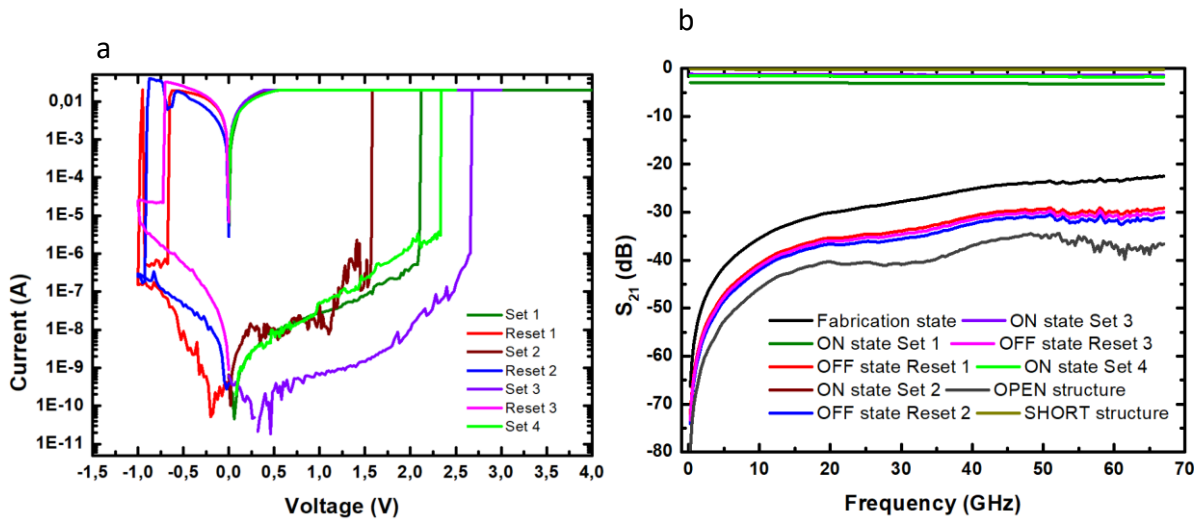


Figure 22 (a) I-V characteristics with multiple cycles of one  $0.5 \times 0.5 \mu\text{m}^2$  device with Ni/MoS<sub>2</sub>/Pt interface. (b)  $S_{21}$  parameter of Ni/MoS<sub>2</sub>/Pt interfaces for one  $0.5 \times 0.5 \mu\text{m}^2$  device and compared to the OPEN/SHORT structure fabricated on chip. Multiples switching cycles of the same device are displayed. The insertion loss of the device is 0.9 dB at 67 GHz and its isolation is -30 dB at 67 GHz.

Fig. 23 sums up the I-V characteristics for two  $1 \times 1 \mu\text{m}^2$  devices and four  $0.5 \times 0.5 \mu\text{m}^2$  devices. Overall, we observe that no change happens for the reset voltage that is between -0.5 V and -1 V and a maximum of 40 mA is reached as a reset for all devices. However, for the set part, we observe that the set voltage happens between 0.5 and 3.2 V for all devices. The more cycle a device does, the more voltage is needed.

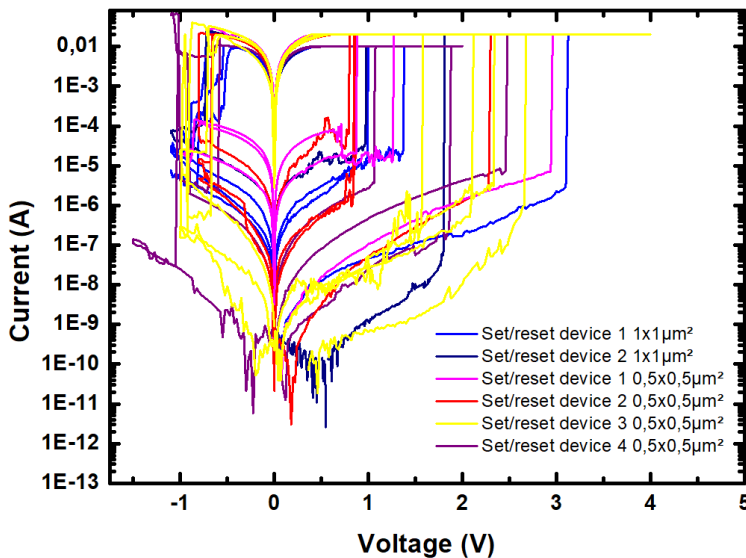


Figure 23 Summary of the I-V characteristics for two  $1 \times 1 \mu\text{m}^2$  devices and four  $0.5 \times 0.5 \mu\text{m}^2$  devices with Ni/MoS<sub>2</sub>/Pt interface with 6 MLs of 2D materials. All devices show multiple switching. The switching voltage value is between 1 V and 3 V for its state change from OFF to ON state and between -1 and -0.5V for its state change from its ON to OFF state.

Table 2 resumes the 7 tested devices out of 20 devices fabricated for  $1 \times 1 \mu\text{m}^2$  size,  $0.5 \times 0.5 \mu\text{m}^2$  size and the 5 tested device out of 20 for  $0.25 \times 0.25 \mu\text{m}^2$ . From this table we can observe that most of the devices (13 out of 14 tested) with a size of  $1 \times 1 \mu\text{m}^2$  and  $0.5 \times 0.5 \mu\text{m}^2$  could exhibit multiple switching behaviour. The maximum cycles realized is 4.

*Table 2 Summary of Ni/MoS<sub>2</sub>/Pt interface devices tested*

Active part dimension ( $\mu\text{m}^2$ )	# Devices tested	#Non-working device	# Switching behaviour observed once	# Multiple switching behaviour
1x1	7	0	7	7
0.5x0.5	7	1	6	6
0.25x0.25	5	4	1	0

### *3.4.3 Conclusion of IV characteristics and S-parameters measurement for SS04*

For all the devices measured on SS04 for the Ni/MoS<sub>2</sub>/Pt interface, no matter the dimension of its active part, the difference in  $S_{21}$  is more than 15 dB between the ON and the OFF state. They also show a good reliability except for the  $0.25 \times 0.25 \mu\text{m}^2$  dimension. For the  $1 \times 1 \mu\text{m}^2$  and  $0.5 \times 0.5 \mu\text{m}^2$ , 13 out of 14 devices tested worked and showed a multiple switching behaviour.

### 3.5 I-V characteristic and S-parameters measurement of Ni/MoS<sub>2</sub>/Pt with 3 MLs

In this part, the impact of the number of monolayers of MoS<sub>2</sub> is explored. Switches with three monolayers of MoS<sub>2</sub> are fabricated. The interface composed of Ni/MoS<sub>2</sub>/Pt is present in this batch.

MoS<sub>2</sub> was deposited on top of the bottom electrodes for a total surface around 7 cm<sup>2</sup> covering 6 out of the 9 units (Fig. 24). The goal of this sample is to compare SS04 Ni/MoS<sub>2</sub>/Pt with 6 MLs of MoS<sub>2</sub> and SS07 Ni/MoS<sub>2</sub>/Pt interface with 3 MLs.

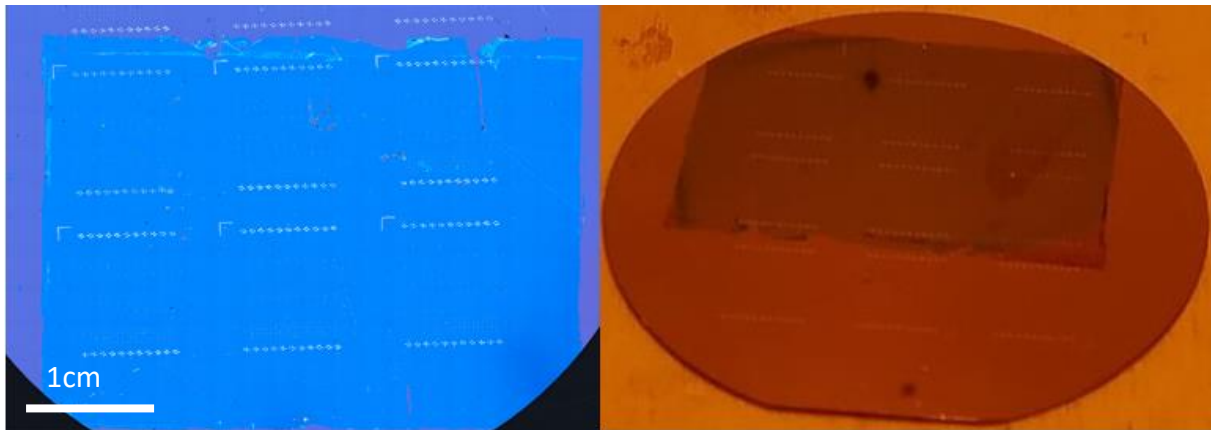


Figure 24 Optical photography of SS07 after deposition of the 3 MLs of MoS<sub>2</sub>

The device tested are from the Ni/MoS<sub>2</sub>/Pt interface. We will first take a look at the 1x1 μm<sup>2</sup> active part devices and then follow on the 0.5x0.5 μm<sup>2</sup> active part device.

### 3.5.1 Switch structures with an active area 1x1 μm<sup>2</sup>

Fig. 25a shows the I-V characteristics of one 1x1 μm<sup>2</sup> devices and S<sub>21</sub> of the same device. The I-V characteristics of Fig. 25a shows that, the device switch from its OFF-state to its ON-state at a voltage between 1 V and 2 V for the set process. For the reset process, the devices switch between -0.5 V and -1 V, the maximum current reach for the switching is higher with a maximum value of 80 mA obtained during a reset process. The current for the OFF state is 10<sup>-11</sup> A and 10<sup>-5</sup> A for the ON state at 0 V. In Fig. 25b, we can observe that, as for the previously studied device with the same interface but 6 MLs of MoS<sub>2</sub>, after fabrication the first OFF state obtainable has a higher isolation with a value of -10 dB at 67 GHz. The isolation obtains after a reset reach a value of -25 dB at 67 GHz. For the ON state of the switch, the value of the insertion loss of the device is around -1 dB at 67 GHz. The difference between the isolation and insertion loss is 24 dB and it is enough for future application to distinguish efficiently both states.

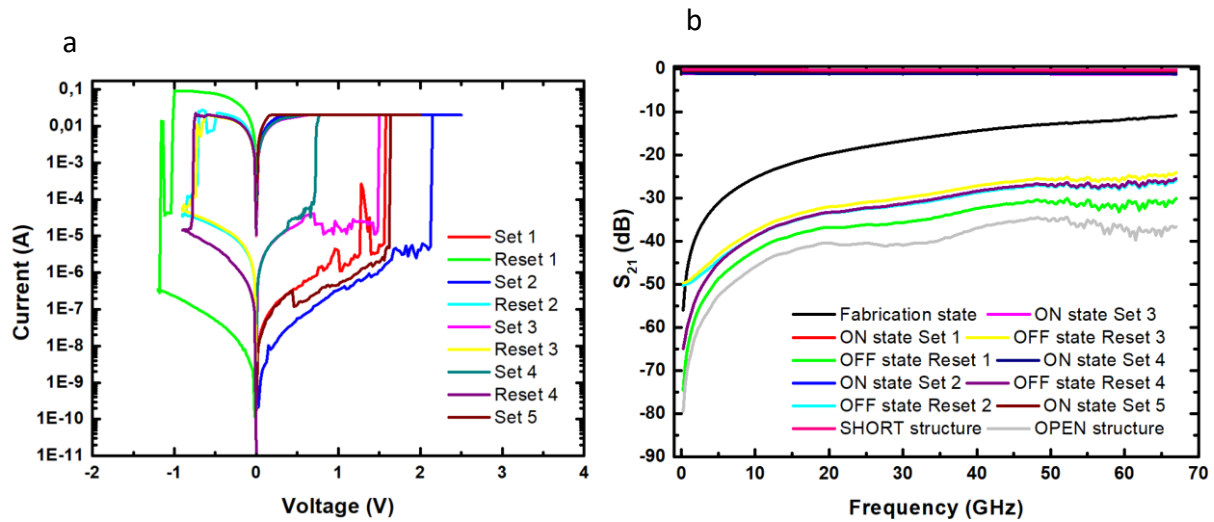


Figure 25 (a) I-V characteristics of one  $1 \times 1 \mu\text{m}^2$  device with Ni/MoS<sub>2</sub>/Pt interface with 3 MLs of MoS<sub>2</sub>. (b)  $S_{21}$  of Ni/MoS<sub>2</sub>/Pt interfaces for  $1 \times 1 \mu\text{m}^2$  device compared with OPEN structure. Multiple switching cycles of the device are displayed. The insertion loss is -1 dB at 67 GHz and the isolation is -25 dB at 67 GHz for RESET 3.

### 3.5.2 Switch structures with an active area $0,5 \times 0,5 \mu\text{m}^2$

For  $0.5 \times 0.5 \mu\text{m}^2$  device, Fig. 26 shows the I-V characteristics and the S-parameters. The I-V characteristics displayed in Fig. 26a show a switching voltage for the ON state between 1 V and 2.5 V for these devices. The switching voltage to turn the devices OFF is between -0.5 and -1 V, a current of 65 mA at maximum is reached during RESET. The OFF state current value is  $10^{-11}$  A for the OFF state and  $10^{-5}$  A for the ON state. From the S-parameters displayed in Fig. 25b, we can observe that the first state after fabrication is OFF and the isolation is -20 dB. After a cycle is realized, the isolation goes down to -30 dB at 67 GHz. This behaviour seems to happen for interfaces where the Ni is the metal of the bottom electrode. The insertion loss is -1.5 dB at 67 GHz in ON state. The  $S_{21}$  parameter difference between ON and OFF state is 28 dB.

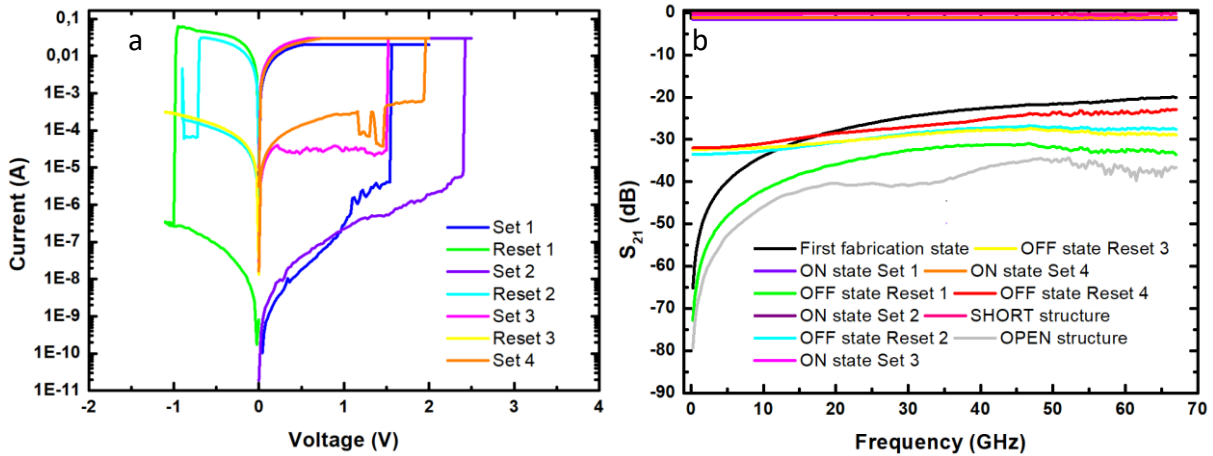


Figure 26 (a) I-V characteristics with multiple cycles for one  $0.5 \times 0.5 \mu\text{m}^2$  devices with Ni/MoS<sub>2</sub>/Pt interface. (b)  $S_{21}$  of Ni/MoS<sub>2</sub>/Pt interfaces for  $0.5 \times 0.5 \mu\text{m}^2$  device with multiple switching realized. The insertion loss is 1.5 dB at 67 GHz and the isolation is 28 dB at 67 GHz for RESET 3

Fig.27 resumes the I-V characteristics obtained for two  $1 \times 1 \mu\text{m}^2$  devices and five  $0.5 \times 0.5 \mu\text{m}^2$  devices, all them showing multiple switching behaviour for Ni/MoS<sub>2</sub>/Pt devices. The more cycles a device is making the more its switching voltage seems to increase reaching a value around 2.5 V as maximum. For the reset, the switching voltage is between -0.5 V and -1 V with a maximum of current of 80 mA reach during a reset no matter its active part size.

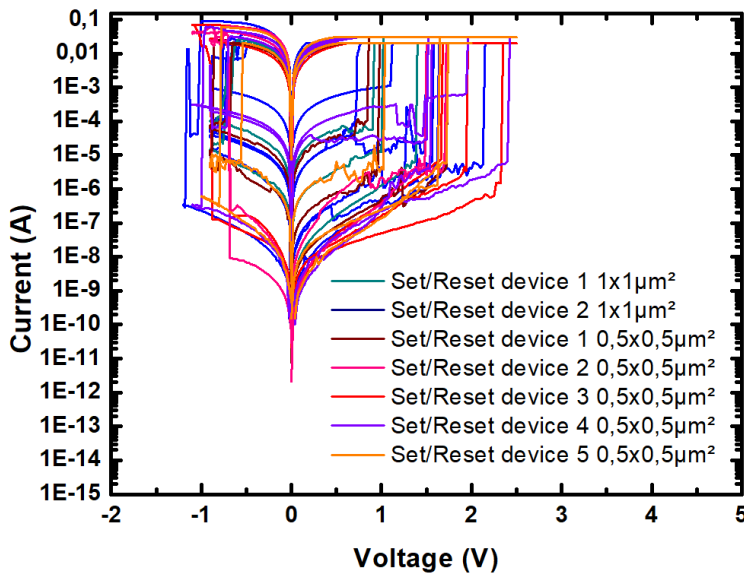


Figure 27 Summary of I-V characteristics of multiple devices with a Ni/MoS<sub>2</sub>/Pt interface. Two devices are presented with a  $1 \times 1 \mu\text{m}^2$  active part size and 5 devices are presented with a  $0.5 \times 0.5 \mu\text{m}^2$  active part. Independent on the device size, we observe a switching voltage between 0.5 V and 2 V for its state change from OFF to ON state. For its state change from ON to OFF state the switching voltage is between -1 V and -0.5 V.



Table 3 resumes the number of devices tested out of the 20 devices fabricated for each dimension of active part. Most of the devices (5 out of 8 for  $1 \times 1 \mu\text{m}^2$ , 10 out of 12 for  $0.5 \times 0.5 \mu\text{m}^2$ ) tested were working and exhibit a multiple switching behaviour. Only 3 out of 14 devices with a  $0.25 \times 0.25 \mu\text{m}^2$  size could show a multiple switching behaviour. The maximum number of cycles is still low with only 7 cycles. The reliability of this interface is then important.

*Table 3 Summary of devices tested for the interface Ni/MoS<sub>2</sub>/Pt.*

Active part dimension ( $\mu\text{m}^2$ )	# Devices tested	Non-working device	# Switching behaviour observed once	# Multiple switching behaviour
1x1	8	1	7	5
0.5x0.5	12	2	10	10
0.25x0.25	14	4	10	3

### *3.5.3 Conclusion of IV characteristics and S-parameters measurement for SS07*

All devices tested were able to reach a  $S_{21}$  difference between OFF and ON state of more than 15 dB allowing a good distinction of the state for future application (data communication). Most of the devices are multiple switching behaviour devices. However, no evident difference between the 6 MLs and the 3 MLs could be found for both SS04 and SS07 Ni/MoS<sub>2</sub>/Pt for both their I-V characteristics and S-parameters.

In the next section, we will extract an equivalent circuit model and a FOM for both of these interfaces.

## 4 De-embedding of devices and FOM extraction of 3 MLs and 6 MLs of MoS<sub>2</sub>

Based on the de-embedding technique explained in chapter 2, we can extract the  $C_{\text{OFF}}$  and  $R_{\text{ON}}$  of the devices from the S-parameters.

Table 4 shows the extracted parameters from Ni/MoS<sub>2</sub>/Pt for SS04 with 3 MLs and SS07 with 6 MLs. C<sub>OFF</sub> is extracted for the first state after fabrication where we can observe a clear difference between the 3 MLs and 6 MLs devices and for the 1<sup>st</sup> reset of the device. R<sub>ON</sub> is also display for the first and second set applied to the device. The FOM calculated from the R<sub>ON</sub> and C<sub>OFF</sub> is presented.

Table 4 FOM extracted from SS04 and SS07 to compare the 3MLs and the 6MLs MoS<sub>2</sub>

Device	Number of MLs of 2D	Active part Dimension (μm <sup>2</sup> )	R <sub>on</sub> (Ω) 1 <sup>st</sup> set	C <sub>OFF</sub> (fF) for fabrication state	R <sub>on</sub> (Ω) 2 <sup>nd</sup> set	C <sub>OFF</sub> (fF) first reset	F <sub>c</sub> (THz) fabrication state	F <sub>c</sub> (THz) 1 <sup>st</sup> reset
SS04_Ni/MoS <sub>2</sub> /Pt	6	1x1	32	6.3	20.5	1.13	0.79	6.87
SS04_Ni/MoS <sub>2</sub> /Pt	6	1x1	26.5	6.12	23.5	0.89	0.98	7.59
SS04_Ni/MoS <sub>2</sub> /Pt	6	1x1	15.67	5.8	20.9	1.14	1.75	6.68
SS04_Ni/MoS <sub>2</sub> /Pt	6	1x1	16.45	5.79	/	/	1.67	/
SS04_Ni/MoS <sub>2</sub> /Pt	6	0.5x0.5	17.05	1.46	17.25	0.8	6.39	11.53
SS04_Ni/MoS <sub>2</sub> /Pt	6	0.5x0.5	12.1	1.53	11.34	0.66	8.6	21.27
SS07_Ni/MoS <sub>2</sub> /Pt	3	1x1	15	8.6	9.28	1.37	1.23	12.48
SS07_Ni/MoS <sub>2</sub> /Pt	3	1x1	9.25	7.9	/	/	2.15	/
SS07_Ni/MoS <sub>2</sub> /Pt	3	0.5x0.5	16	3.3	13.5	1.24	3.01	9.51
SS07_Ni/MoS <sub>2</sub> /Pt	3	0.5x0.5	17.9	3.38	10.4	1.38	2.63	11.09

The extracted C<sub>offextr</sub> capacitance for the first OFF state after fabrication is compared to the static capacitance, C<sub>OFF</sub>, given by the expression:

$$C_{off} = \epsilon_r * \epsilon_0 * \frac{S}{d}$$

With C<sub>off</sub> in [F], E<sub>r</sub> the relative permittivity, ε<sub>0</sub> the permittivity of the vacuum, S the surface and d the thickness of the 2D material. S correspond at the surface of the active part ranging from 1 μm<sup>2</sup> to 0.25 μm<sup>2</sup>. The thickness of the 2D material were estimated to be 3 nm based on TEM (Fig. 28) image taken on SS07 where 3 MLs of MoS<sub>2</sub> could be observed and an AFM

measurement determined the thickness of 6 MLs of MoS<sub>2</sub> at 6 nm (Fig. 6). The relative permittivity chosen was 3.7 that correspond to the permittivity of a ML of MoS<sub>2</sub> [2].

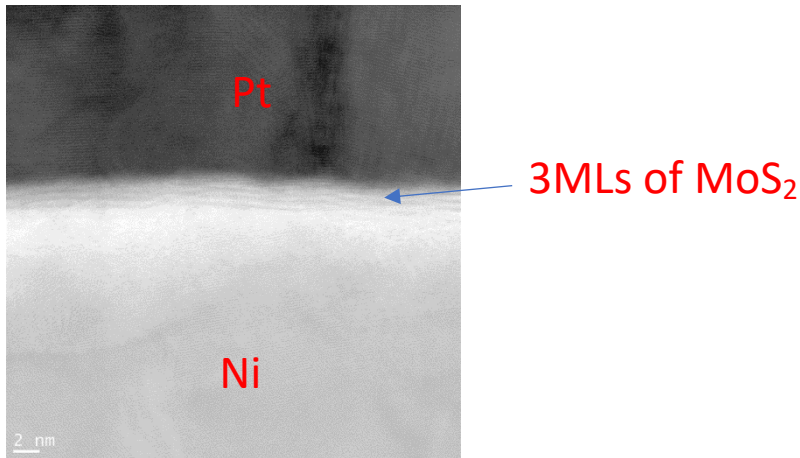


Figure 28 TEM image of SS07 Ni/MoS<sub>2</sub>/Pt interface where the 3MLs of MoS<sub>2</sub> are observable

From this equation we can plot the static value of C<sub>OFF</sub> for each SS04 (6 MLs) and SS07 (3 MLs) and compare their extracted values with the calculated ones (Fig. 29). From this graph we can see that the extracted value is close to the calculated one.

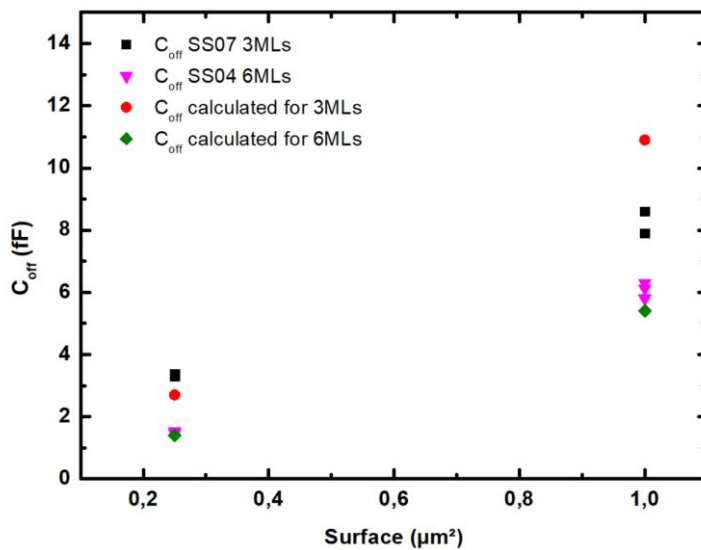


Figure 29 Comparison of C<sub>OFF</sub> for SS07 (3 MLs) and SS04 (6 MLs) for the fabrication state with the interface Ni/MoS<sub>2</sub>/Pt. The calculation and the extracted value are close to each other with a value of 3fF for the calculated and the measured C<sub>OFF</sub> for a 0.25x0.25 μm<sup>2</sup> device for example.

Both table 5 and Fig. 29 show that the device has a different C<sub>OFF</sub> that depends on the number of MoS<sub>2</sub> layers and is consistent with the theory because the calculated value for C<sub>OFF</sub> based on the planar capacitor matches the value extracted from the measurement for the first state

obtain after fabrication. The value for a  $0.5 \times 0.5 \mu\text{m}^2$  device is around 3.3 fF for 3 MLs devices and 6.25 fF for 6ML device. However, once the switch has performed some cycles this difference is not observed and they cannot be differentiated.

## 5. Conclusion

In this chapter the fabrication process that was used as a general-purpose process for RF switch was presented. The step presented are the fabrication of the alignment marks, with an etching of the substrate. Then the fabrication of the bottom electrode by evaporating different metal like Au and Ni. The transfer of the  $\text{MoS}_2$  was done by our collaborator CEA Leti. The patterning and etching the  $\text{MoS}_2$  are presented. It followed the deposition of the top electrode. Finally, the deposition of the CPW structure that was simulated in chapter 2, is realized by metal evaporation of 50nm of Ni as an adhesion layer and 500 nm of Au.

The second part of this chapter is the analysis of the I-V characteristics and S-parameters of the devices fabricated previously. We describe typical I-V characteristics and S-parameters for interfaces, starting with SS03 6 MLs Au/ $\text{MoS}_2$ /CrAu. The  $0.5 \times 0.5 \mu\text{m}^2$  active part size could reach 14 dB difference between the ON and OFF state and the  $1 \times 1 \mu\text{m}^2$  could reach a difference of 7 dB. We could observe that by increasing the limit of the current for the ON state of our devices we could improve the insertion loss. These devices reached the highest switching current during the switching from the ON to the OFF state, with value around 35 mA. Then sample SS04 is described starting by noticing the use of Pt for top electrode and the difference in the structure deposited and optimized for higher frequency than the previous sample. SS04 present also new interface; Ni/ $\text{MoS}_2$ /Pt. The interface Ni/ $\text{MoS}_2$ /Pt shows interesting result with a better reliability. We could reach the 15 dB goal for all active part dimension.

This interface that is also present on SS07 substrate which possess 3 MLs of  $\text{MoS}_2$ . This allowed us to compare the SS04 one with 6 MLs and the SS07 on with 3 MLs. Both show a difference of more than 15 dB between the  $S_{21}$  parameter for their OFF and ON state for their  $1 \times 1 \mu\text{m}^2$  and  $0.5 \times 0.5 \mu\text{m}^2$  active part devices.

They could withstand a similar number of maximum cycle and their reliability is similar. Furthermore, their I-V characteristics are close to each other. They also display a similar behaviour for their S-parameters.

The difference between 3 MLs and 6 MLs devices was only observed on the first OFF state after fabrication. We could observe that the value of  $C_{OFF}$  of the device match the simple model of a plan capacitor and then show the distinction between the 3MLs and 6MLs with a  $C_{OFF}$  capacitance higher for the 3MLs than the 6MLs. However, after starting the cycling of the devices, no distinction could be obtained between the  $C_{OFF}$  value of the 6ML devices and the 3 MLs devices. The FOM, extracted from the best device after cycling, are  $R_{ON} = 11.34 \Omega$ ,  $C_{OFF} = 0.66 \text{ fF}$  and a cut off frequency of  $F_c = 21.27 \text{ THz}$ .

To conclude about the different size of the devices and the different interfaces, the most reliable size, no matter of which metal is used, is  $0.5 \times 0.5 \mu\text{m}^2$ . Furthermore, all devices with this size shows a difference between the ON and OFF state of at least 14 dB which allows to have a good distinction between the ON and OFF state for future application.

As conclusion about the interfaces, Au/MoS<sub>2</sub>/CrAu could reach an 8 dB difference between  $S_{21}$  parameters in ON and OFF state and this interface might not be the best with 6 MLs of MoS<sub>2</sub>. Ni/MoS<sub>2</sub>/Pt possess the best isolation.

## 6. References

- [1] S. Cadot *et al.*, « A novel 2-step ALD route to ultra-thin MoS<sub>2</sub> films on SiO<sub>2</sub> through a surface organometallic intermediate », *Nanoscale*, vol. 9, n° 2, p. 538-546, 2017, doi: 10.1039/C6NR06021H.
- [2] Y. Li *et al.*, « Resistive switching properties of monolayer h-BN atomrictors with different electrodes », *Appl. Phys. Lett.*, vol. 120, n° 17, p. 173104, apr. 2022, doi: 10.1063/5.0087717.
- [3] S. M. Hus *et al.*, « Observation of single-defect memristor in an MoS<sub>2</sub> atomic sheet », *Nat. Nanotechnol.*, vol. 16, n° 1, p. 58-62, jan. 2021, doi: 10.1038/s41565-020-00789-w.
- [4] M. Kim *et al.*, « Analogue switches made from boron nitride monolayers for application in 5G and terahertz communication systems », *Nat. Electron.*, vol. 3, n° 8, p. 479-485, agu 2020, doi: 10.1038/s41928-020-0416-x.

- [5] M. Kim *et al.*, « Monolayer molybdenum disulfide switches for 6G communication systems », *Nat. Electron.*, may 2022, doi: 10.1038/s41928-022-00766-2.
- [6] R. Ge *et al.*, « Atomristor: Nonvolatile Resistance Switching in Atomic Sheets of Transition Metal Dichalcogenides », *Nano Lett.*, vol. 18, n° 1, p. 434-441, jan. 2018, doi: 10.1021/acs.nanolett.7b04342.
- [7] D. Davelou, G. Kopidakis, G. Kioseoglou, et I. N. Remediakis, « MoS<sub>2</sub> nanostructures: Semiconductors with metallic edges », *Solid State Commun.*, vol. 192, p. 42-46, aug. 2014, doi: 10.1016/j.ssc.2014.04.023.

# CHAPTER IV Linearity and data communication

# Table of Contents

CHAPTER IV Linearity and data communication .....	94
1. Introduction.....	96
2. Linearity.....	97
2.1. IP3 measurement principle.....	98
2.2. Polynomial fit and extraction for ADS simulation.....	100
2.3. Result of the IP3 measurement .....	102
2.4. IP3 conclusion .....	104
3. Real life scenario: data communication.....	104
3.1. Structures of switches used for data communications .....	104
3.2. RF characteristics of switches used for data communications.....	105
3.3. Setup for data communication at 100 GHz .....	107
3.4. RF result on data communication at 100 GHz .....	109
3.5. Data communication at 320 GHz .....	111
3.6. Setup for data communication at 320GHz and advanced vectorial modulation 112	
3.7. RF result on data communication at 320 GHz .....	113
4. Conclusion .....	116
5. References.....	117



## 1. Introduction

This chapter is divided in two parts, the first part focuses on a study on the linearity of the 2D material based RF switch made at IEMN and a second part focuses on a data communication of devices made in collaboration with the University of Texas at Austin.

First, a study of the linearity of the devices that is important for broadband communication at high frequency is realized. [1] Since RF input power can induce self-heating and may impact the electrical properties, the ON state variation can cause nonlinearity. A description of the measurement set up process for linearity measurements is reported followed by the result of the study on our devices with two different interfaces. The effect of the different current limitation on the linearity of the device is also handled in this study. The calibration is explained in the annex. Furthermore, the extraction of polynomial parameters on the linear part from DC measurement of the switch allows to simulate the IP3 of the device by using an ADS schematic. This simulation goal is to estimate without measurement the IP3 value. The accuracy of the proposed approach is validated by comparing simulations to measurements.

Secondly in this chapter, a real-time experiment is performed with two data communication one at 100 GHz with one ML hBN device made from a first batch and another one at 320 GHz made with one ML of MoS<sub>2</sub> devices from the second batch of devices with the structure described in chapter 2. Both devices are made by the University of Texas and are a work in collaboration between University of Lille and University of Texas. The goal of the 100 GHz system is to determine the best data rate obtainable with a simple on-off keying (OOK) modulation and the bit error rate (BER) of this approach. The second data communication goal is to match the requirement of the new IEEE 6G requirements [2] which are a high carrier frequency (around 300 GHz) with advanced modulation and high data rate. The second setup works with a carrier frequency of 320 GHz and advanced modulation can be generated and send through our devices. From both of these data communication setups, S-parameters, data rates and bit error rate (BER) result are studied. Furthermore, the signal noise ratio (SNR) and the error vector magnitude (EVM) are reported for the second data communication system.

## 2. Linearity

According to previous studies [3]–[5], the I-V characteristics of switches are not perfectly linear. This nonlinearity is due to heating of our devices caused by the DC bias power through the devices. Moreover, according to previous research if the compliance current increases, the ON resistance decreases. Similarly, when the power of the input RF signal applied to the switch is increased, this may generate self-heating that may induce change in the ON state electrical properties and generate nonlinearity. The devices described in this work have similar behaviour regardless of the interfaces used, as shown in Fig. 1.

Typically, the nonlinear performance of a device is defined by the third-order intercept point (IP3). The IP3 is a purely mathematical concept and does not correspond to a practically occurring physical power because it lies far beyond the damage threshold of a device. The IP3 is based on intermodulation products. The device is fed with two signals at two different frequencies,  $f_1$  and  $f_2$ . Both of these signals generate intermodulation frequencies at various frequencies including two frequencies close to  $f_1$  and  $f_2$ ; they are  $2f_1-f_2$  and  $2f_2-f_1$ . The IP3 is obtained graphically by plotting the output power versus the input power on a logarithmic scale for  $f_1$ ,  $f_2$ ,  $2f_1-f_2$ , and  $2f_2-f_1$ . The IP3 point represents the intersection of the main frequencies with a slope of 1 by the third-order frequencies with a slope of 3. It represents a purely mathematical point where the power of the third order frequency is equal to the one of the main frequencies. Therefore, the higher the IP3 value is, the better the linearity and so it is an important figure of merit for data communication systems. In this chapter a setup is described to measure the third-order intercept point (IP3). [1] After the explanation of the setup for the linearity measurement, the focus is put on using the I-V characteristics of a switch to simulate its IP3 and compare it with the measurement realized. As shown in Fig. 1 we can observe in the ON state of our device that the I-V characteristics is nonlinear (steps 4-5 in Fig. 1). This is also the case in the OFF state (steps 7-1 in Fig. 1).

These parameters could be achieved by calculation based on the I-V characteristics of a switch combined to efficient software tools (ADS model is used here). These analyses are compared with measurements for validation.

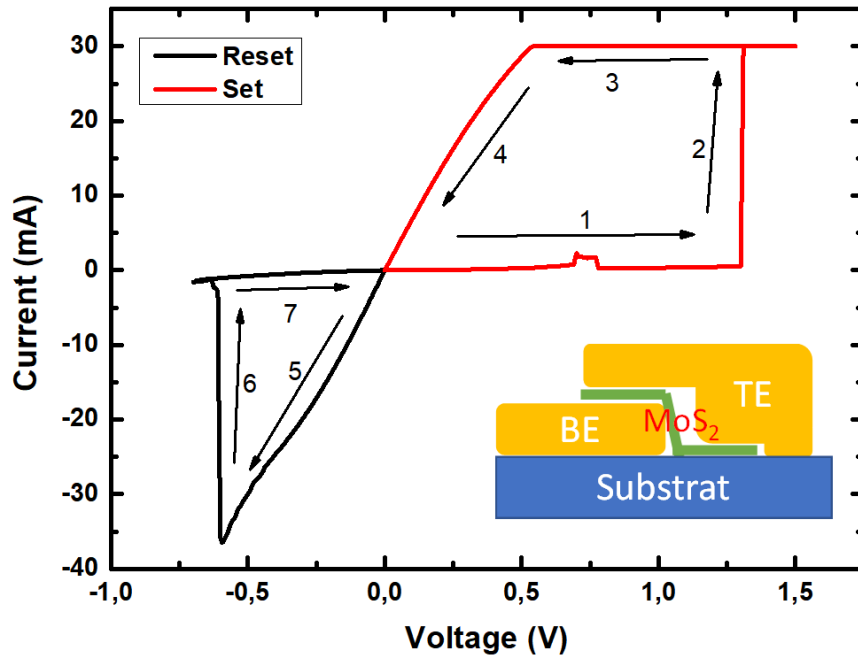


Figure 1 Typical IV measurement from a MoS<sub>2</sub> RF switch made at IEMN

A study regarding the impact of the limitation current used for the ON switching on the linearity is conducted.

## 2.1. IP3 measurement principle

To measure the IP3, the device under test (DUT) has to be excited with two signals at two different frequencies  $f_1$  and  $f_2$ . With this excitation, the device generates at its output two new intermodulation signals at frequencies  $2f_1 - f_2$  and  $2f_2 - f_1$ . After sweeping the input power, we can plot the characteristics of the input power vs the output power at the frequency  $f_1$  (or  $f_2$ ) and  $2f_2 - f_1$  as function of the input power. The IP3 is defined by the intersection point of these two characteristics after a linear fitting on a log scale.

This measurement is realized on a setup that was specifically developed at IEMN (Fig. 2) which is illustrated in Fig. 3.

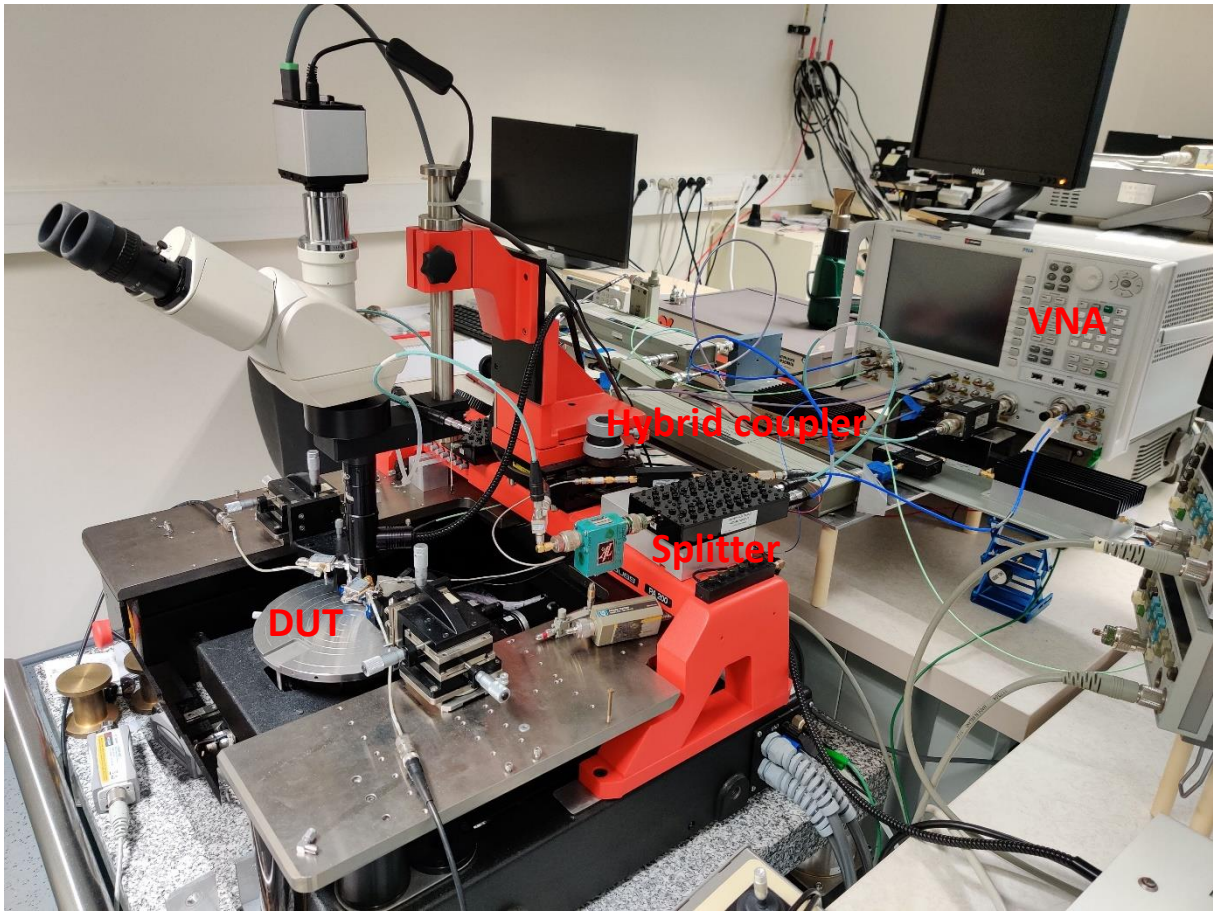


Figure 2 IP3 measurement setup including VNA

A 4-port-Vector Network Analyzer (VNA) and two sources (Keysight PNA-N5222A) are used. The VNA generates and measures the signal that is transmitted to the DUT. Its two sources generate the two input signals at  $f_1$  (2,365 GHz) and  $f_2$  (2.415 GHz) which are then amplified to achieve a larger sweep range than the one available with the PNA alone. The signals are then mixed and applied to the DUT input. Several filters refine the signal and improve its spectral purity before the DUT. At the output of the DUT, a diplexer separates the main signals ( $f_1$  and  $f_2$ ) and the intermodulated signal ( $2f_2-f_1$ ) and send both separated signal to the VNA to be measured distinctly and to optimize the measurement quality.

The calibration of the setup is described in the annex.

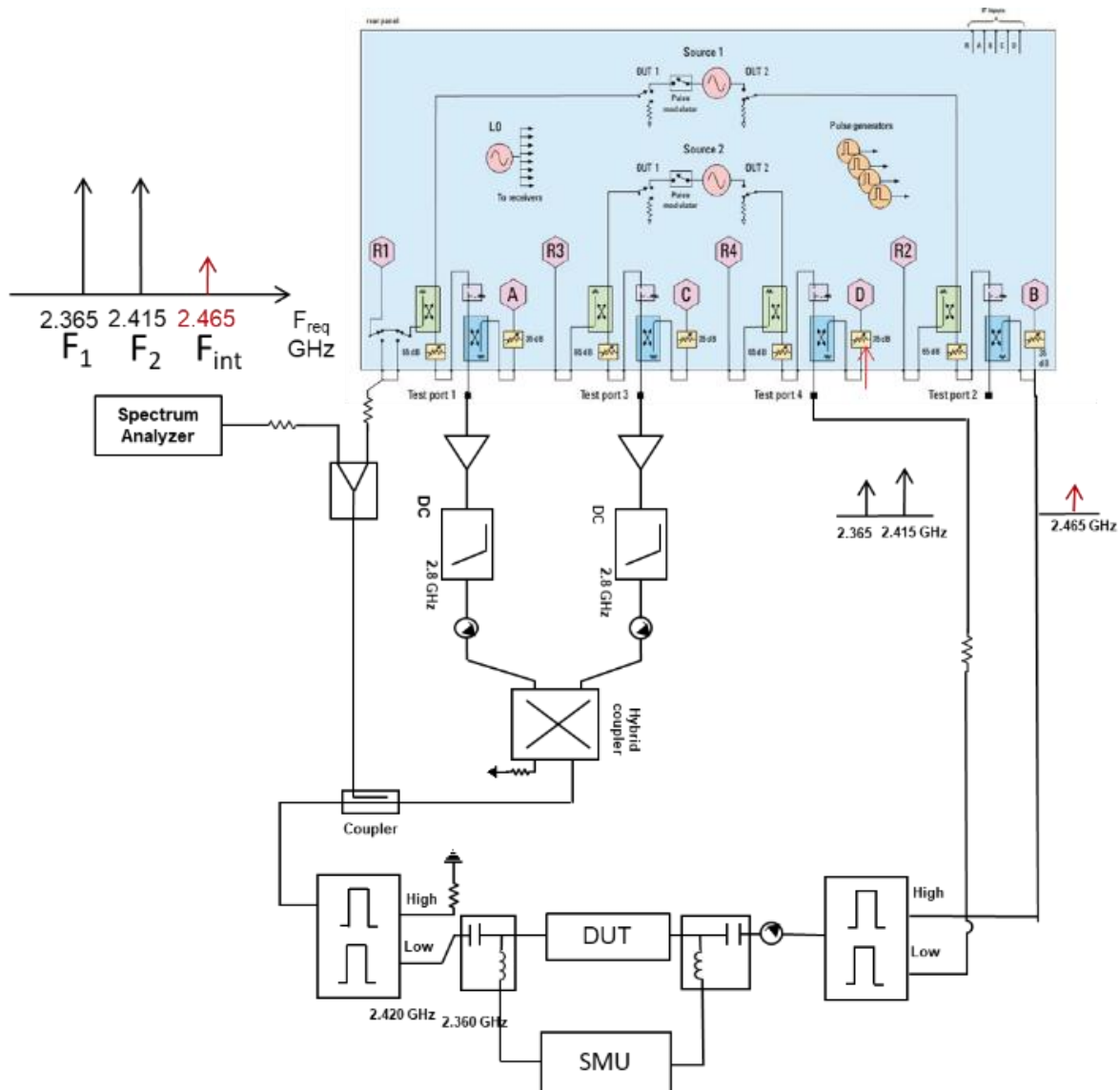


Figure 3 Schematic of the IP3 measurement setup

## 2.2. Polynomial fit and extraction for ADS simulation

The I-V is taken from the DUT before and after the IP3 measurement to be able to observe any changes happening to the switch. From this measurement, one can extract the polynomial factors up to the 3<sup>rd</sup> order by fitting the I-V in its linear part with a polynomial curve.

The current is approximated by the following equation using the coefficient obtained by the polynomial fitting:

$$I(V_{in}) = \beta_1 V_{in} + \beta_2 V_{in}^2 + \beta_3 V_{in}^3 \dots$$

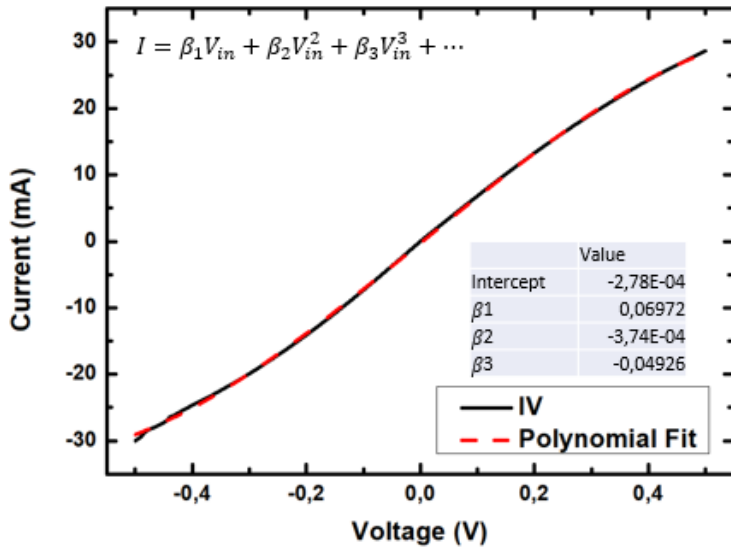


Figure 4 Zoom in on the quasi-linear part of a RF switch

The polynomial coefficients are injected into a simple ADS schematic to simulate the IP3. This schematic allows to use the symbolically-defined (SDD) block to simulate a device by using the extracted polynomial I-V parameters from the native device (Fig 5). Then from this schematic, the IP3 measurement is obtained by simulating an excitation of two signals at  $f_1$  and  $f_2$  with a sweep for the input power in a range from -30dB to -5dB.

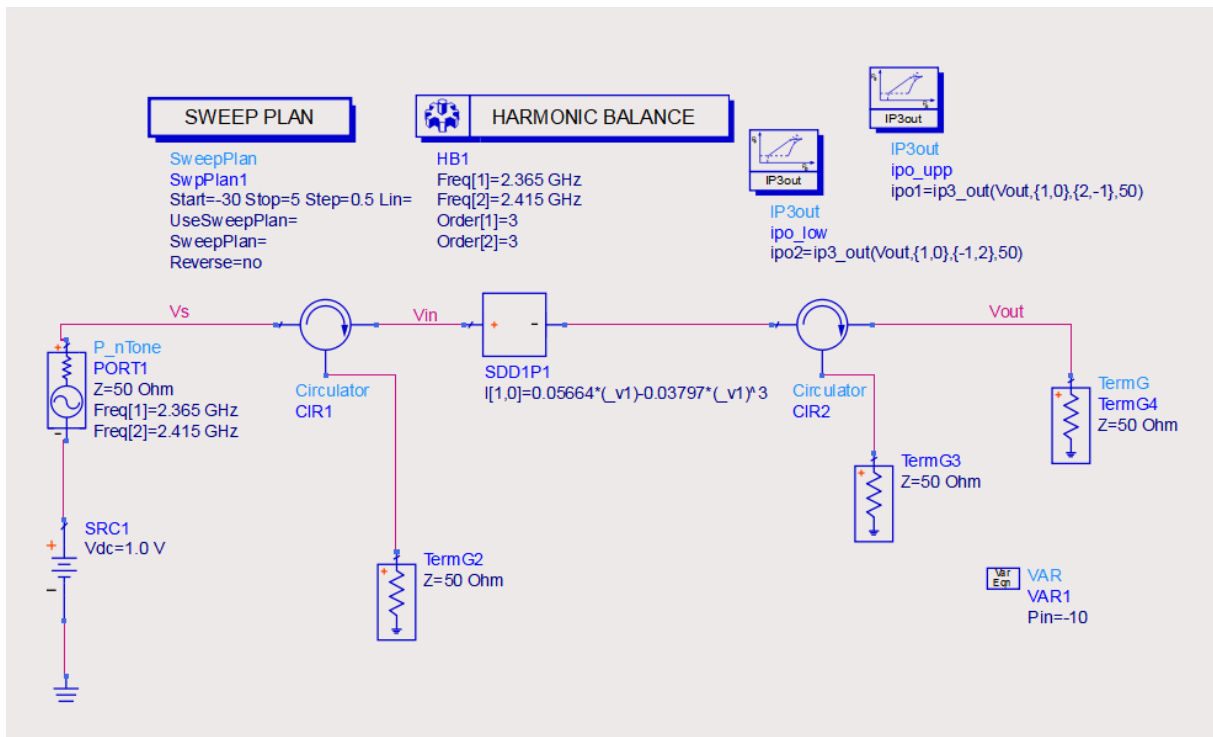


Figure 5 Schematic of the IP3 simulation schematic used in ADS

The resulting IP3 simulated by ADS is then compared to the measured one (Fig. 6).

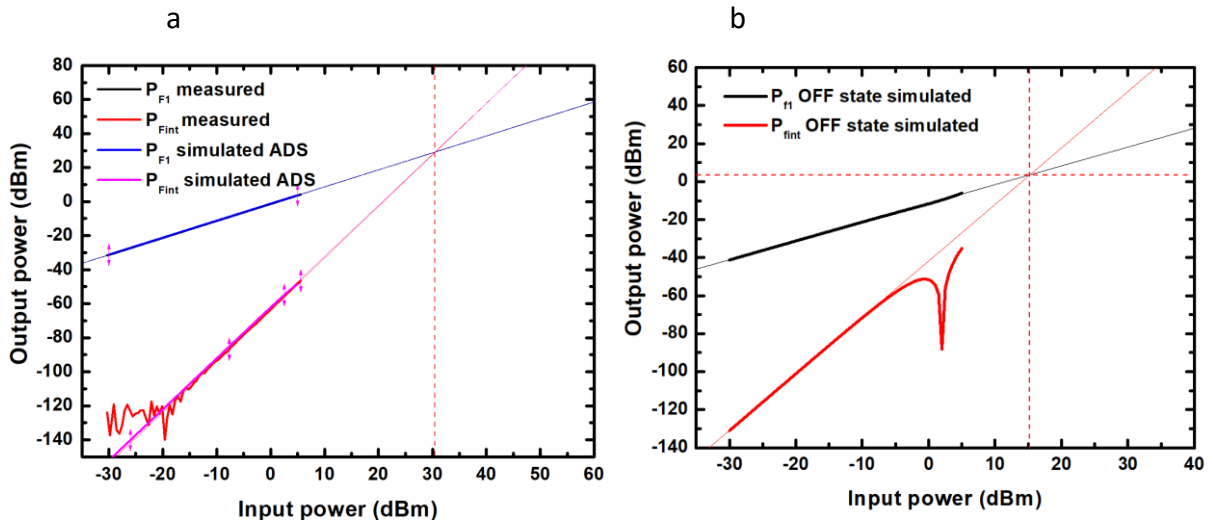


Figure 6 IP3 comparison between measurements and the ADS simulations for SS03\_37 with 3 ML and a  $0.5 \times 0.5 \mu\text{m}^2$  active part size and (b) simulation of the OFF state based on the OFF state of SS03\_37

We can observe in Fig. 6 that simulations and measurements are in agreement. This allows us to try and simulate the OFF state of this device using the I-V characteristics of the device (steps 7-1 in Fig. 1) for which we obtain a IP3 value of 15 dBm which is close to the value measured for the 2D switch in [6].

With this technique, we can analyze the IP3 of some of the components that were fabricated before and study their associated linearity.

The following part will focus on the study of the linearity of SS03 depending on the interface and the current limitation during the ON state switching.

### 2.3. Result of the IP3 measurement

This part focuses on the results on two interfaces from the SS03 substrate. All results are from switches that show a multiple switching behaviour (at minimum of 2 cycles are reached by the device). During the IP3 measurement, I-V characteristics were taken before and after the measurement to ensure device stability during the IP3 characterization. Furthermore, depending on the switch, the impact of the applied current limitation on this parameter is studied. First, table 1 resumes the different devices tested and the results for the simulations, measurements in function of their current limitation during the ON state for Au/MoS<sub>2</sub>/CrAu interfaces.



Table 1 IP3 simulation and measurement for SS03 Au/MoS<sub>2</sub>/CrAu interface

Device	Active part size ( $\mu\text{m}^2$ )	IP3 measured (dBm)	IP3 simulated (dBm)	Current limitation (mA)
SS03_24	1x1	37	35	30
SS03_37	0.5x0.5	30	30	30
SS03_55	0.25x0.25	26	25	20
SS03_56	0.25x0.25	27	25	20

Table 2 resumes the devices for Ni/MoS<sub>2</sub>/Ni interfaces.

Table 2 IP3 simulation and measurement for Ni/MoS<sub>2</sub>/Ni interface on SS03

Device	Active part size ( $\mu\text{m}^2$ )	IP3 measured (dBm)	IP3 simulated (dBm)	Current limitation (mA)
SS03_22	1x1	35	32	30
SS03_36	0.5x0.5	25	22	20
SS03_37	0.5x0.5	25	22	20
SS03_38	0.5x0.5	32	30	30
SS03_57	0.25x0.25	25	22	20
SS03_59	0.25x0.25	31	29	30

These results show that:

- Simulations are in agreement with experimental data
- For a given current limitation, IP3 increase with devices size
- For a given device size, by increasing the ON current from 20mA to 30 mA, a small improvement in IP3 is observed. This could be related to the improvement of insertion loss associated to the switch. As a consequence, the linear region of the switch is extended.



- No impact of the type of metallic electrodes on device linearity, considering the same conditions (current saturation, geometry, ...) is observed. For the Au/MoS<sub>2</sub>/CrAu and Ni/MoS<sub>2</sub>/Ni interfaces, we can observe that devices which possess a better linearity, *i.e.*, an IP3 of more than 30dBm are the switches with higher current limitation in their ON state. The error between measurement and simulation is also reasonable with a maximum difference of 3 dBm for the lowest IP3 value.

The measurements made on switches with 3 monolayers of MoS<sub>2</sub>, SS07 and the metal interfaces composed by of Ni/MoS<sub>2</sub>/Pt are given in the annex. Similar results are obtained. Therefore, considering the conditions of the measurement with 30 mA current limitation, the impact of metal interfaces is negligible.

## 2.4. IP3 conclusion

In this part we observed that the linearity of the device depends on the current limitation during the switching in the ON state of the device and it is better if the device is switched with a higher current limitation. An IP3 over 30 dBm for a 30 mA current limitation is greater than the IP3 measured with a current limitation of 20 mA (25 dB). Furthermore, the simulation of the IP3 shows a result close to the measured one with an error of maximum 3 dB between the simulation and the measurement for the high current limitation device.

## 3. Real time scenario: data communication

### 3.1. Structures of switches used for data communications

In collaboration with the University of Texas in Austin, two batches of RF switches based on a monolayer of 2D material were fabricated, with hBN and MoS<sub>2</sub> respectively. The RF switch structure based on hBN and fabricated during the first batch is represented in Fig. 7a. The atomic force microscopic (AFM) representation shows the active part of the device where the 2D material is present between the top and the bottom electrode. (Fig. 7b)

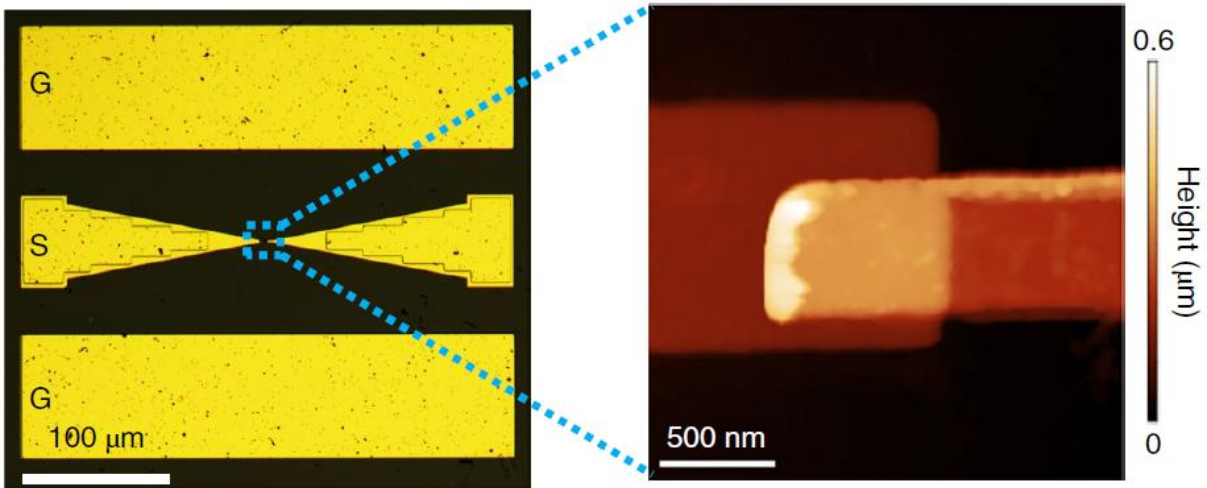


Figure 7 (a) Optical microscopy image of a monolayer hBN RF switch with GSG Au electrodes (b) Representative AFM image of the active part region with  $0.5 \times 0.5 \mu\text{m}^2$  active part area from [3]

The second one based on a monolayer of MoS<sub>2</sub> is represented with an AFM image of its active part in Fig. 8. For these devices, the transmission lines designed for high frequency applications (see chapter 2) are used. These devices are fabricated at the University of Texas in Austin on diamond substrates, in order to manage thermal conduction problems which are observed on some devices on SiO<sub>2</sub>/Si substrate. [3]

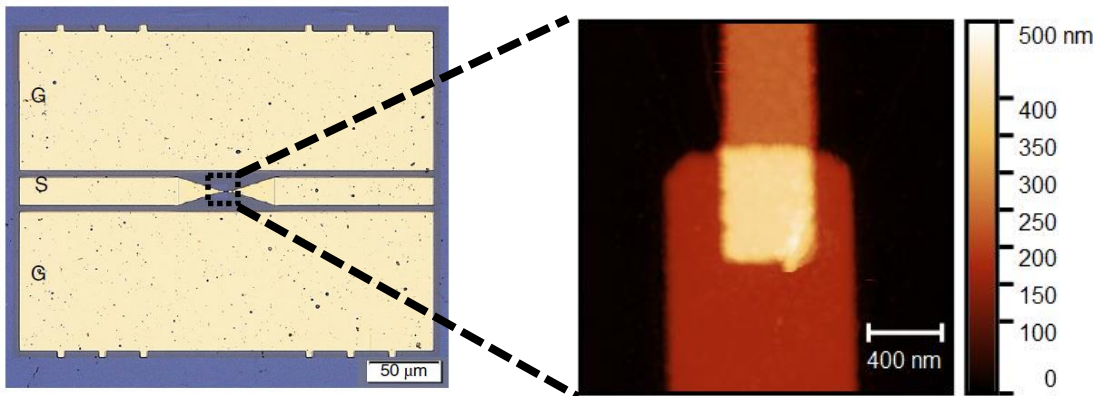


Figure 8 Optical microscopy image of an MoS<sub>2</sub> RF switch with GSG Au electrode from [6] (b) Representative AFM image of the active part region with  $0.5 \times 0.5 \mu\text{m}^2$  active part area

### 3.2. RF characteristics of switches used for data communications

The devices are switched into the ON state with a current limitation of 30 mA, in order to set the insertion loss at the minimum value (lower ON resistance).

The S-parameters of the hBN devices were measured in IEMN up to 220 GHz. Figure 8 shows the  $S_{21}$  parameter for the ON state (in blue) and the OFF state (in red) of the same device. This gap allows us to perform a data communication test at 100 GHz using this device to highlight its potential in a real-life scenario. Furthermore, as latency time is one of the key points for future high bandwidth networks, a real time BER testing is realized. Its goal is to determine the quality of the signal transmitted by indicating the number of incorrectly received bit.

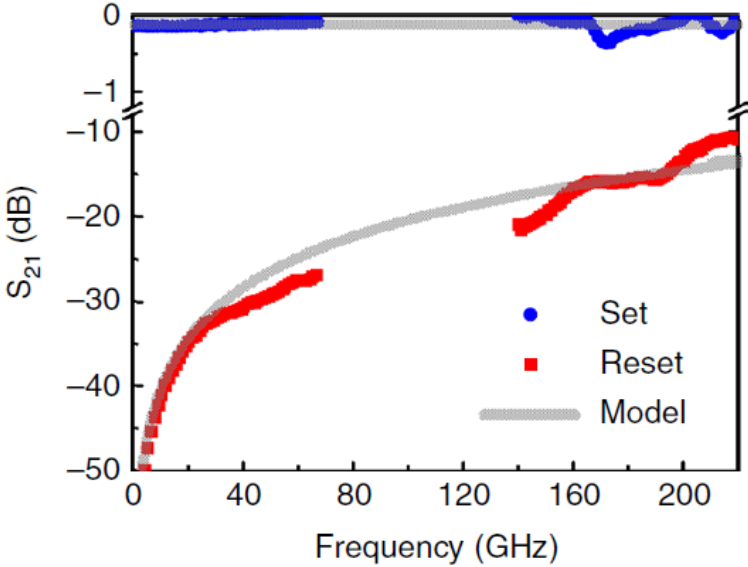


Figure 9 Measured S-parameter data and simulated result from 0-67 GHz and 140-220 GHz from [3]

After the 100 GHz data communication, another data communication at 320 GHz is realized with a device which possess a structure optimized at IEMN to reach 500 GHz and fabricated at the University of Texas in Austin. (Fig. 9)

The S-parameters of the device were measured and show a possibility for our device to perform data communication at higher frequency with an insertion loss of 0.8 dB at 320 GHz and an isolation of 20 dB at 320 GHz for its ON and OFF state, respectively. (Fig. 10)

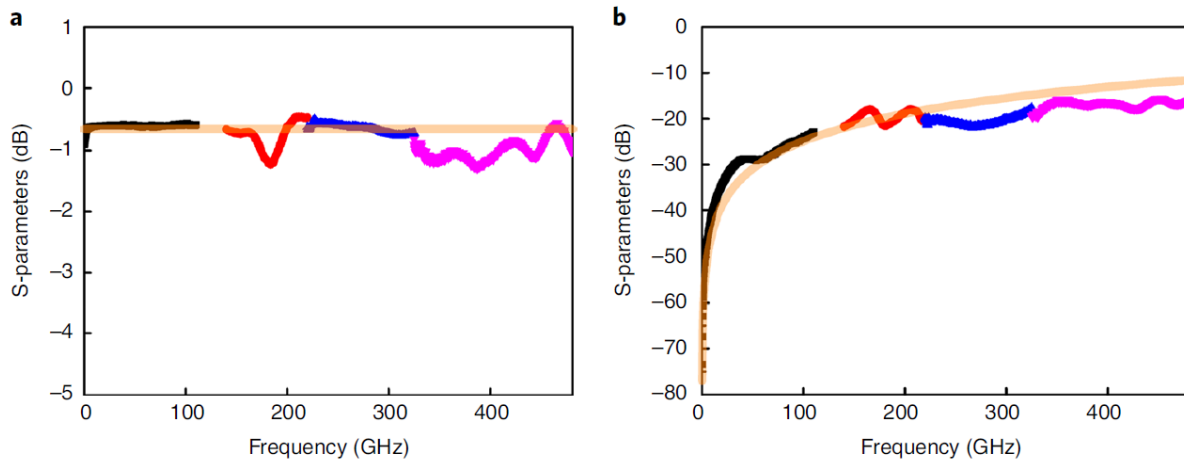


Figure 10 S-parameters of a MoS<sub>2</sub> nonvolatile switch. De-embedded S<sub>21</sub> data in (a) ON state and (b) OFF state. The SET and RESET data are measured on a device with a 0.2x0.2 μm<sup>2</sup> active part area. Black, red, blue and magenta colour lines show S<sub>21</sub> data from the 0.25-110, 140-220-220-325 and 325-480 GHz bands, respectively. The orange lines show the S-parameters of the extracted equivalent lumped element circuit model. The extracted R<sub>ON</sub> and C<sub>OFF</sub> value are 8 Ω and 0.9 fF for a cut off frequency F<sub>CO</sub> = 22 THz from [6]

To evaluate this optimized device response toward IEEE 802.15.3d standard, several vectorial modulations as amplitude-shift keying (ASK) or quadrature phase-shift keying (QPSK) are used. As 6G technology's goal is to be integrated with many applications' scenarios, it needs to be as versatile as possible.

The next part presents the setup used for 100 GHz, the result of this test. Finally, the 320GHz data communication setup and result are presented.

### 3.3. Setup for data communication at 100 GHz

Firstly, a mixed optical signal is created at 100 GHz by photomixing of two optical waves from two lasers at 1550 nm with an wave length difference of 0.8 nm. This signal is then modulated with a Mach-Zehnder modulator and a pseudo random bit sequence creating a modulated optical signal at 100 GHz at the output of the Mach-Zehnder modulator and represented by the pink color in Fig. 11. The modulated optical signal is fed into a photodiode, which generates an electrical signal at the same frequency (100 GHz). The electrical signal (in green on Fig. 11) is then amplified and send to the DUT in our case the fabricated RF switch. The power supplying the switch is precisely controlled by the variable attenuator. At the output of

the DUT, the signal is fed to a Schottky barrier diode, which is used here as an envelope detector for direct detection. The output of the detector (in grey in Fig. 11) is then amplified and send to a buffer amplifier that allows us to use a Bit Error Rate (BER) tester to determine the real timer BER performance.

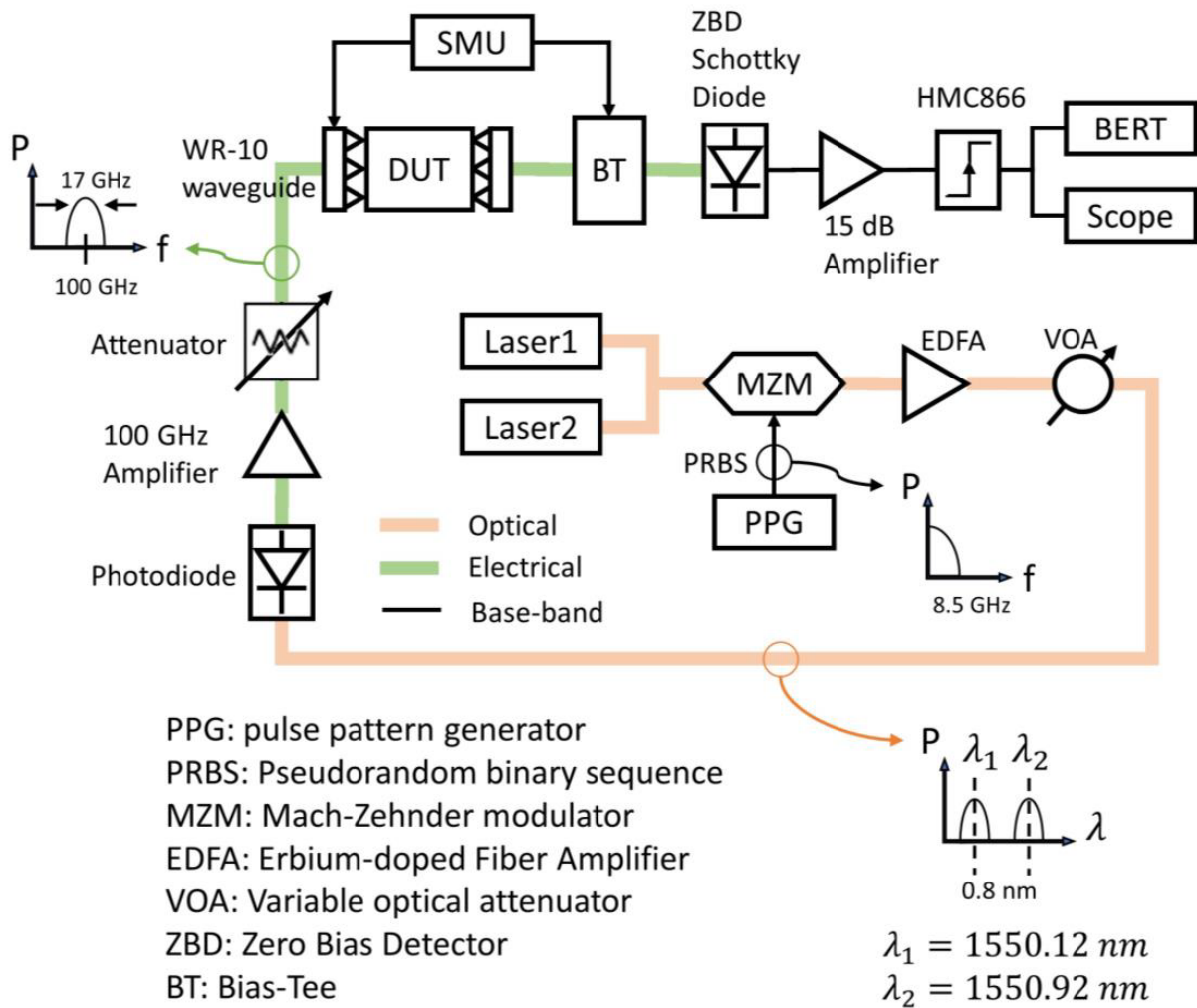


Figure 11 Setup for the 100GHz data communication with OOK modulation

In this experiment, a maximum data rate of  $8.5 \text{ Gbit.s}^{-1}$  is attained because of the limited bandwidth of the setup. (Fig 12)

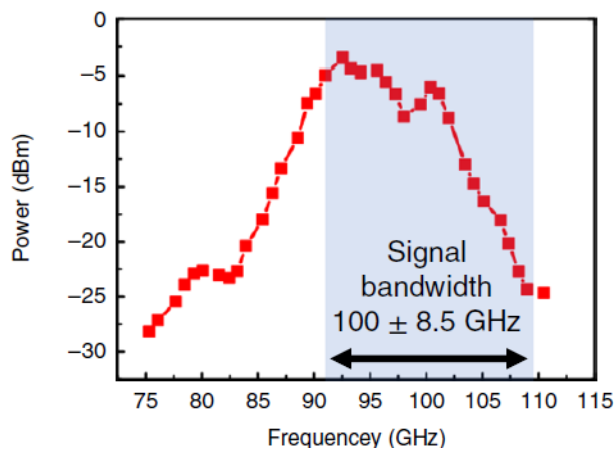


Figure 12 Frequency response of the measurement system from [3]

### 3.4. RF result on data communication at 100 GHz

The demonstration of the switch was done by performing BER measurements on device to determine the quality of a signal flowing through the device, and is recorded in function of the input power. All these measurements were realized at 100GHz carrier frequency and at a data rate of  $8.5\text{Gbit}\cdot\text{s}^{-1}$ . Four BER measurement were realized, the first measurement, used as a reference, is performed by using a direct connection (thru device - SHORT) between the probes that is not a switch but a SHORT structure. Then, three measurements were realized on a working switch, the first one in the ON state (blue curve). The switch is then put in its OFF state and measured again (red curve) and finally put back in its ON state (green curve). The eye pattern associated to each measurement is clearly visible and the evolution of the BER values follow the same course than the thru one.

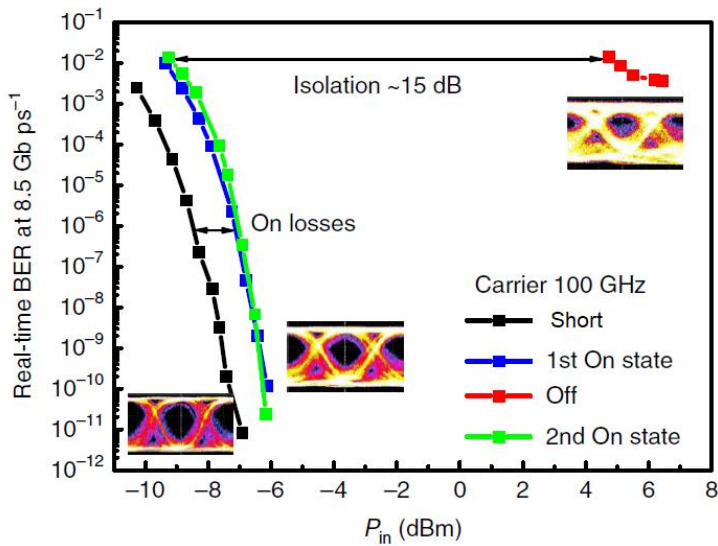


Figure 13 BER measurement with different switch status inset: eye diagram measured at  $f_c = 100$  GHz with a data rate of  $8.5 \text{ Gbit.s}^{-1}$  from [3]

The difference in power between thru and the hBN switch is caused by the insertion loss of the switch over the frequency range of the modulated signal. Due to limitation of the setup, 15 dB was the highest measurable isolation possible to ensure the driving of the BER tester. Higher isolation could not be test because the BER tester could not permit it to be measurable. Other hBN devices exhibit a higher isolation but their BER was not measurable. Furthermore, a data rate of  $2 \text{ Gbit.s}^{-1}$  is tested afterward and show a good eyes diagram and BER value below  $10^{-12}$ . (Fig. 14a and b).

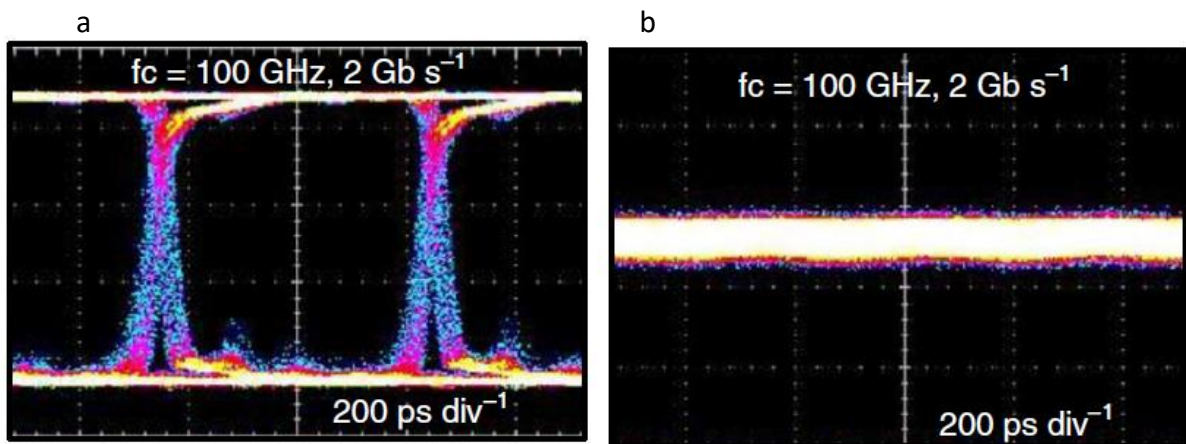


Figure 14 Switches in ON and OFF state showing open (a) and closed (b) eye diagrams at  $f_c = 100$  GHz with a data rate of  $2 \text{ Gbits.s}^{-1}$  from [3]



Finally, a practical test was realized by encoding a high-definition television data stream without compression ( $1.5 \text{ Gbit.s}^{-1}$ ) at 100 GHz and transmitting it through the switch in the ON state. The signal is then decoded and displayed in real time on a television. When the switch is turned off, the television stream stopped as the data transmission was interrupted. A video of this demonstration was realized. [3]

To conclude this data communication at 100 GHz, the maximum data rate achieved with the OOK modulation was  $8.5 \text{ Gbit.s}^{-1}$ . The quality of the signal going through our device was also of good quality with a BER test of  $10^{-12}$  with a power of -6 dBm at a data rate of  $8.5 \text{ Gbit.s}^{-1}$ . A quasi-perfect eye diagram was observed at  $2 \text{ Gbit.s}^{-1}$ . Finally, a real-life scenario proves the worth of the switch with a television data stream transmission.

### 3.5. Data communication at 320 GHz

With the previous result of the data communication, we demonstrated that the device was working across the entire 5G spectrum (100 GHz) with a data rate of  $8.5 \text{ Gbit.s}^{-1}$  with an OOK modulation. However, 6G communication technology based on new standard like the one specified in IEEE 802.15.3d will require higher operating frequencies with carrier frequencies around 300 GHz and the use of advanced modulation like ASK or QPSK for example. [2] Another requirement is also to achieve a high data rate of at least  $100 \text{ Gbit.s}^{-1}$  to support the future application. The device used for this data communication is also a device fabricated in collaboration with university of Texas in Austin and characterized by IEMN. These new devices use one layer of  $\text{MoS}_2$  as a 2D material and are optimized to work at higher than before frequency (around 500 GHz) as show in chapter 2. For that, the structure of the device was modified and match the one presented in chapter 2 with a width of the signal has been reduced to  $20 \mu\text{m}$  and the gap between the source and the ground has been reduced to  $5 \mu\text{m}$ . The substrate used is still diamond. (Fig 13) [6]

The following part focuses on the explanation of the measurement setup follow by discussion on the result and the viability of the devices to match the IEEE 802.15.3d standard. However, because of setup devices availability, the data communication was conducted at 320 GHz carrier rather than the 278.64 GHz that is the standard for IEEE 802.15.3d.



### 3.6. Setup for data communication at 320GHz and advanced vectorial modulation

The 320 GHz setup, which is similar to the one described in the article from S. Nellen *et al* [7], was used to carry out the measurements.

Fig. 15 represents the schematic of the setup. Firstly, two baseband data signals are generated by a Keysight M8195A (allows a generation up to 25 GBaud). These two signals go under an amplitude and phase modulation by means of an Optical I/Q Mach-Zehnder modulator. Two original baseband signals by changing their type determine the final modulation (QAM16, QPSK, OOK) generated at the end of the Mach-Zehnder modulator in the optical domain. This modulated signal at 1549.96 nm and a continuous wave optical laser line at 1552.52 nm are mixed to generate an optical signal at 320 GHz, which is fed to the exact same system that the system described in the previous section for 100 GHz data communication. The photodiode converts the optical signal into an electrical one at 320 GHz and this signal passes through the device. To allow the detection of the advanced modulation, the switch output sends the signal to a GaAs Schottky-barrier sub harmonic mixer at 320 GHz pumped by a local oscillator at 150 GHz. The Intermediate frequency (IF) obtained at the output of the mixer is then amplified by 30 dB by a distributed amplifier (SHF810) and sent to a real-time oscilloscope with 70 GHz bandwidth (Keysight UXR). The processing of these signals allows to obtain the constellation and the performance of the device and particularly the signal to noise ratio (SNR), BER measurement and error vector magnitude (EVM). A signal sent by an ideal transmitter or received by an ideal receiver has all constellation points precisely at the ideal location. However, because of imperfection during the transmission (noise, phase noise, ...) the points of the constellation deviate from their ideal location and EVM is a measure that determines the percentage of error from their ideal position.

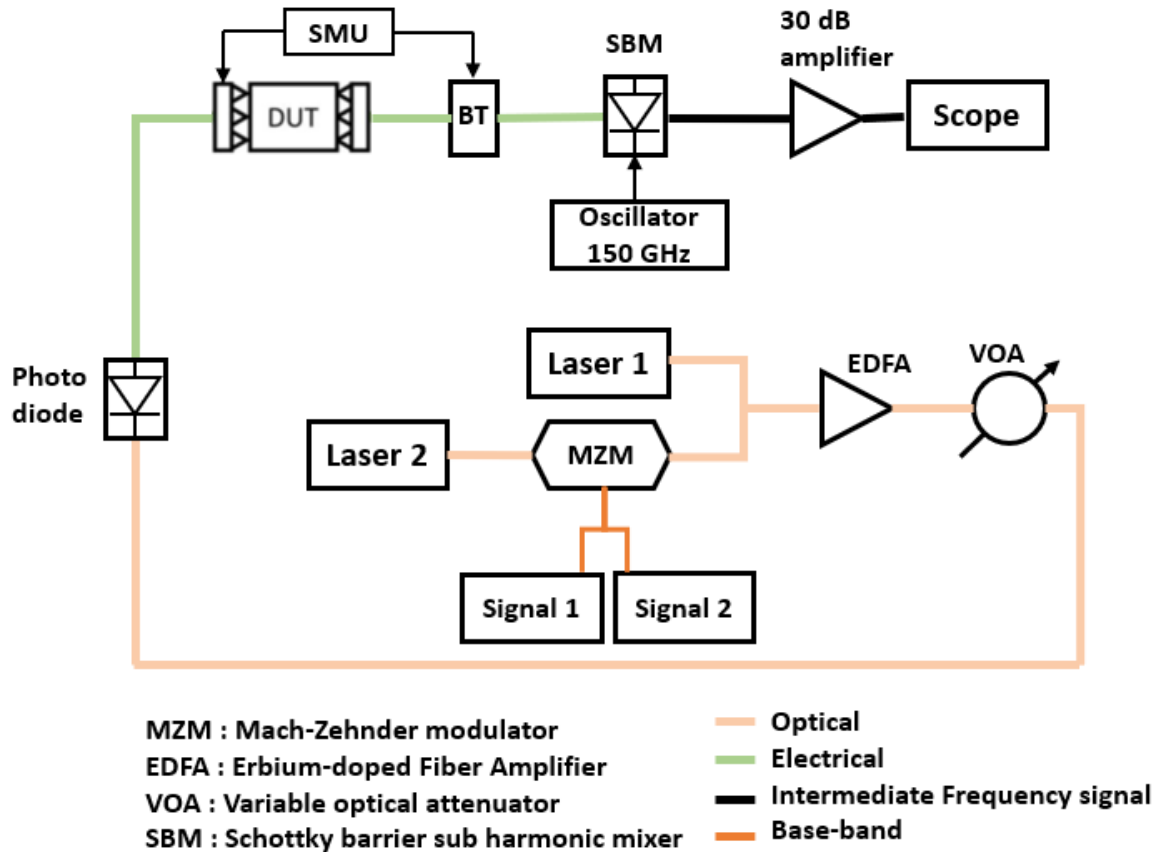


Figure 15 Setup for data communication at 320 GHz with advanced vector modulation

### 3.7. RF result on data communication at 320 GHz

As for the previous data communication test, BER measurement was conducted. It was first realized for different switch states using an amplitude-shift keying (ASK) modulation with a  $10 \text{ Gbits.s}^{-1}$  data rate. As for the 100 GHz BER measurement, first, a through measurement (black line) is realized and serves as the reference using a SHORT device available on-chip and not a switch. Then, a measurement of the RF switch is conducted in its ON state (red line) and its OFF state (blue line). (Fig. 16a) The associated eye diagram is also presented close to the through and ON state curve. The gap between the reference and the ON state originates from the insertion loss of the  $\text{MoS}_2$  switch over the modulated signal. To reach the transmitting and receiving performances wanted in IEEE 802.15.3d, different combination of high baud rate/spectral efficiencies and multilevel modulation are required. Modulation as quadrature phase-shift keying (QPSK) for 10 and 25 GBaud ( $20$  and  $50 \text{ Gbits.s}^{-1}$  respectively), amplitude-phase keying (APSK) with 16 symbol (APSK16) and quadrature amplitude modulation (QAM)

with 16, 32 and 64 symbols (QAM16, QAM32 and QAM64, respectively) were validated with the MoS<sub>2</sub> switch. Fig 16b represent the evolution of the SNR for the previously named modulation methods. It also shows that with a higher data rate, the SNR decrease. This is cause by the limitation of the transmitting and receiving hardware for this experiment.

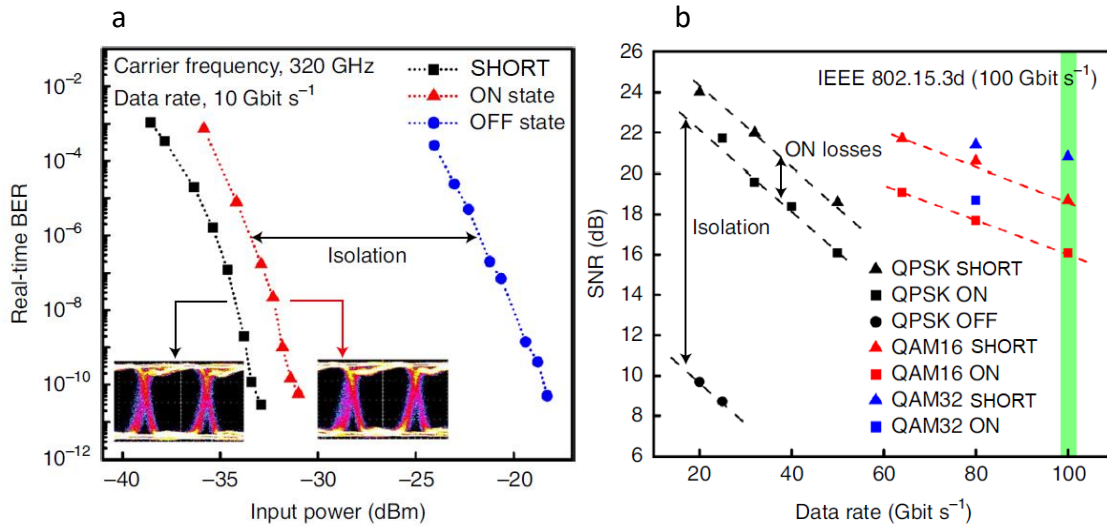


Figure 16 (a) Real-time BER measurement for different states of a switch using ASK modulation. Inset are the respective eye diagram for the SHORT and ON state at 320 GHz carrier frequency and a data rate of 10 Gb.s<sup>-1</sup> from [6] (b) SNR evolution in function of the data rate for different state of the switches and for different modulation from [6]

It also shows that the requirement, of 100 Gbit.s<sup>-1</sup> for 6G network at 300 GHz band, was reached using a QAM16 modulation. Considering the baud rates used of 25 GBaud, the bandwidth is close to 40 GHz, meaning that the RF signal injected into the device cover the 300 to 340 GHz band and the MoS<sub>2</sub> switch could respond successfully to this operation.

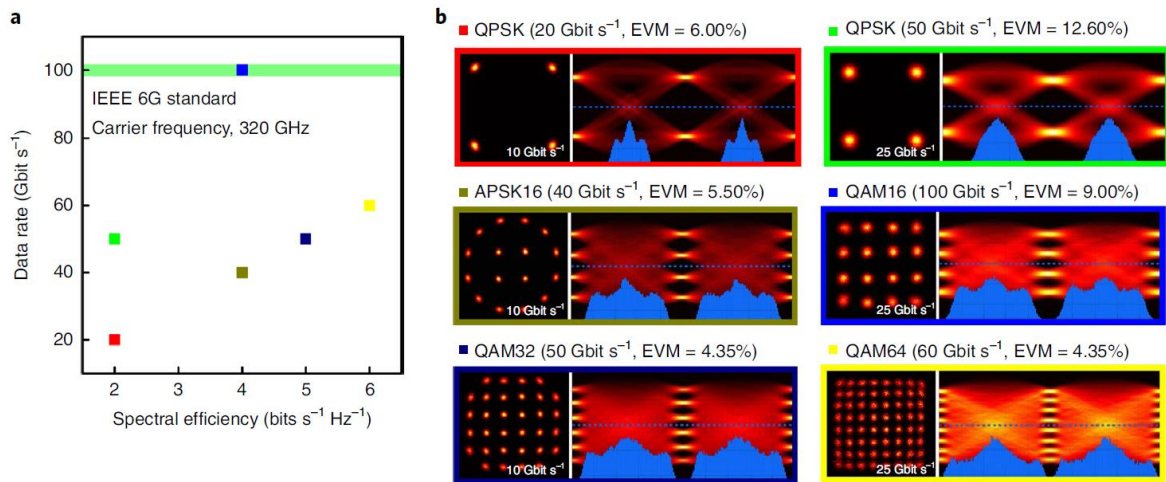


Figure 17 (a) Data communication measurement on MoS<sub>2</sub> switches at different data rates and modulation methods. The green line at 100 Gbits.s<sup>-1</sup> corresponds to IEEE 6G standard for high data rate wireless networks. (b) representative constellation and eye diagram of (a) from [6]

Fig. 17 shows the data communication performance of the MoS<sub>2</sub> device with different data rates and modulation methods. We can observe the eye diagram and constellation diagram for each modulation method. The target data rate of 100 Gbits.s<sup>-1</sup> represented by the green line in Fig. 17a was reached with a 16 QAM modulation. It also indicates the EVM for each modulation order. The blue histograms under the eye diagrams show a signal-crossing probabilities between the eye diagram level. A zero value of this curve at the decision instant means that (normalized time = 1 in the eye patterns) the probability of error is zero. EVM in Fig. 17 is considered as figure-of-merit of the constellation since the BER cannot be measured in real time for I/Q modulation.

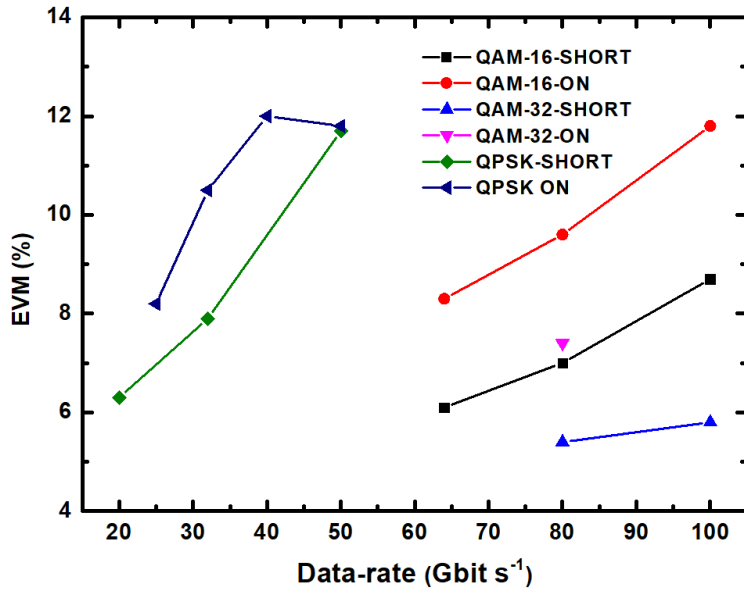


Figure 18 EVM on different modulation methods and data-rates for SHORT structure and ON state

Fig. 18 resume all the EVM measurement obtain for the different modulation techniques tested. We can observe that the higher the data rate, the higher is the EVM. We can also observe that in the ON state, the EVM is around 12% for 100 Gbit.s<sup>-1</sup> data rates that shows that the quality of the signal is high.

After the data rate characterization is conducted, a real-time application was realized. A high-definition data stream was encoded into the 300-GHz band carrier and transmitted through the device. In its ON state, the signal was transmitted decoded and then display on a TV without latency. After electrically switching the device in its OFF state, the data transmission was interrupted and the stream disappear from the TV. This demonstrate that the MoS<sub>2</sub> device can handle real time data streams in the THz band.

## 4. Conclusion

In this chapter, linearity measurements were performed on devices made at IEMN. We demonstrate that these devices possess a good linearity with an IP3 value over 30 dBm and the simulation methods using I-V characteristics was also demonstrated. It shows result close to the measurement with a maximum difference of 3dBm between the measurement and the simulation. We also demonstrate that a better linearity could be reach by switching the device ON with a higher current limitation with a maximum of 30 mA tested. Furthermore, two

interfaces were reported for the linearity measurement with Au/MoS<sub>2</sub>/CrAu and Ni/MoS<sub>2</sub>/Ni interfaces. Both show similar result with a maximum IP<sub>3</sub> of 37 dBm for the Au/MoS<sub>2</sub>/CrAu and 35 dBm for Ni/MoS<sub>2</sub>/Ni for the same dimension.

For the data communication part using devices made in collaboration with the University of Texas and characterized at IEMN, we demonstrate their capability to perform data communication at 100GHz with a simple OOK modulation and 8.5 Gbit.s<sup>-1</sup> data rate for the first batch of device. The first batch of device could exhibit a BER value of 10<sup>-12</sup> at -6 dBm at 100GHz carrier frequency and with a data rate of 8.5 Gbit.s<sup>-1</sup>. This shows the possible uses of our devices for high frequency communication. Furthermore, a real life application scenario realized with this device by encoding and sending through it a data stream of 1.5 Gbit.s<sup>-1</sup> that is then display on television was performed.

Then, the second batch of devices simulated beforehand at IEMN (see chapter 2) demonstrate its capability to match the requirement for 6G IEEE standard. Multiple modulations were tested with different data rates for each (QPSK: 50 Gbit.s<sup>-1</sup>, 16 APSK: 40 Gbit.s<sup>-1</sup>, 32 QAM: 50 Gbit.s<sup>-1</sup>, 64 QAM: 60 Gbit.s<sup>-1</sup> and 16 QAM: 100 Gbit.s<sup>-1</sup>) that is one of the requirements for 6G. The second requirement is a high data rate of 100 Gbits.s<sup>-1</sup> that was reach with a QAM16 modulation. It also demonstrates a good SNR of 16dB for the 16 QAM at 100 Gbit.s<sup>-1</sup> and 16dB for QPSK at 50 Gbit.s<sup>-1</sup>. Finally, a real data stream was encoded at 320 GHz and transmitted through the MoS<sub>2</sub> device and display on TV at 320 GHz carrier frequency. This last demonstration proves the great possibility and the worth of our device as a future 6G device.

## 5. References

- [1] D. M. Pozar, *Microwave Engineering, 4th Edition*. Wiley, 2011.
- [2] V. Petrov, T. Kurner, et I. Hosako, « IEEE 802.15.3d: First Standardization Efforts for Sub-Terahertz Band Communications toward 6G », *IEEE Commun. Mag.*, vol. 58, n° 11, p. 28-33, 2020, doi: 10.1109/MCOM.001.2000273.
- [3] M. Kim *et al.*, « Analogue switches made from boron nitride monolayers for application in 5G and terahertz communication systems », *Nat. Electron.*, vol. 3, n° 8, p. 479-485, aug. 2020, doi: 10.1038/s41928-020-0416-x.

- [4] M. Kim *et al.*, « Non-volatile RF and mm-wave Switches Based on Monolayer hBN », in *2019 IEEE International Electron Devices Meeting (IEDM)*, dec. 2019, p. 9.5.1-9.5.4. doi: 10.1109/IEDM19573.2019.8993470.
- [5] S. M. Hus *et al.*, « Observation of single-defect memristor in an MoS<sub>2</sub> atomic sheet », *Nat. Nanotechnol.*, vol. 16, n° 1, p. 58-62, janv. 2021, doi: 10.1038/s41565-020-00789-w.
- [6] M. Kim *et al.*, « Monolayer molybdenum disulfide switches for 6G communication systems », *Nat. Electron.*, may 2022, doi: 10.1038/s41928-022-00766-2.
- [7] S. Nellen *et al.*, « Coherent Wireless Link at 300 GHz With 160 Gbit/s Enabled by a Photonic Transmitter », *J. Light. Technol.*, vol. 40, n° 13, p. 4178-4185, 2022, doi: 10.1109/JLT.2022.3160096.

# Conclusion and perspectives

In this thesis after briefly presenting commonly used RF switches based on active components (diodes, transistors) and MEMs, emerging devices based on non-volatile memory technologies have been described. Finally, I focused on the presentation of the main topic of this thesis namely RF switches based on 2D materials that have high expectations to operate up to THz frequencies. Their integration and switching are very simple compared to other technologies. In the second chapter, we simulate the coplanar waves guide structure in which our 2D switch is inserted and define its dimension. Two structures were validated, the first one has the objective to be measured up to 67 GHz with a signal's width  $W=40\ \mu\text{m}$  and a gap between ground and signal  $S$  of  $22\ \mu\text{m}$ . The second structure has for objectives to be measured up to 500 GHz with  $W=20\ \mu\text{m}$  and a  $S = 5\ \mu\text{m}$ . The simulation of de-embedding structure gives an idea of the ideal 2D switch OFF and ON state. They reach an isolation of -22 dB and an insertion loss of -0.4 dB at 67 GHz. These values are compatible for future applications. For the second design, the isolation could reach -18 dB at 480 GHz and an insertion loss of -2 dB at 480 GHz. In the third chapter, the fabrication of the 2D RF switch was successful. Three different batches of substrate were fabricated and measured to verify that they are operational. For Au/MoS<sub>2</sub>/CrAu present on SS03 with 6MLs of MoS<sub>2</sub>, the  $0.5\times 0.5\ \mu\text{m}^2$  could reach an insertion loss of -1 dB and an isolation of -16dB at 67GHz and reach a difference of 15 dB for the transmission parameters. For Ni/MoS<sub>2</sub>/Pt interface present on SS04 batch, both  $1\times 1\ \mu\text{m}^2$  and  $0.5\times 0.5\ \mu\text{m}^2$  exhibit a correct behaviour with a  $S_{21}$  parameters difference between the ON and OFF state of 28 dB and 30 dB. Furthermore, the reliability of these devices is correct with 13 out of 19 devices exhibiting multiple switching behaviour. Finally, a last interface identical to the one on SS04 which is Ni/MoS<sub>2</sub>/Pt but with 3 MLs of MoS<sub>2</sub> is studied. It shows RF performance of -1 dB for the insertion loss and -30dB for the isolation at 67 GHz for its ON and OFF state respectively with a  $1\times 1\ \mu\text{m}^2$  device and the value for the  $0.5\times 0.5\ \mu\text{m}^2$  device are close to this one. With the help of de-embedding structure made on chip (OPEN and SHORT structure), we extract the intrinsic parameters  $R_{\text{ON}}$  and  $C_{\text{OFF}}$  of our devices. We obtained for the best device for Ni/MoS<sub>2</sub>/Pt with 6ML of MoS<sub>2</sub> a  $R_{\text{ON}}$  of 11.34  $\Omega$  and a  $C_{\text{OFF}}$  of 0.66 fF for cut



off frequencies of 21.27 THz. These results are good enough to try to work at higher frequency up to 500 GHz.

In the last chapter of this thesis, the analysis of nonlinear parameters shows a good linearity with a minimum value at 26 dBm. We also demonstrate that a better linearity could be reached by switching the device ON with a higher current limitation with a max of 30 mA tested (IP3 of 37 dBm reached). The linearity of the different interfaces tested show that the interface has no impact. Furthermore, the simulation model shows a matching result with the measurement (max 3 dB difference).

For the second part of the last chapter, the data communication shows the capability of hBN RF switch to work at 100 GHz with a data rate of  $8.5 \text{ Gbit.s}^{-1}$ . A BER measurement of  $10^{-12}$  that demonstrate the good quality of the signal. The second data communication realized with a second batch of device made with monolayer of MoS<sub>2</sub>. The monolayer MoS<sub>2</sub> device matches the IEEE 6G requirements by reaching a data rate of  $100 \text{ Gbits.s}^{-1}$  using an QAM 16 modulation with a carrier frequency of 320 GHz. The worth of the devices is proved by sending a data stream into the device successfully at 320 GHz.

To conclude, the table presented in the first chapter is updated with data from the devices made during this thesis.

Table 1 Summary of all technologies from the state of the art with the work of this thesis

Ref	Technology	IL (dB)	IS (dB)	Bandwidth (GHz)	R <sub>ON</sub> (Ω)	C <sub>OFF</sub> (fF)	F <sub>c</sub> (THz)	Control voltage (V)
Y. Kim et al	70nm GaAs m-HEMT SPST	-1.1	-25	59-77	5.4	36	0.81	/
J. Kim et al	65nm CMOS SPST	-4	-40	250-320	/	/	/	/
A. Eltaliawy et al	CMOS SOI SPST	<-3	-50	0-43	/	/	/	< 3
B. Liu et al	MEMS Ohmic contact	-0.2	-22	0-20	/	/	/	50
M. Li et al	MEMS capacitive contact	-0.3	-20.5	0-40	/	/	/	18.3
S. T. Wipf et al	MEMS BiCMOS	-0.44	-24.6	220-325	/	/	/	70
T. Boles et al	SPST PIN diode	-0.3	-50	0-50	/	/	/	/
V. Vassilev et al	SPDT PIN diode	-2.8	-30	55-105	10	23	0.69	1.8
J. Jiang et al	SPST VO <sub>2</sub> switch	-0.4	-28	0-20	/	/	/	15
C. Hilman et al	SPST VO <sub>2</sub> switch	-1	-12	210-290	/	/	/	1
A. Hariri et al	SPST GeTe switch	-2	-15.5	0-20	25	10	0.63	/
T. Singh et al	GeTe switch	-0.6	>20	0-67	/	/	/	/
A. Léon et al	GeTe switch	-0.15	>25	0-40	1.1	6.8	11	7.5
S. López-Soriano et al	CB switch	-1.1	-25	0-3	2	1681	0.04	16
S. Pi et al	CB switch	-0.3	-30	0-40	2.6	1.45	42.2	3
R. Ge et al	MoS <sub>2</sub> Atomristor	-0.25	-29	0-50	11	7.7	1.87	1
This work	hBN monolayer switch	-0.5	-12	0-220	2.8	0.44	129	1.5
This work	MoS <sub>2</sub> monolayer switch	-1	-20	0-480	8	0.9	22	1.5
This work	MoS <sub>2</sub> multilayer switch	-1	-20	0-67	10.9	1.28	11.41	2

## Perspectives:

Based on the result of this work where we show the possibility of the RF switches based on 2D materials. One of the main perspectives will be to continue the measurement of the device made with three and six monolayers of MoS<sub>2</sub> up to 500 GHz frequency. Furthermore, we need to improve our devices by increasing its cyclability. To achieve this goal, one way is to change the way we measure the device by switching the device from a progressive ramp to a pulse measurement to reduce its heating deterioration. We also need to study the possibility to increase the cyclability by reducing the ON state limitation current and then reducing the current needed for resetting the device.

From a fabrication point of view, we can increase the thickness of the metallic electrodes as it seems to be one of the main defaults that cause destruction of the device. We can also try to buried the bottom electrode in SiO<sub>2</sub> to increase the thermal diffusion and reduce the constraints on the 2D and hoping to increase the cyclability of the device.

Furthermore, for the measurement advancement, a new study using similar devices will be realized and we expect to reach the 1 THz working frequency.

Another evolution of this study is to develop memories based on the different resistive state observed on these 2D materials devices. We hope to increase the cycling test by reducing the switching current.

# ANNEX

## Annex of chapter 2

Transformation equation from S-parameter to Z-parameter

$$Z_{11} = \frac{(1 + S_{11})(1 - S_{22}) + S_{12}S_{21}}{\Delta s} Z_0$$

$$Z_{12} = \frac{2S_{12}}{\Delta s} Z_0$$

$$Z_{21} = \frac{2S_{21}}{\Delta s} Z_0$$

$$Z_{22} = \frac{(1 - S_{11})(1 + S_{22}) + S_{12}S_{21}}{\Delta s} Z_0$$

Where  $\Delta s = (1 - S_{11})(1 - S_{22}) - S_{12}S_{21}$  and with  $Z_0$  the characteristic impedance of the network [1].

From the Z parameters, we transform it to its Y parameters with the following equation:

$$Y_{11} = \frac{Z_{22}}{|Z|}$$

$$Y_{12} = \frac{-Z_{12}}{|Z|}$$

$$Y_{21} = \frac{-Z_{21}}{|Z|}$$

$$Y_{22} = \frac{Z_{11}}{|Z|}$$

Where  $|Z| = Z_{11}Z_{22} - Z_{12}Z_{21}$ . [1]

For ON state, we get the following intrinsic parameters after de embedding:

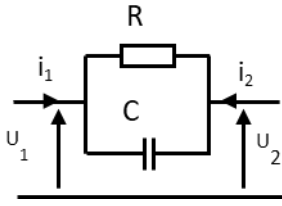


Figure 1 Quadrupole representation of the intrinsic characteristics of the RF switch

From this system we can determine the admittance matrix of this quadrupole:

$$Y_{11} = \frac{1}{R} + jC\omega$$

$$Y_{12} = -\frac{1}{R} - jC\omega$$

$$Y_{21} = -\frac{1}{R} - jC\omega$$

$$Y_{22} = \frac{1}{R} + jC\omega$$

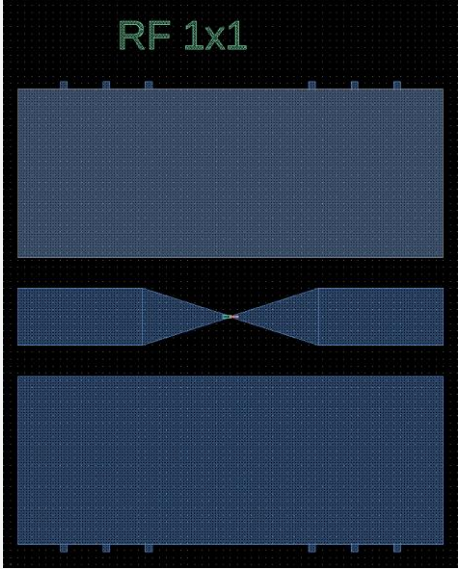
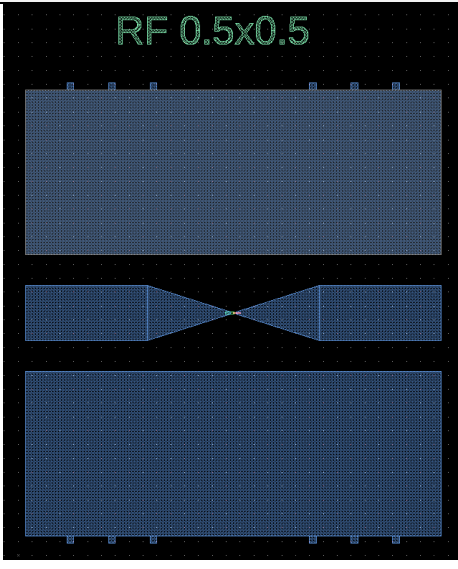
Then from this admittance matrix we can extract the  $R_{ON}$ ,  $C_{ON}$ ,  $R_{OFF}$  or  $C_{OFF}$  by following these equations for the ON state or OFF state respectively:

$$R = \frac{1}{\text{Real}(Y_{11})} = \frac{1}{\text{Real}(-Y_{21})}$$

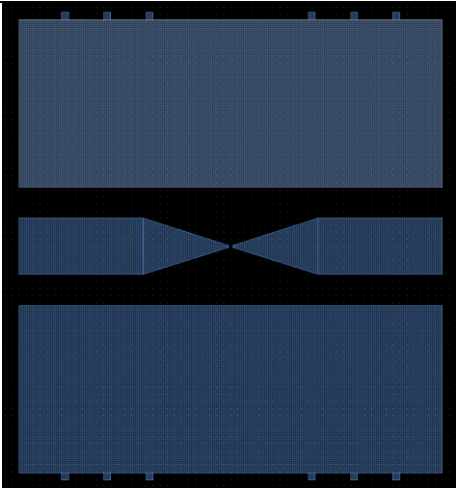
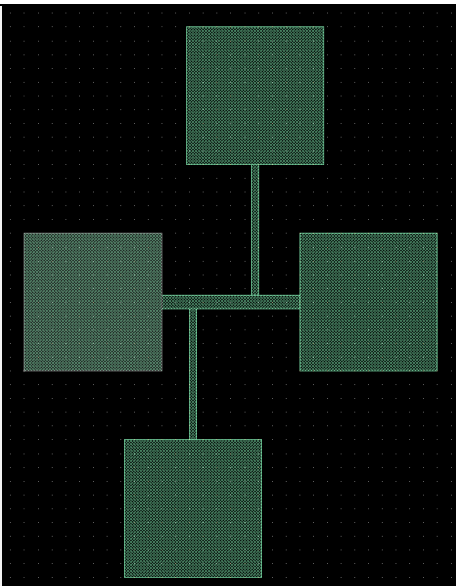
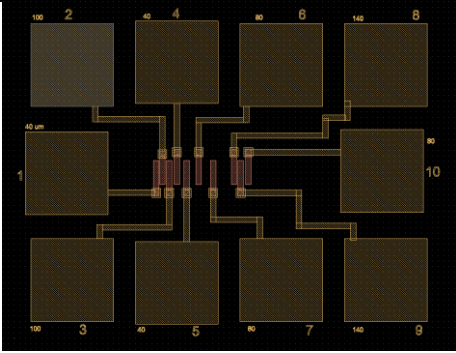
$$C = \frac{\text{Imag}(-Y_{deem}(2,1))}{2 * \pi * \text{Frequency}}$$

## Annex of chapter 3

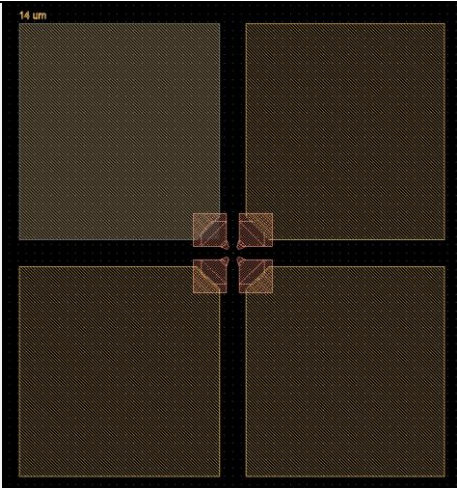
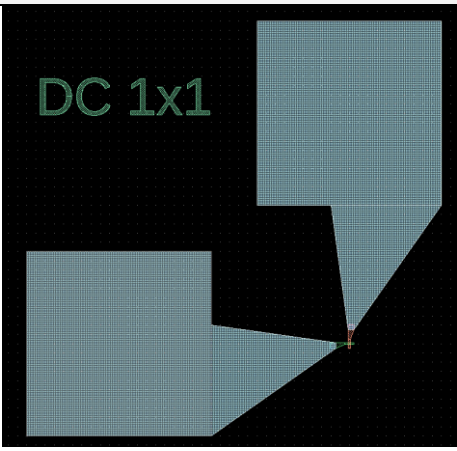
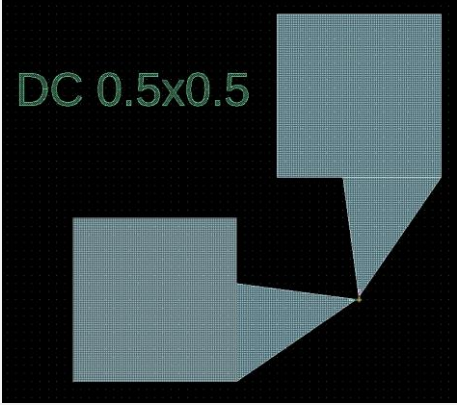
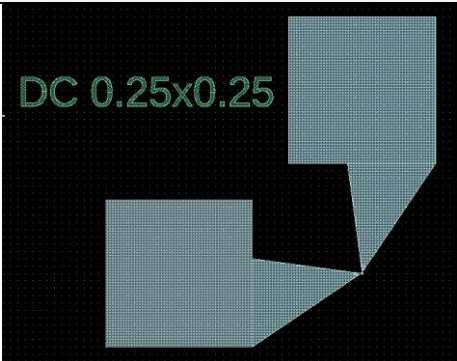
Table 1 Composition of one unit cells with design for each components

Components	Design
20 RF switch $1 \times 1 \mu\text{m}^2$	 <p>The diagram for the RF 1x1 component shows a central blue structure on a black background. At the top, the text "RF 1x1" is written in green. The structure consists of a top horizontal bar with five small rectangular protrusions along its top edge. Below this bar is a central section with a narrow waist, formed by two trapezoidal shapes meeting at a point. At the bottom is another horizontal bar with five small rectangular protrusions along its bottom edge.</p>
20 RF switch $0.5 \times 0.5 \mu\text{m}^2$	 <p>The diagram for the RF 0.5x0.5 component shows a central blue structure on a black background. At the top, the text "RF 0.5x0.5" is written in green. The structure is similar to the 1x1 version but scaled down, with a top horizontal bar and a bottom horizontal bar, each having five small rectangular protrusions. The central section also has a narrow waist formed by two trapezoidal shapes meeting at a point.</p>

<p>20 RF switch <math>0.25 \times 0.25 \mu\text{m}^2</math></p>	 <p>RF 0.25x0.25</p> <p>The micrograph shows a device layout with a central gap. The top and bottom sections are filled with a grid of small squares, representing the 20 RF switches. The central gap contains a structure with a central constriction, likely a quantum dot or a similar device. The text 'RF 0.25x0.25' is overlaid in green at the top of the image.</p>
<p>4 CPW</p>	 <p>The micrograph shows a device layout with four coplanar waveguide (CPW) lines. The lines are arranged in a central gap, with two lines on the top and two lines on the bottom. The lines are connected to the top and bottom sections of the device.</p>
<p>16 SHORT structure</p>	 <p>The micrograph shows a device layout with a central gap. The top and bottom sections are filled with a grid of small squares, representing the 16 SHORT structures. The central gap contains a structure with a central constriction, similar to the one in the first micrograph. The text 'RF 0.25x0.25' is overlaid in green at the top of the image.</p>

<p><b>10 OPEN structure</b></p>	
<p><b>22 Resistivity pattern</b></p>	
<p><b>12 TLM structure</b></p>	



<p><b>4 hall square</b></p>	
<p><b>19 DC switch 1x1μm<sup>2</sup></b></p>	
<p><b>19 DC switch 0.5x0.5μm<sup>2</sup></b></p>	
<p><b>19 DC switch 0.25x0.25μm<sup>2</sup></b></p>	

### **Fabrication process summary:**

*Table 2 Process of alignment mark step by step*

Step 1	Dehydration of substrate at 180°C for 10 min on hot plate
Step 2	Deposition of UV210 41% resist with PC8 spin coater (2500rpm, 1000rpm/s for 15s, lid OPEN) thickness: 2μm
Step 3	Baking 140°C 1min 30 on hot plate
Step 4	Electron beam lithography patterning with EBPG 5000plus with a resolution of 25 nm and 35 μC/cm <sup>2</sup> for the surface density charge current: 25 nA voltage: 100keV
Step 5	Post exposition bake at 140°C for 1min30s and revelation with AZ326MIF for 32s, drying with nitrogen gun
Step 6	Reaction Ion Etching (RIE); SiO <sub>2</sub> etching: CF <sub>4</sub> , 40sccm, 50mTorr, 180W for 15 min material etch 400nm RIE Si etching: SF <sub>6</sub> , 10sccm, 20mTorr 75W for 30s, material etch 400nm Total substrate etched: 800nm
Step 7	Removing polymerized resist: RIE: Oxygen etching: O <sub>2</sub> 20 sccm, 50 mTorr, 50W for 5 min
Step 8	Removing of the remaining resist: SVC 14 at 70°C for 2h Rinsing with acetone for 2 min and IPA for 2 min Drying with nitrogen gun

Table 3 Process of Bottom electrode deposition step by step

Step 1	Dehydration of substrate at 180°C for 10 min on hot plate
Step 2	Deposition of 2 different resist: copolymer EI 6% and PMMA 4% 950K with PC8 spin coater EL 6% (1500 rpm, 1000 rpm/s for 15 s, CLOSE lid / 800 rpm, 1000 rpm/s for 8 s, OPEN lid) thickness: 220 nm Baking for 10min 180°C on hot plate PMMA 4% 950K diluted 5/3 (3500rpm, 1000rpm/s for 30s, OPEN lid) thickness: 80nm Baking for 10min at 180°C on hot plate
Step 3	Patterning with eBeam lithography: surface density charge: 700 $\mu$ C/cm <sup>2</sup> resolution: 10 nm current: 10nA voltage: 100keV
Step 4	Revelation with MIBK/IPA ratio 1/2 for 1min IPA for 30s. Drying with nitrogen gun
Step 5	Metal deposition with plassys MEB 550s Ni/Au: 10/110nm <b>deposition rate:</b> 0.2nm/s and 0.5nm/s or Ni: 120nm <b>deposition rate:</b> 0.2nm/s
Step 6	Lift off: SVC14 at 70°C for 2h Rinsing with acetone for 2min IPA for 2min Drying with nitrogen gun

Table 4 Transfer of MoS<sub>2</sub> step by step (done in CEA-Leti)

Step 1	Cleaning of the target substrate with acetone and IPA in an ultrasonic bath
Step 2	Deposition of PMMA on MoS <sub>2</sub> grown on Si/SiO <sub>2</sub> substrate Baking at 150°C for 3min on hot plate
Step 3	Delamination of PMMA/MoS <sub>2</sub> with Deionized (DI) water for SS03 Delamination of PMMA/MoS <sub>2</sub> with NaOH for SS04 Delamination of PMMA/MoS <sub>2</sub> with NaOH for SS07
Step 4	Fishing up of PMMA/MoS <sub>2</sub> layers with the target substrate (SS03, SS04 and SS07)
Step 5	Slow drying at 80°C on hot plate for 20 min
Step 6	Removal of PMMA layer in acetone for 10 min

Table 5 Patterning step for MoS<sub>2</sub> based switch

Step 1	Baking at 180°C for 10min on hot plate
Step 2	Deposition of PMMA 5% 450K resist with PC8 spin coater (2500rpm, 1000rpm/s for 10s, CLOSE lid / 500rpm, 500 rpm/s for 10s, OPEN lid)
Step 3	Ebeam lithography surface density charge: 700μC/cm <sup>2</sup> resolution: 10nm current: 10nA voltage: 100keV
Step 4	Revelation with MIBK/IPA ratio 1/2 for 1min IPA for 30s and drying with nitrogen gun
Step 5	Etching of the MoS <sub>2</sub> with RIE SF <sub>6</sub> 25sccm, 80mTorr, 50W for 25s
Step 6	Removal of resist: 2h in SVC 14 at 70°C Rinsing with acetone for 2 min IPA for 2min and drying with nitrogen gun

Table 6 Step by step process for TOP electrode for all substrates

Step 1	Dehydration at 180°C for 10min on hot plate
Step 2	Deposition of 2 different resist: copolymer EI 13% and PMMA 4% 950K with PC8 spin coater EL 13% (2000rpm, 1000rpm/s for 15s, CLOSE lid // 800rpm, 1000rpm/s for 8s, OPEN lid) thickness: 700nm Baking for 10min 180°C PMMA 4% 950K (3500rpm, 1000rpm/s for 15s, CLOSE lid //500rpm, 500rpm/s for 8s, OPEN lid) thickness: 150nm Baking for 10min at 180°C on hot plate
Step 3	Ebeam writing of TE surface density charge: 700 $\mu$ C/cm <sup>2</sup> resolution: 10nm current: 10nA voltage: 100keV
Step 4	Revelation with MIBK/IPA ratio 1/2 for 1min IPA 30s Drying with Nitrogen gun
Step 5	Metal deposition SS03 Cr/Au 2/198nm <b>deposition rate:</b> 0.2nm/s and 1nm/s Ni/Au 30/170nm <b>deposition rate:</b> 0.2nm/s and 1nm/s
Step 5	Metal Deposition SS04 Pt/Au 25/175nm <b>deposition rate:</b> 0.2nm/s and 1nm/s
Step 5	Metal Deposition SS07 Pt/Au : 25/275nm
Step 6	Lift off: SVC14 at 70°C for 2h Rinsing with acetone for 2 min IPA for 2min drying with nitrogen gun

Table 7 Step by step process for CPW pads deposition

Step 1	Dehydration at 180°C for 10min on hot plate
Step 2	Deposition of 2 different resist: copolymer EI 13% and PMMA 4% 950K with PC8 spin coater EL 13% (2000 rpm, 1000 rpm/s for 15 s, CLOSE lid // 800 rpm, 1000 rpm/s for 8s, OPEN lid) thickness: 950 nm Baking for 10 min 180°C PMMA 4% 950K diluted 5/3 (3500 rpm, 1000 rpm/s for 30 s, OPEN lid) thickness: 150 nm Baking for 10min at 180°C
Step 3	Ebeam writing of CPW pads density charge: 700 $\mu\text{C}/\text{cm}^2$ resolution: 50 nm current: 25 nA voltage: 100 keV
Step 4	Revelation with MIBK/IPA ratio 1/2 for 1 min IPA 30 s Drying with Nitrogen gun
Step 5	Metal deposition for SS03, SS04 Ni/Au 50/450 nm <b>deposition rate:</b> 0.4 nm/s and 1 nm/s
Step 5	Metal deposition for SS07 Ni/Au 50/450 nm <b>deposition rate:</b> 0.4 nm/s and 1 nm/s
Step 6	Lift off: SVC14 at 70°C for 2h Rinsing with acetone for 2 min IPA for 2min drying with nitrogen gun

**SS04 process change:**

The fabrication change of SS04 is the addition of an adhesion zone close to the 2D. We want to study the precise interface between different metal with the 2D layer with metal like Pt or Au, without adhesion layer that was Cr for SS03 however Pt does not adhere well on Si/SiO<sub>2</sub> substrate, so an additional zone outside of the active part where the 2D has been patterned previously but close to it for the TE to be deposit on top and adhere the substrate is needed and fabricated. The goal of this adhesion zone is to allow the top electrode to adhere the Si/SiO<sub>2</sub> substrate without the metal being present at the interface of the 2D and without being remove during the lift off. This adhesion layer was made at 1  $\mu\text{m}$  outside of the 2D and is a

4\*1 $\mu\text{m}^2$  rectangle made of Ni. The process used for this adhesion zone is a lift off process as the one for the BE. The only difference is the deposition of only 20nm of Ni at a rate of 0.2nm/s. Table 8 resume all the step made for the fabrication of the adhesion zone.

*Table 8 Step by step process for the adhesion zone*

Step 1	Dehydration at 180°C for 10min on hot plate
Step 2	Deposition of 2 different resist: copolymer EI 6% and PMMA 4% 950K with PC8 spin coater EL 6% (3000 rpm, 1000 rpm/s for 15s, CLOSE lid // 800 rpm, 1000 rpm/s for 8 s, OPEN lid) thickness: 130 nm Baking for 10min 180°C on hot plate PMMA 4% 950K diluted 5/3 (3500 rpm, 1000 rpm/s for 30 s, OPEN lid) thickness: 80 nm Baking for 10 min at 180°C on hot plate
Step 3	Ebeam writing of Adhesion zone surface density charge: 600 $\mu\text{C}/\text{cm}^2$ resolution 50 nm current: 25 nA voltage: 100 keV
Step 4	Revelation with MIBK/IPA ratio 1/2 for 1 min IPA 30 s Drying with Nitrogen gun
Step 5	Metal deposition of: Ni 20 nm <b>deposition rate:</b> 0.2 nm/s
Step 6	Lift off: SVC14 at 70°C for 2h Rinsing with acetone for 2 min IPA for 2min drying with nitrogen gun



Table 9 Summary of all interfaces from all samples

Sample	Interfaces present on sample
SS03	Au/MoS <sub>2</sub> (6MLs)/CrAu Ni/MoS <sub>2</sub> (6MLs)/Ni Pt/MoS <sub>2</sub> (6MLs)/Ni
SS04	Au/MoS <sub>2</sub> (6MLs) /Pt Ni/MoS <sub>2</sub> (6MLs) /Pt Pt/MoS <sub>2</sub> (6MLs) /Pt
SS07	Ni/MoS <sub>2</sub> (3MLs) /Pt Pt/MoS <sub>2</sub> (3MLs) /Pt

### I-V characteristics and S-parameters of Ni/MoS<sub>2</sub> (6MLs)/Ni interfaces on SS03

#### Switch structures with an active part of 1x1 μm<sup>2</sup>

The I-V characteristics measurement is realized and only two 1x1μm<sup>2</sup> active part devices could exhibit multiple switching behaviour.

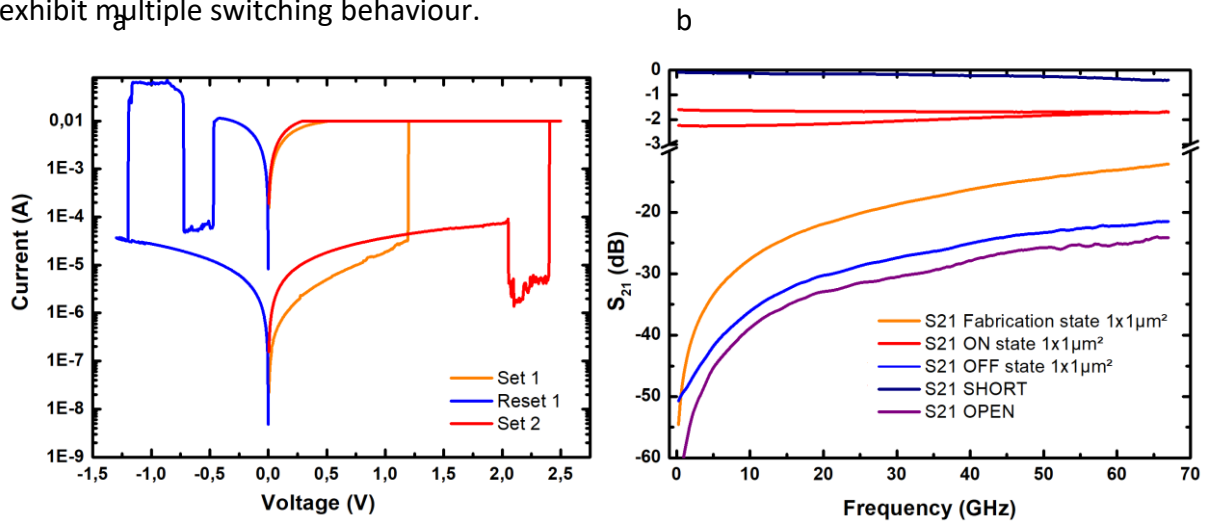


Figure 2 (a) I-V characteristics with multiple cycle on the same 1x1 μm<sup>2</sup> device with the interface Ni/MoS<sub>2</sub>/Ni. (b) S<sub>21</sub> parameter of a 1x1 μm<sup>2</sup> device with multiple switching cycle. The insertion loss is -1.5 dB at 67GHz and an isolation of -20 dB at 67 GHz for the OFF state of the device.

For the dc part show in Fig. 2a, we can see in OFF state a current of 10<sup>-8</sup> A at 0 V and 10<sup>-5</sup> A at 0V in ON state. For the switching voltage, we can observe that it is around 1V for the first set and around 2.5 V for the second set. For the switching with the reset process, it happens around -1.25 V. The device reaches a maximum current value of 70 mA during the reset process. After fabrication, the S-parameters are presented in Fig. 2b, the device reaches an

isolation of -12 dB at 67 GHz for its first state. However, after a cycle, the isolation is improved at -21 dB at 67 GHz. For the ON state, the device possesses an insertion loss of -1.8 dB at 67 GHz. Both the insertion loss and the isolation of the device make a gap of 19 dB for the  $S_{21}$  parameters.

**Switch structures with an active part of  $0,5 \times 0,5 \mu\text{m}^2$**  b

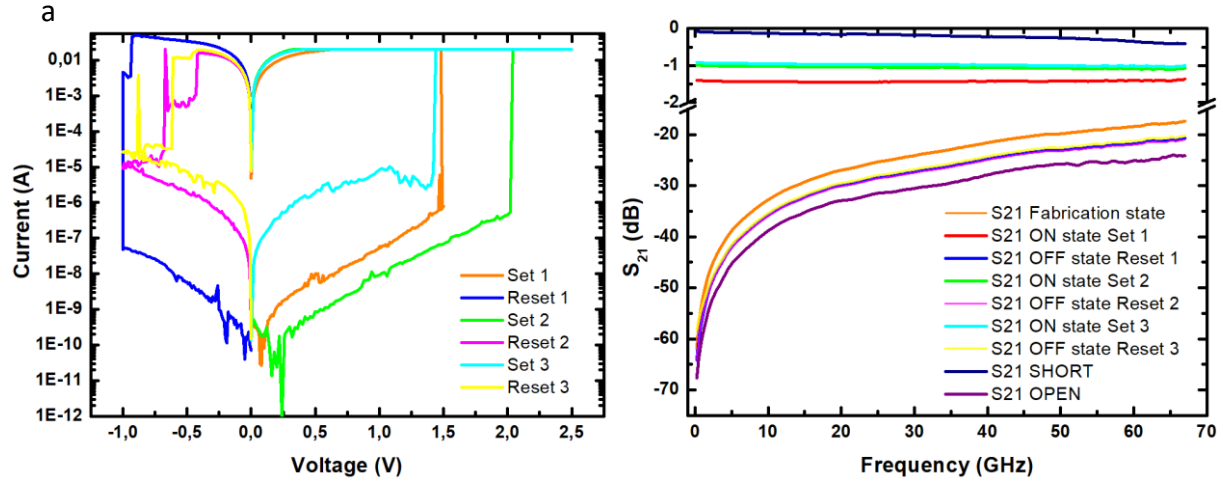


Figure 3 (a) I-V characteristics with multiple cycle on the same  $0.5 \times 0.5 \mu\text{m}^2$  device with the Ni/Mo $\text{S}_2$ /Ni interface. (b)  $S_{21}$  parameters with multiple cycle on the same device. Device size of  $0.5 \times 0.5 \mu\text{m}^2$  active part. The insertion loss is -1 dB at 67 GHz and the isolation is -20 dB at 67GHz for RESET 2.

Fig 3a represents the I-V characteristics of a  $0.5 \times 0.5 \mu\text{m}^2$  device. The current is  $10^{-11}$  A for the OFF state and  $10^{-5}$  A for the ON state at 0V. Device switch from its OFF state to its ON state between 1.5 V and 2 V. the switching voltage for the reset is between -1 V and -0.5 V.

Fig. 31b represents the S-parameters of a  $0.5 \times 0.5 \mu\text{m}^2$  device. We can observe that the isolation after fabrication is around -19dB. The isolation obtained after a RESET process that is around -22 dB. For the ON state part, an insertion loss of -1.5 dB for the first set and improves at a value of -1 dB at 67 GHz for the second set of the device. The gap between isolation and insertion loss is then of 20 dB in  $S_{21}$ .

From the Fig 4, we can observe all the SET/RESET process for one  $1 \times 1 \mu\text{m}^2$  active part device and three  $0.5 \times 0.5 \mu\text{m}^2$  devices. The switching voltage for the set happens between 0.5 V and 2.5 V. For the reset part, all devices reset with a switching voltage between -0.5 V and -0.75 V. The maximum current is 50 mA and happens during a reset.

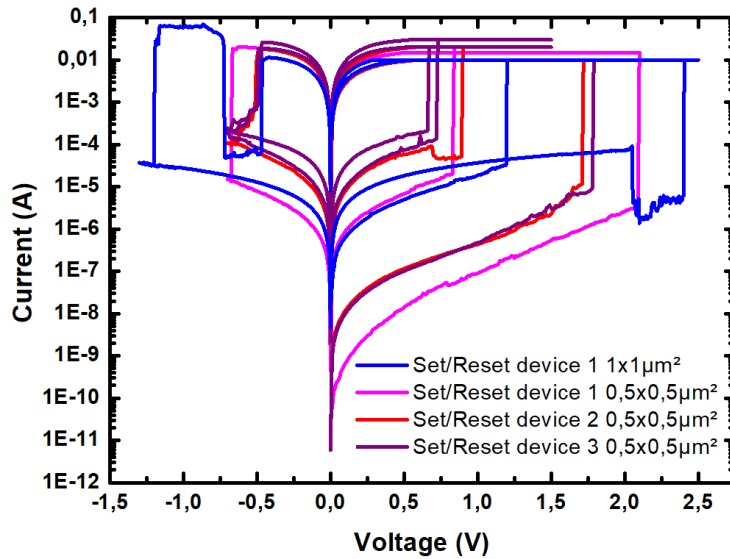


Figure 4 Summary of I-V characteristics for one  $1 \times 1 \mu\text{m}^2$  device and three  $0.5 \times 0.5 \mu\text{m}^2$  device from Ni/MoS<sub>2</sub>/Ni devices. The switching voltage for its state change from its OFF to ON state is between 0.5 V ad 2.5 V. The switching voltage for its state change from its ON to OFF change is between -1.25 V and -0.5 V. The switching value is not impacted by the size of the active part

Table 10 resumes the data for the Ni/MoS<sub>2</sub>/Ni interfaces detailing the number of switches that were tested, the number of working devices and the number of devices with multiple switching behaviour. We observed that the reliability of this process is higher than Au/MoS<sub>2</sub>/CrAu present on the same substrate. All devices work regardless of size, and are consistent in terms of switching.

Table 10 Summary of Ni/MoS<sub>2</sub>/Ni interface device tested

Active part dimension ( $\mu\text{m}^2$ )	# Devices tested	Non-working device	# Switching behaviour observed once	# Multiple switching behaviour
1x1	16	0	16	3
0.5x0.5	16	0	16	10
0.25x0.25	15	3	12	4

## I-V characteristics and S-parameters measurement of Au/MoS<sub>2</sub>/Pt interface

### Switch structures with an active part of 1x1 μm<sup>2</sup>

For the first devices made with Au as BE and Pt for the TE, from the I-V characteristics (Fig. 5a), we obtain the switching voltage from OFF to ON state that is between 0.5 and 1 V and the switching voltage from ON to OFF state that is around -0.5 V. The maximum current reach during the reset process is 35 mA. The current values at 0 V are 10<sup>-5</sup>A in ON state and 10<sup>-8</sup> in OFF state.

Fig. 5b shows S-parameters measured. The device shows isolation around – 8 dB and insertion loss of - 0.8 dB at 67 GHz. The difference between S<sub>21</sub> parameters from its ON and OFF state is of 7dB. The distinction in future application will not be good with a 7 dB gap between both states.

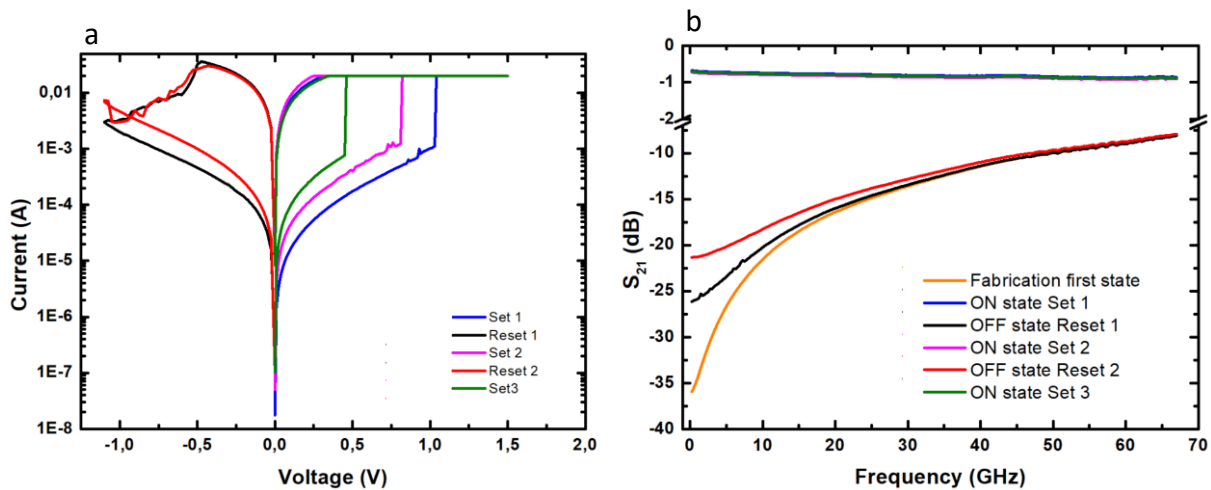


Figure 5 (a) I-V characteristics with multiple cycle on the same 1x1 μm<sup>2</sup> device for the Au/MoS<sub>2</sub>/Pt interface. (b) S<sub>21</sub> parameters of Au/MoS<sub>2</sub>/Pt interfaces with multiple cycle on the same device. Device size of 1x1 μm<sup>2</sup> active part. The insertion loss of this device is -0.9 dB at 67 Ghz and the isolation is -8dB at 67 GHz.

### Switch structures with an active part of 0,5x0,5 μm<sup>2</sup>

For the 0.5x0.5 μm<sup>2</sup> active part area (Fig 6), we can observe that the switching voltage from OFF to ON state between 0.5 and 1 V and a switching voltage from ON to OFF state around - 0.5 V. The maximum value for the current in reset is 45mA. For the current at 0V, its value is 10<sup>-8</sup>A in OFF state and 10<sup>-4</sup> A in ON state. For the S parameters presented in Fig 5b, the isolation value is -15.5 dB at 67 GHz and the device possesses an insertion loss of -1.1 dB at 67 GHz. The

difference between ON and OFF state  $S_{21}$  parameters is 14 dB that is correct but not optimal to distinguish both state in a data communication experiment.

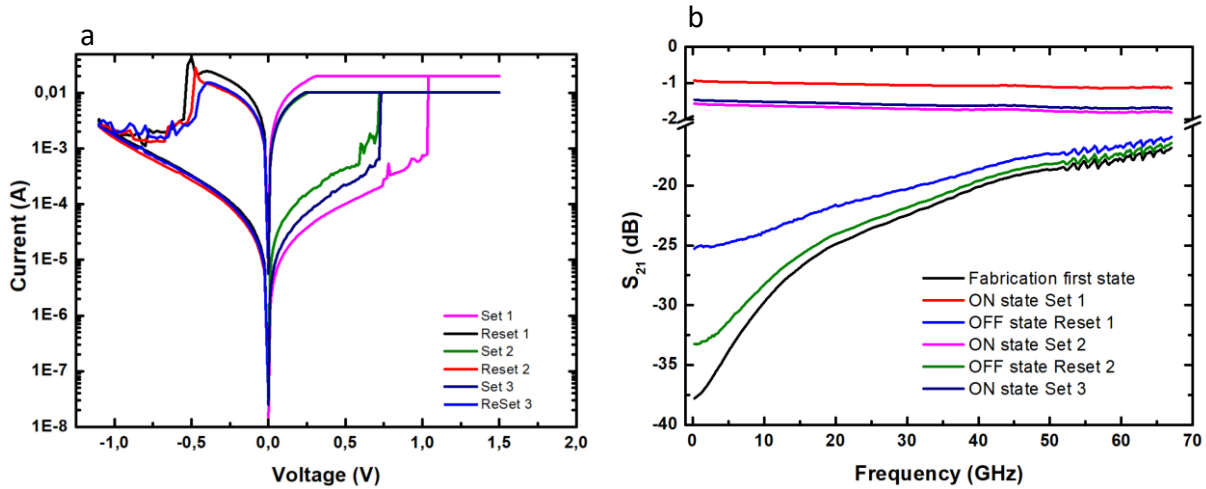


Figure 6 (a) I-V characteristics with multiple cycle on the same  $0.5 \times 0.5 \mu\text{m}^2$  device for the Au/MoS<sub>2</sub>/Pt interface. (b)  $S_{21}$  parameters for one  $0.5 \times 0.5 \mu\text{m}^2$  device with multiple cycle. The insertion loss is -1 dB at 67 GHz and an isolation of -15dB at 67 GHz for RESET 2.

Fig 7 shows all the set and reset process for one  $1 \times 1 \mu\text{m}^2$  device and two  $0.5 \times 0.5 \mu\text{m}^2$  devices. It shows that all set happens between 0.5 V and 1.5 V and all the reset happens between -0.5 V and -1 V and the maximum current reach for all devices reset is 45 mA.

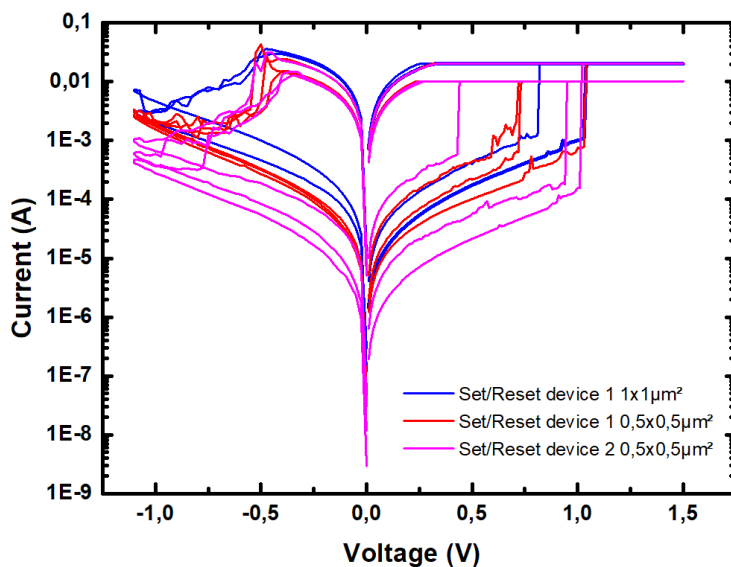


Figure 7 Summary of I-V characteristics of one  $1 \times 1 \mu\text{m}^2$  device and two  $0.5 \times 0.5 \mu\text{m}^2$  devices from Au/MoS<sub>2</sub>/Pt interface. The switching voltage for its state change from OFF to ON state is between 0.5V and 1V. The switching voltage for its state change from its ON to OFF state is between -0.5V and -1V. The size of the device does not impact the switching value.

A summary of the devices tested with their switching behaviour is report in Table 11. It shows that even with a change in the metal for the TE from CrAu to Pt, the ratio of devices that exhibit a multiple switching is around 1/3 for each active part size.

*Table 11 Summary of Au/MoS<sub>2</sub>/Pt interface devices tested*

Active part dimension ( $\mu\text{m}^2$ )	# Devices tested	Non-working device	# Switching behaviour observed once	# Multiple switching behaviour
1x1	7	4	3	2
0.5x0.5	8	4	4	2
0.25x0.25	7	1	6	1

Therefore, considering the structure with a multilayer of MoS<sub>2</sub>, with a gold/platinum interface, the isolation of the switch is not good enough at this frequency range. The main reason is not yet understood. One aspect which was not explored in this work is the detailed analysis of the 2D material.

## Annex of chapter 4

### **Calibration:**

A calibration of the input and output power is needed to accurately characterize the DUT's performances. First, the calibration of the input power is realized with a power meter at the place of the DUT. The difference between the power measured by the power meter and the one from the VNA is then applied to the measurement for each frequency  $F_1$  and  $F_2$ . This part is used to calibrate all the power that enter the device at  $F_1$  and  $F_2$  frequencies, the calibration is represented in red in Fig 8. A high frequency signal generator, previously calibrated, is used to calibrate the measurement at the output of the DUT. It generates signal for each frequency  $F_1$ ,  $F_2$  and  $2F_2 - F_1$  and inject it into the setup at the place of the output of the DUT. Then the difference between the power obtained by the VNA and the power delivered by the generator and measured by the power meter calibrated with the generator, is applied to the measurement for each frequency. This allow to calibrate the output power at all frequency that exist after the device  $F_1$ ,  $F_2$  and  $2F_2 - F_1$ , the calibration of the output is represented in blue in Fig 7. Finally, the loss from the coplanar probes used to connect the DUT to the setup is removed from the measurement. Thus, all the difference from input and output calibration and loss of the probes are removed from the measurement by the software developed to pilot the setup.

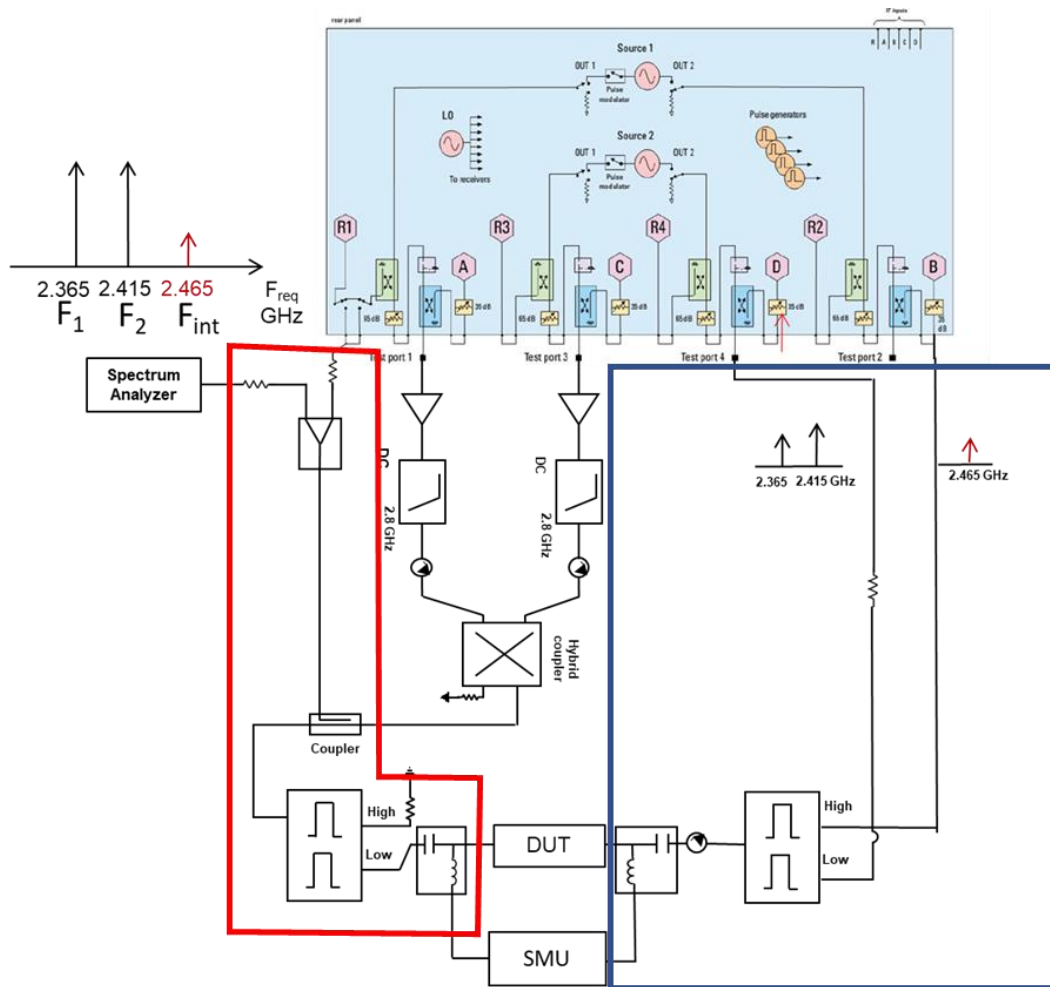


Figure 8 Schematic of the IP3 measurement setup with in red the calibration of the input power and in blue the calibration of the output power

### **SS07 IP3 measurement:**

Device from SS07 were measured for their linearity only on the Ni/MoS<sub>2</sub>/Pt interfaces as only devices from this interface could show multiple switching behaviour during the IP3 measurement.



Table 12 IP3 simulation and measurement for Ni/MoS2/Pt interface on SS07

Device	Active part size ( $\mu\text{m}^2$ )	IP3 measured (dBm)	IP3 simulated (dBm)	Current limitation (mA)
SS07_15	1x1	27	27	30
SS07_17	1x1	29	28	30
SS07_32	0.5x0.5	25	22	20
SS07_33	0.5x0.5	25	25	20
SS07_34	0.5x0.5	37	34	30

# Summary

## **French summary:**

La croissance exceptionnelle du marché des télécommunications due à la révolution digitale en cours et l'importance dans notre vie de tous les jours de l'internet des objets, a entraîné le développement de nombreux systèmes de communications sans fils. De nouveaux systèmes sont envisagés dans des gammes de fréquence peu utilisées jusqu'à présent, telles que les bandes de fréquence au-delà de 100GHz. Ces bandes de fréquence peuvent supporter des débits importants. Pour ces systèmes, il est nécessaire de proposer des commutateurs haute fréquence qui puissent router les signaux de manière efficace à ces fréquences.

Dans cette thèse, nous proposons de développer des commutateurs RF fonctionnant à très haute fréquence (>100GHz) et fabriqués à partir de matériaux qui ont émergés ces dernières années : les matériaux 2D. Ces commutateurs sont constitués d'une à quelques monocouches de matériau 2D, insérées entre deux électrodes métalliques.

Ce travail de thèse a été financé par le projet ANR SWIT n° ANR-19-CE24-0004-01, sous la coordination du Dr. Emiliano PALLECCHI, et en partenariat avec le CEA LETI, IMEP-LaHC. Les composants ont été conçus et fabriqués en utilisant du disulfure de molybdène (MoS<sub>2</sub>) avec 3 et 6 monocouches atomiques dont la croissance est faite au LETI. Compte tenu du mode de fonctionnement de ces composants, la commutation s'effectue en appliquant une rampe en tension positive ou négative pour le faire commuter. Différentes combinaisons de métaux ont été explorées. Ces commutateurs s'insèrent facilement dans les structures de propagation de type coplanaire. La caractérisation de ces composants jusqu'à 67GHz a permis d'obtenir des pertes d'insertion autour de -1dB (dispositif à l'état ON) et une isolation de -25dB (dispositif à l'état OFF) à 67GHz. La caractérisation et l'analyse des propriétés non linéaires de ces commutateurs (IP<sub>3</sub> de l'ordre de 35 dBm) a été effectuée. Ceci nous a permis de développer un modèle de simulation sous ADS<sup>®</sup>, qui s'appuie sur les caractéristiques I-V pour prédire leur comportement non linéaire.

Une collaboration sur cette thématique a été menée avec l'Université du Texas à Austin. Dans ce cadre, des commutateurs avec une monocouche atomique ont été fabriqués (U. Texas-Austin) et caractérisés à l'IEMN.

Dans une première phase, des commutateurs à base d'une monocouche de nitrure de bore (hBN) ont été étudiés. Ces dispositifs ont été caractérisés jusqu'à 220 GHz, et les performances de ce type de commutateur ont été validés en les intégrant avec succès dans un système de transmission à haut débit avec une porteur à 100GHz (modulation tout ou rien – On Off Keying OOK – avec un débit de 8,5 Gbits.s<sup>-1</sup>).

Dans une seconde phase, l'optimisation des structures de propagation, couplée à la fabrication de commutateurs à base d'une monocouche de MoS<sub>2</sub>, nous a permis de valider le comportement des commutateurs pour des signaux jusqu'à 500GHz. Nous avons ainsi pu montrer que ces derniers commutateurs répondaient aux normes du standard IEEE de la future norme 6G pour les télécommunications. En effet, en considérant une porteuse à 320 GHz, différents schémas de modulation ont été testés et nous avons atteint un débit maximal de 100Gbit.s<sup>-1</sup> pour une modulation d'amplitude en quadrature (QAM 16). Un démonstrateur avec un flux vidéo en temps réel intégrant ces commutateurs a été testé et validé avec succès.

**English summary:**

The exceptional growth of the telecommunication market due to the ongoing digital revolution and the importance of the Internet of Things in our daily lives, has led to the development of numerous wireless communication systems. New systems are being considered in frequency ranges that have been little used until now, such as frequency bands above 100GHz. These frequency bands can support high data rates. For these systems, there is a need for high-frequency switches that can route signals efficiently at these frequencies.

In this thesis, we propose to develop RF switches operating at very high frequencies (>100GHz) and made from materials that have emerged in recent years: 2D materials. These switches are made of one to a few monolayers of 2D material, inserted between two metallic electrodes.

This thesis work was funded by the ANR SWIT project n° ANR-19-CE24-0004-01, under the coordination of Dr. Emiliano PALLECCHI, and in partnership with CEA LETI, IMEP-LaHC. The components have been designed and fabricated using molybdenum disulfide (MoS<sub>2</sub>) with 3

and 6 atomic monolayers grown at LETI. Considering the mode of operation of these components, the switching is done by applying a positive or negative voltage ramp to make it switch. Different combinations of metals have been explored. These switches are easily inserted in coplanar propagation structures. The characterization of these components up to 67GHz has resulted in insertion losses around -1dB (device in ON state) and isolation of -25dB (device in OFF state) at 67GHz. The characterization and analysis of the non-linear properties of these switches (IP3 of the order of 35 dBm) has been performed. This allowed us to develop a simulation model under ADS®, which relies on the I-V characteristics to predict their nonlinear behaviour.

A collaboration on this topic was conducted with the University of Texas at Austin. In this context, switches with an atomic monolayer have been fabricated (U. Texas-Austin) and characterized at the IEMN.

In a first phase, switches based on a boron nitride monolayer (hBN) have been studied. These devices have been characterized up to 220 GHz, and the performances of this type of switch have been validated by successfully integrating them in a high-speed transmission system with a carrier at 100GHz (On Off Keying OOK modulation - with a data rate of 8.5 Gbits.s<sup>-1</sup>).

In a second phase, the optimization of propagation structures, coupled with the fabrication of switches based on a MoS<sub>2</sub> monolayer, allowed us to validate the behaviour of the switches for signals up to 500GHz. We were thus able to show that these switches met the IEEE standard for the future 6G telecommunications standard. Indeed, considering a carrier at 320 GHz, different modulation schemes were tested and we reached a maximum data rate of 100Gbit.s<sup>-1</sup> for a quadrature amplitude modulation (QAM 16). A demonstrator with a real time video stream integrating these switches has been tested and validated successfully.

## Publication:

M. Kim, G. Ducournau, S. Skrzypczak, Sung Jin Yang, Pascal Szriftgiser, Nicolas Wainstein, Keren Stern, Henri Happy, Eilam Yalon, Emiliano Pallecchi and Deji Akinwande,  
**« Monolayer molybdenum disulfide switches for 6G communication systems »**, Nat. Electron.

## Conferences:

- Oral at Graphene & 2DM online conference April 2021

S. Skrzypczak, K. Myungsoo, G. Ducournau, D. Vignaud, R. Gassilloud, A. Cresti, J. David-Viffantzeff, Y. Deblock, V. Avramovic, H. Happy, D. Akinwande, and E. Pallecchi,  
**“Switch RF based on 2D material”**

- Oral at Graphene conference in Grenoble on October 2021

S. Skrzypczak, K. Myungsoo, G. Ducournau, D. Vignaud, R. Gassilloud, A. Cresti, J. David-Viffantzeff, Y. Deblock, J. Hadid, V. Avramovic, H. Happy, D. Akinwande, and E. Pallecchi  
**“Non linearity of RF switch based on 2D materials”**

- Oral at HOWDI GDR in Dourdan on May 2022

S. Skrzypczak, M. Kim, G. Ducournau, D. Vignaud, R. Gassilloud, A. Cresti, J. David-Viffantzeff, Y. Deblock, J. Hadid, V. Avramovic, H. Happy, D. Akinwande, and E. Pallecchi  
**“2D switches for RF application”**

- Oral at JNM (National Microwaves Day) in Limoges on June 2022

S. Skrzypczak, M. Kim, G. Ducournau, D. Vignaud, R. Gassilloud, A. Cresti, J. David-Viffantzeff, Y. Deblock, J. Hadid, V. Avramovic, H. Happy, D. Akinwande, and E. Pallecchi  
**« Commutateur RF fabriqué à parti de matériau 2D »**

- Oral at Graphene week in Berlin on September 2022

S. Skrzypczak, M. Kim, G. Ducournau, D. Vignaud, R. Gassilloud, A. Cresti, J. David-Viffantzeff, Y. Deblock, J. Hadid, V. Avramovic, H. Happy, D. Akinwande, and E. Pallecchi

***“RF switches with 2D material”***

- Oral at workshop for GRAPHENE flagship in Lucca on October 2022

S. Skrzypczak, M. Kim, G. Ducournau, D. Vignaud, R. Gassilloud, A. Cresti, J. David-Viffantzeff, Y. Deblock, J. Hadid, V. Avramovic, H. Happy, D. Akinwande, and E. Pallecchi

***“RF Switch based on 2D material”***